

**THERMAL CHARACTERIZATION OF SEMICONDUCTING  
POLYMER BULK HETEROJUNCTIONS**

by

Roddel A. Remy

A dissertation submitted to the Faculty of the University of Delaware in partial fulfillment of the requirements for the degree of Doctor of Philosophy in Materials Science and Engineering

Fall 2016

© 2016 Roddel A. Remy  
All Rights Reserved

ProQuest Number:10246342

All rights reserved

INFORMATION TO ALL USERS

The quality of this reproduction is dependent upon the quality of the copy submitted.

In the unlikely event that the author did not send a complete manuscript and there are missing pages, these will be noted. Also, if material had to be removed, a note will indicate the deletion.



ProQuest 10246342

Published by ProQuest LLC (2017). Copyright of the Dissertation is held by the Author.

All rights reserved.

This work is protected against unauthorized copying under Title 17, United States Code  
Microform Edition © ProQuest LLC.

ProQuest LLC.  
789 East Eisenhower Parkway  
P.O. Box 1346  
Ann Arbor, MI 48106 – 1346

**THERMAL CHARACTERIZATION OF SEMICONDUCTING  
POLYMER BULK HETEROJUNCTIONS**

by

Roddel A. Remy

Approved: \_\_\_\_\_

Darrin J. Pochan, Ph.D.

Chair of the Department of Materials Science and Engineering

Approved: \_\_\_\_\_

Babatunde A. Ogunnaike, Ph.D.

Dean of the College of Engineering

Approved: \_\_\_\_\_

Ann L. Ardis, Ph.D.

Senior Vice Provost for Graduate and Professional Education

I certify that I have read this dissertation and that in my opinion it meets the academic and professional standard required by the University as a dissertation for the degree of Doctor of Philosophy.

Signed: \_\_\_\_\_

Michael E. Mackay, Ph.D.  
Professor in charge of dissertation

I certify that I have read this dissertation and that in my opinion it meets the academic and professional standard required by the University as a dissertation for the degree of Doctor of Philosophy.

Signed: \_\_\_\_\_

Steven R. Aubuchon, Ph.D.  
Member of dissertation committee

I certify that I have read this dissertation and that in my opinion it meets the academic and professional standard required by the University as a dissertation for the degree of Doctor of Philosophy.

Signed: \_\_\_\_\_

William N. Shafarman, Ph.D.  
Member of dissertation committee

I certify that I have read this dissertation and that in my opinion it meets the academic and professional standard required by the University as a dissertation for the degree of Doctor of Philosophy.

Signed: \_\_\_\_\_

Eric M. Furst, Ph.D.  
Member of dissertation committee

I certify that I have read this dissertation and that in my opinion it meets the academic and professional standard required by the University as a dissertation for the degree of Doctor of Philosophy.

Signed: \_\_\_\_\_

Darrin J. Pochan, Ph.D.

Member of dissertation committee

## ACKNOWLEDGEMENTS

I would be remiss if I began my acknowledgements without first thanking Dr. Derrick Swinton who, in my junior year of college at Lincoln University, convinced me to attend a seminar at the University of Delaware. It was lunchtime on a Friday and I had no idea what the topic of the seminar was until I arrived and found out that it was about solar energy. There I met Dr. Michael Mackay and then group members Dr. Jonathan Kiel and Dr. Jonathan Seppala. Six years later I am writing a thesis about polymer solar cells under the advisement of Dr. Mackay. If it wasn't for Dr. Swinton's influence, the past six years would have been completely different.

I would like to thank Dr. Michael Mackay, my advisor, for sticking it out with me. The ideas and hypotheses in this thesis were unclear in the beginning, but your encouragement and thoughtfulness brought them to light. Dr. Steven Aubuchon was also instrumental in teaching me everything I know about the practical elements of thermal analysis. Your expertise and keen eye for experimental accuracy kept me on my toes. The rest of my thesis committee: Dr. Darrin Pochan, Dr. William Shafarman and Dr. Eric Furst, has always been there supporting me, offering advice and checking in whenever I come across them.

Dr. Jonathan Kiel and Dr. Jonathan Seppala were the first two members of the Mackay research group that I met. Their candid responses to my questions about graduate school and the research life was greatly appreciated at a time when I had to make those decisions that would lead me along such a path. Dr. Brett Guralnick basically took me under his wing when I entered the Mackay group as a graduate student. He taught me how to manage and explore ideas in the lab. He, along with Dr. Hao Shen, Dr. Jeong Jae Wie and Dr. Wenluan Zhang were all amazing sounding boards and teachers as the senior laboratory members. Dr. Ngoc Nguyen and I entered

the University and the Mackay group together. We leaned on each other during tough classes and homeworks, teaching assistantships, research, conferences and presentations to survive this journey. Our friendship means a lot to me.

Collaborations were a large part of my Ph.D. experience. I was fortunate to perform research and be funded by the NIST Center for Neutron Research. Dr. Brian Kirby was extremely helpful and always entertained my random questions about neutrons and experimental ideas involving them. Thanks to my collaborators at Carnegie Mellon, Dr. Tomasz Kowalewski and Dr. Emily Daniels Weiss for generously sharing your P3HT samples and data. Also, thanks to Dr. Luis Campos and Dr. Sujun Wei for taking the time to synthesize regiorandom P3HT for my investigations. At the University of Delaware, I had the pleasure of collaborating with the research group of Dr. Thomas Epps, Dr. Xinqiao Jia and her post doctoral student Dr. Shuang Liu. All of the cooperative work that was done during this experience produced publications and forged professional relationships that I treasure.

Finally, my family and friends have been my rocks from the very beginning. They have stood by me, supported me and helped calm me down when things got rough. They never stopped having faith in me even when my faith in myself was low. The Department of Materials Science and Engineering, the Black Graduate Student Association and the Graduate Student Government were all sources of social and professional development. I can only hope those relationships get stronger with time. Being the only one in my immediate family to achieve this academic level made it extremely difficult to describe what was going on, not to mention being thousands of miles apart. Despite this, the love and understanding that my family expressed has kept me grounded and driven to complete my studies and continue on a path of success.

## TABLE OF CONTENTS

<b>LIST OF TABLES</b> . . . . .	<b>x</b>
<b>LIST OF FIGURES</b> . . . . .	<b>xi</b>
<b>ABSTRACT</b> . . . . .	<b>xvi</b>
 <b>Chapter</b>	
<b>1 INTRODUCTION</b> . . . . .	<b>1</b>
1.1 Energy Outlook . . . . .	1
1.2 Solar Cells . . . . .	3
1.3 Organic/Polymer based Solar Cells . . . . .	4
1.3.1 Device Architecture and Morphology . . . . .	5
1.4 Thesis Outline . . . . .	8
<b>BIBLIOGRAPHY</b> . . . . .	<b>10</b>
<b>2 A FACILE CALCULATION OF THE ENTHALPY OF FUSION OF POLY(3-HEXYLTHIOPHENE)</b> . . . . .	<b>16</b>
2.1 Introduction . . . . .	16
2.2 Experimental . . . . .	18
2.3 Results and Discussion . . . . .	21
2.3.1 DSC Analysis . . . . .	21
2.3.2 Onset of Chain Folding . . . . .	24
2.3.3 $\Delta H_m^\infty$ Modification . . . . .	26
2.4 Secondary Confirmation of Crystallinity . . . . .	29
2.5 Equilibrium Melting and Entropy . . . . .	31
2.6 Conclusion . . . . .	33

<b>BIBLIOGRAPHY</b> . . . . .	<b>34</b>
<b>3 QUANTIFYING THE RIGID AMORPHOUS FRACTION IN POLY(3-HEXYLTHIOPHENE)</b> . . . . .	<b>42</b>
3.1 Introduction . . . . .	42
3.2 Experimental . . . . .	44
3.3 Results and Discussion . . . . .	45
3.3.1 MDSC Technique and Parameter Optimization . . . . .	45
3.3.2 RAF Calculation for Bulk rrP3HT . . . . .	48
3.3.3 RAF Calculation for Thin Film ranP3HT . . . . .	52
3.3.4 RAF Calculation for Thin Film rrP3HT . . . . .	55
3.4 Conclusion . . . . .	57
<b>BIBLIOGRAPHY</b> . . . . .	<b>59</b>
<b>4 REFINING THE DESCRIPTION OF THE POLYMER:FULLERENE BULK HETEROJUNCTION</b> . . . . .	<b>67</b>
4.1 Introduction . . . . .	67
4.2 Experimental . . . . .	68
4.3 Results and Discussion . . . . .	69
4.3.1 Chemical Reaction at the PEDOT:PSS Interface . . . . .	69
4.3.2 TMDSC and Crystallinity Analysis . . . . .	72
4.3.3 $T_g$ and the Amorphous Fraction . . . . .	77
4.3.4 Combination of SANS and MDSC for RAF Calculation . . . . .	81
4.4 Conclusion . . . . .	84
<b>BIBLIOGRAPHY</b> . . . . .	<b>85</b>
<b>5 INVESTIGATION OF INTERFACIAL PCBM DIFFUSION BY NEUTRON REFLECTIVITY</b> . . . . .	<b>90</b>
5.1 Introduction . . . . .	90

5.2	Experimental . . . . .	91
5.3	Results and Discussion . . . . .	92
5.3.1	PEDOT:PSS Layer Modeling . . . . .	92
5.3.2	P3HT/PEDOT:PSS bilayer . . . . .	93
5.3.3	PCBM/PEDOT:PSS bilayer . . . . .	95
5.3.4	Analysis of Diffusion into PEDOT:PSS . . . . .	98
5.4	Conclusion . . . . .	100
<b>BIBLIOGRAPHY . . . . .</b>		<b>102</b>
<b>6 THESIS CONCLUSION AND FUTURE WORK . . . . .</b>		<b>107</b>
6.1	Conclusion of Thesis . . . . .	107
6.2	Future Work . . . . .	109
6.2.1	A New P3HT:PCBM Phase Diagram . . . . .	109
6.2.2	Replacing PEDOT:PSS . . . . .	109
6.2.3	PCBM Thermal Properties . . . . .	111
6.2.4	High Performance Donor Polymers . . . . .	112
<b>BIBLIOGRAPHY . . . . .</b>		<b>114</b>
<b>Appendix</b>		
A	TMDSC OF PCBM . . . . .	119
B	REPRINT PERMISSIONS . . . . .	121

## LIST OF TABLES

2.1	Characteristics of P3HT used in this paper. . . . .	19
2.2	Comparison of measured c-axes of each sample to theoretical values. . . . .	26
2.3	Results of the X-ray reflectivity fitting procedure. . . . .	28
3.1	Measurements from TMDSC of rrP3HT . . . . .	52
3.2	Calculated percentages of the three phases in rrP3HT thin films. . . . .	56
4.1	Measurements taken from the TMDSC experiments shown in Figure 4.3. . . . .	74
4.2	Measured and calculated BHJ phases from TMDSC and SANS . . . . .	83
5.1	Table of initial $\rho$ for each examined component. . . . .	92
5.2	Calculated $\phi_{PCBM}$ contained in PEDOT:PSS layer. . . . .	97

## LIST OF FIGURES

1.1	The top graph show the world's energy consumption in quadrillion Btu ( $\sim 3 \times 10^{11}$ kilowatthours) by energy source. The bottom graph shows the world's electricity generation in trillion ( $10^{12}$ ) kilowatthours. Both graphs contain past data as well as projections through 2040.[1] . . . . .	2
1.2	U.S. plans for installing/retiring generation capacity (in gigawatts) based on the short, mid and long term application of the EPA's Clean Power Plan.[3] . . . . .	3
1.3	Graph showing best laboratory scale solar device efficiencies over time, by material class. This plot is courtesy of the National Renewable Energy Laboratory, Golden, CO. . . . .	4
1.4	Illustrations of different polymer solar cell morphologies. A single conjugated polymer sandwiched between two electrodes (a). A layered structure of polymer donor and electron acceptor (b). A bulk heterojunction structure (c). An optimized heterojunction structure (d). Reprinted from Ref. [21] with permission from the American Chemical Society. . . . .	6
1.5	A diagram of the conventional P3HT:PCBM bulk heterojunction solar cell. . . . .	7
2.1	$H^1$ NMR of regiorandom P3HT illustrating the process of calculating regioregularity in the P3HT samples employed in this work. . . . .	20
2.2	(a) DSC thermograms of the different P3HT samples used in this work. Dashed lines are tangents drawn to illustrate the integrated area for each sample. Graphs shifted vertically for clarity. GIWAXS data and their associated in (red) and out (blue) of plane line profiles of (b) DP31 and (c) DP66 samples. . . . .	22

2.3	Graph of melting enthalpy vs. $1/M$ for P3HT. Straight line drawn using <i>Low M region</i> and extrapolated to give the y-intercept ( $\Delta H_m^\infty$ ). The diamonds are from Ref. [23] and is included with the data gathered here. . . . .	23
2.4	Shown are TEM micrographs of DP31 (a), DP47 (b), DP62 (c), DP66 (d) and CS (e) nanofibrils. Also shown is a schematic of the typical <i>edge-on</i> P3HT crystal orientation (f). . . . .	25
2.5	Plot of crystalline P3HT volume fraction ( $\Phi_{crystal}$ ) vs. degree of polymerization (DP) derived from the Porod analysis of GISAXS data (not shown). Linear region up to DP62 can be used as correction factor for the DSC melting enthalpy of the respective samples. . . .	27
2.6	X-ray reflectivity of regiorandom P3HT on a Si substrate with a natural oxide layer showing the fit to the experimental data. . . . .	28
2.7	Graph of <i>Low M region</i> showing original and corrected values for the melting enthalpies and their corresponding linear fits. . . . .	29
2.8	Graph of P3HT density vs. crystalline fraction. Orange circles and line depict the linear relationship between the fully amorphous ( $\rho_a$ ) and fully crystalline ( $\rho_c$ ) P3HT. Blue square shows that the crystalline fraction in CS from density measurements follows this relationship while the DSC analysis gives a slightly lower result. . .	30
2.9	Graph of $T_m^\infty$ and $\Delta S_m^\infty$ versus inverse molecular weight of the <i>Low M region</i> . Dashed lines are linear fits to each dataset. Points shown correspond to the average value $\pm$ one standard deviation. . . . .	32
3.1	Deconvoluted data from two TMDSC experiments on rrP3HT. Total heat flow thermograms are shown in (a) and (c) with their experimental parameters. An overlay of their respective heat flow signals from a typical DSC experiment (red dashed lines) is also shown to illustrate the similarity in the resultant data of both methods. Black dot-dashed line in (c) defines the area used to calculate sample crystallinity. Reversing and non-reversing heat flow thermograms for (a) and (c) are displayed in (b) and (d), respectively.	46

3.2	Raw TMDSC data from both experimental parameters. (a) Parameters taken from Ref. [24] and (b) parameters used in this study. (c) shows a magnified view of the melting transition in (b). It can be observed that the parameters used here more than double the oscillations across the melting transition resulting in more accurate deconvolution. . . . .	47
3.3	TMDSC thermograms showing $c_p^{rev}$ of ranP3HT (a) and rrP3HT (b), along with their respective derivatives, $dc_p^{rev}/dT$ , in (c) and (d). The red dashed lines in (b) and (d) identify the local minima in $dc_p^{rev}/dT$ for rrP3HT used to assign regions I, II and III. . . . .	49
3.4	Illustration defining the proposed "mobile beads" that comprise a P3HT monomer unit. Blue represents the large bead that provides twice the energy as the small beads (red). . . . .	50
3.5	A closer view of $c_p^{rev}$ of rrP3HT showing how $\Delta C_{p,sam}$ was split into $\Delta C_{p,1}$ and $\Delta C_{p,2}$ for the calculation of MAF and RAF respectively. . . . .	51
3.6	Graphs showing $c_p^{rev}$ in the $T_g$ region of a ranP3HT thin film (a) and its derivative (b). Both first heat and second heat data are shown to illustrate the difference in $\Delta C_p$ due to thin film effects. Graphs in (a) are vertically offset for clarity. . . . .	53
3.7	Graphs showing $c_p^{rev}$ in the $T_g$ region of a rrP3HT thin film (a) and its derivative (b) as well as a magnification of the melting region (c). Red dashed lines in (a) and (b) indicate side chain, MAF and RAF regions respectively. Black dot-dashed line in (c) illustrates the baseline from which crystallinity was measured. Graphs are vertically offset for clarity. . . . .	55
4.1	S(2p) XPS spectra of PEDOT:PSS (bottom), as cast (middle) and annealed (top) BHJ films. The BHJ film spectra are of the backside of the film that was in contact with the PEDOT:PSS sub-layer. Dashed lines linearly connect the data at either end of the observed peaks and are guides to the eye. . . . .	70
4.2	(a) 1 <sup>st</sup> heat DSC of PEDOT:PSS showing the release of water on heating. (b) TMDSC total heat flow of BHJ samples annealed on a PEDOT:PSS coated substrate (showing evidence of PSS residue) and in the DSC. Data in (b) shifted vertically for clarity. . . . .	71

4.3	TMDSC thermograms of spun cast BHJ films in the as cast (a) and annealed (b) states along with a drop cast sample (c). Dashed lines illustrate baselines for used for crystallinity and $T_g$ analyses. . . . .	73
4.4	Grazing incidence X-ray diffraction of a BHJ film showing the (100) reflection of P3HT with different annealing temperatures. The same film was annealed for 5 minutes at each temperature. Angle of incidence was fixed at $0.4^\circ$ (Rigaku Ultima IV). . . . .	75
4.5	Optical microscopy images of BHJ films. a) As cast, b) annealed at $140^\circ\text{C}$ for 20 minutes and c) annealed at $175^\circ\text{C}$ for 10 minutes. Images taken with a Nikon Eclipse LV100 microscope equipped with a Nikon DS-Ri1 camera attachment. . . . .	76
4.6	Reversing specific heat capacity (a,b) and the corresponding derivatives (c,d) of Spun:as cast (left column) and Spun:annealed (right column) BHJ films showing the $T_g$ region. . . . .	78
4.7	Graph of glass transition ( $T_g$ ) vs. PCBM mass fraction ( $W_{PCBM}$ ). Shown are the $T_g$ s of the measured samples (filled squares) mapped onto the theoretical trendline and calculated values (open squares) based on the total amorphous fraction in the respective samples. Trendline is from Eq. 4.1 and the filled symbols were used in Table 4.2. . . . .	80
5.1	Reflectivity (a) and SLD (b) profiles of a pure PEDOT:PSS film before and after annealing. Data in (a) were shifted vertically for clarity. . . . .	93
5.2	Reflectivity (a) and SLD (b) profiles of a PEDOT:PSS/P3HT bilayer before and after annealing. Data in (a) were shifted vertically for clarity. . . . .	94
5.3	Reflectivity (a) and SLD (b) profiles of a PEDOT:PSS/PCBM bilayer before and after annealing. Data in (a) was shifted vertically for clarity. . . . .	96
5.4	Chart showing bulk PEDOT:PSS SLD in the pure and bilayer samples. Error bars represent 95% confidence interval calculated during the fitting procedure. . . . .	99

5.5	Chart showing SLD of the PSS-rich surface layer in pure and bilayer samples. Error bars represent 95% confidence interval calculated during the fitting procedure. . . . .	100
6.1	DSC of pure PVP (a) and TMSDC total heat flow of regioregular P3HT films that were annealed on two different sacrificial layers (b). Graphs were shifted vertically for clarity. . . . .	110
6.2	DSC of bulk PBTTT-C14 (a) and PBDTTT-C (b). Dashed line in (a) is drawn to define the broad backbone melting transition of PBTTT-C14. . . . .	112
A.1	TMDSC of pure PCBM. Shown are the total heat flow (a) and reversing specific heat capacity (b) in the $T_g$ region. . . . .	119

## ABSTRACT

Polymer semiconductors are intriguing due to their potential use in flexible electronics. Poly (3-hexylthiophene) (P3HT) is regarded as the workhorse polymer in this field but there is still much to investigate about it. P3HT is also a semicrystalline polymer and it is known that crystalline P3HT has a higher hole mobility than amorphous P3HT. Quantifying each fraction (i.e. the crystalline and amorphous fractions) in the bulk and thin film states is therefore crucial to understanding its performance in transistor and other applications. In its polymer solar cell application, it acts as an electron donor and is typically mixed with the nanoparticle-like molecule, phenyl-C<sub>61</sub>-butyric acid methyl ester (PCBM) – an electron acceptor – in a thin film morphology termed a bulk heterojunction (BHJ). The structural hierarchy within the bulk heterojunction is complicated and its characterization, with a focus on P3HT morphology, is the topic of this dissertation.

Calorimetry can play an important role in the elucidation of P3HT morphology with quantitative analysis of the crystalline and amorphous fractions present in the material. This was demonstrated by employing differential scanning calorimetry (DSC) to obtain the enthalpy of fusion of 100% crystalline P3HT (42.9 J/g) via a simple linear extrapolation process of oligomeric P3HT measurements. A more sensitive temperature modulated DSC (TMDSC) was then used to examine the glass transition of P3HT and it was discovered that the polymer is composed of three phases; crystalline, mobile amorphous and rigid amorphous phases which were quantified. The presence of these phases can play a large role in understanding the charge transfer process in polymer semiconductors as a valence band offset exists between the crystalline and amorphous phases.

BHJ thin films of 50 wt.% PCBM were then analyzed and a polymer crystallinity of 30% was found after thermal annealing from initially non-crystalline polymer material. With assistance from previously acquired small angle neutron scattering data, a thorough analysis of the entire BHJ morphology was accomplished, quantifying all fractions including: PCBM clusters, P3HT crystalline and rigid amorphous fractions and a mixed phase containing mobile amorphous P3HT and dissolved PCBM. A surprisingly large rigid amorphous polymer phase is present in the BHJ suggesting the high hole mobility P3HT crystals may still be separated from the high electron mobility PCBM agglomerates creating recombination zones evident in previous photoluminescence studies.

Finally, interlayer diffusion of PCBM was examined using neutron reflectivity. By measuring the diffusion between bilayers it was found that up to 12% PCBM is able to diffuse into the PEDOT:PSS electron blocking polymer layer. The possible mixing of these two materials is typically ignored but this study suggests that more attention should be paid to diffusion across the PEDOT:PSS/BHJ interface.

# Chapter 1

## INTRODUCTION

### 1.1 Energy Outlook

With the steady decline of coal use for the production of electricity and the continued increase in human energy consumption more energy sources must be implemented into the world's energy portfolio (see Figure 1.1). Renewable energy sources tap into natural and sustainable energy with the potential to fully replace current resources for a lower penalty in CO<sub>2</sub> emissions. As illustrated in Figure 1.1, coal based generation plants will remain constant as renewable generation continues to grow. The end result is an increase in the world's consumption of lower CO<sub>2</sub> emitting, renewable energy over time. According to the 2016 International Energy Outlook Report, "renewable energy is the world's fastest-growing source of energy, at an average rate of 2.6%/year...".[1] Much of the projected energy generation and consumption in Figure 1.1 will come from developing countries as they grow and become more technologically advanced. In contrast, developed nations seek to reduce consumption and lower carbon emissions through energy conservation schemes and the increased installation of renewable energy plants.

With regard to the U.S. plans for lowering carbon emissions, the Clean Power Plan (CPP) from the Environmental Protection Agency (EPA)[2] is a proactive move to bring the United States' CO<sub>2</sub> emissions down by 32% by 2030. To make this a reality, the plan calls for the retirement of many coal fired power plants, replacing them with solar, wind and natural gas as seen in Figure 1.2. Even in the worst case scenario, where the CPP is overturned (No CPP case in Figure 1.2), 60 gigawatts of coal capacity is still scheduled to be replaced by 2020.[3] U.S. energy consumption is

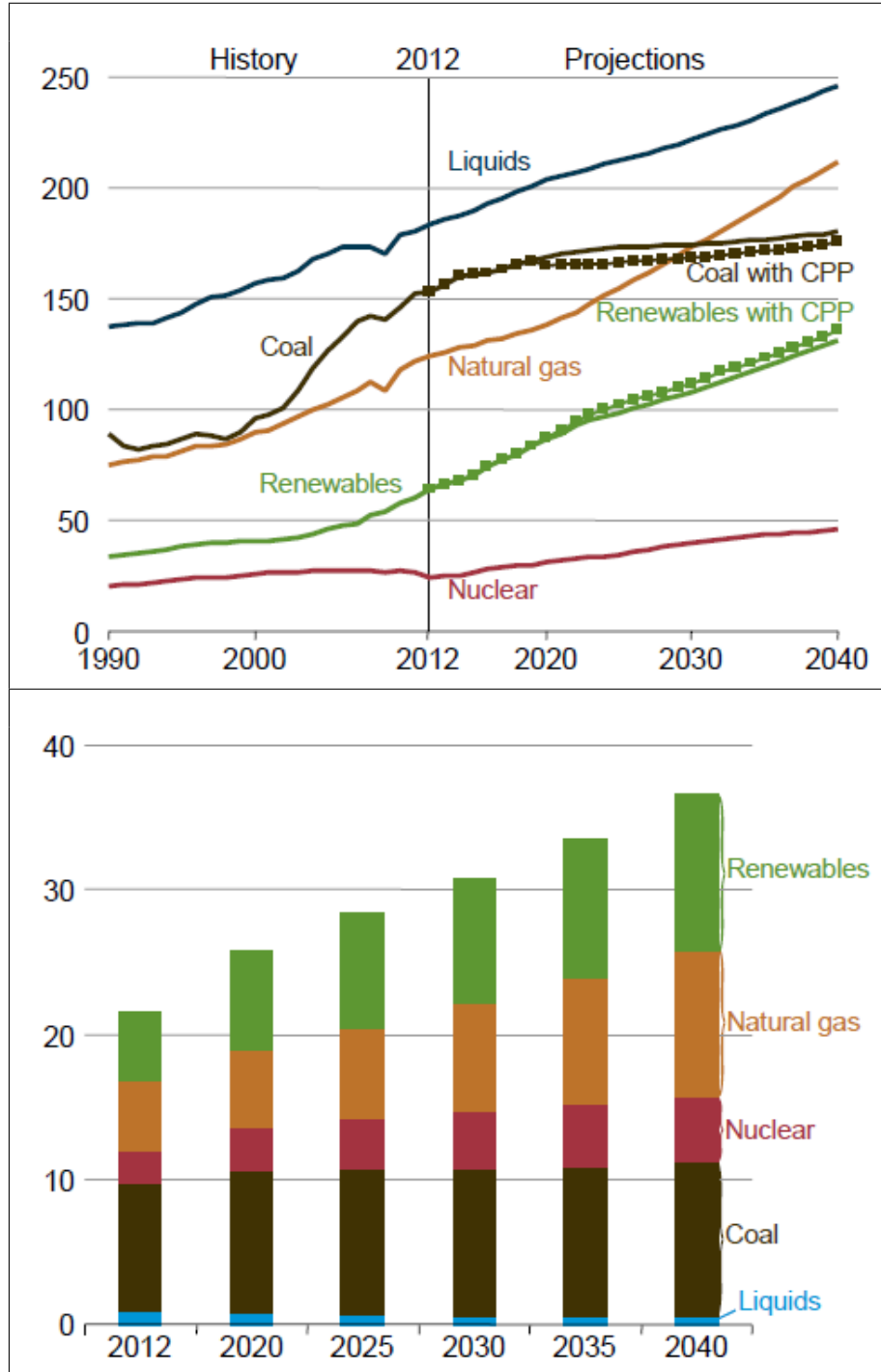


**Figure 1.1:** The top graph show the world’s energy consumption in quadrillion Btu ( $\sim 3 \times 10^{11}$  kilowatthours) by energy source. The bottom graph shows the world’s electricity generation in trillion ( $10^{12}$ ) kilowatthours. Both graphs contain past data as well as projections through 2040.[1]

so large that full adaptation of the CPP will have noticeable global impact. The upper graph of Figure 1.1 demonstrates this by displaying the projected world consumption of coal and renewable energy with and without CPP enactment. It is clear from Figure 1.2 that solar energy will play a major role in america’s – and the world’s by extension – energy generation and consumption through the CPP, especially in the longer term.

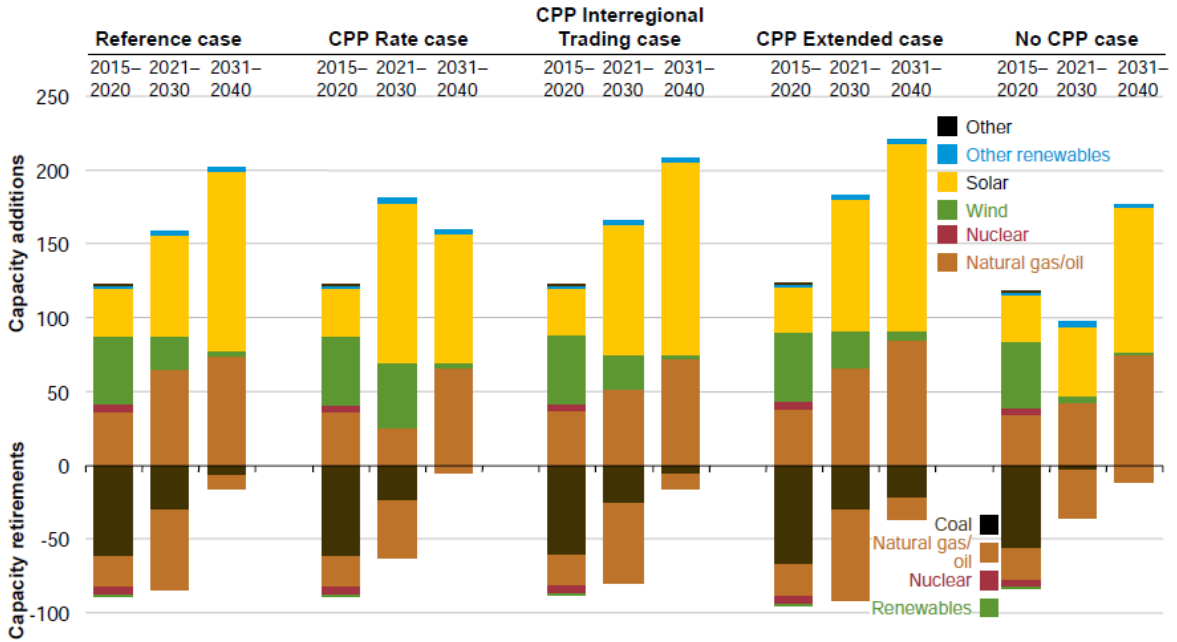


**Figure 1.2:** U.S. plans for installing/retiring generation capacity (in gigawatts) based on the short, mid and long term application of the EPA’s Clean Power Plan.[3]

### 1.2 Solar Cells

With 28,000 terawatts (TW) of solar energy radiating the land mass of the earth, it is understandable why the U.S. has put energy generation from the sun in the forefront of its plans. However, the amount that can be feasibly converted to electricity, for example, is small due to land use, cost and conversion efficiency.[4] To the last point, much research has gone into increasing the efficiency of photovoltaic devices (i.e. solar cells) and development of new photosensitive materials over the years. A comprehensive efficiency trend of the major materials types is shown in Figure 1.3 to illustrate

this. The upper material efficiency limit is  $\sim 30\%$  (known as the Shockley-Queisser limit[5]) and is based on thermodynamic arguments. Currently, this is almost achieved in single junction solar cells made from GaAs, single crystal Silicon and CIGS. This technological achievement has spurred the upscaling and commercialization of many of these materials. Those above the Shockley-Queisser limit in Figure 1.3 are multi-junction devices that typically consists of two or more absorber layers or concentrators that multiply the sun's intensity before reaching the device.

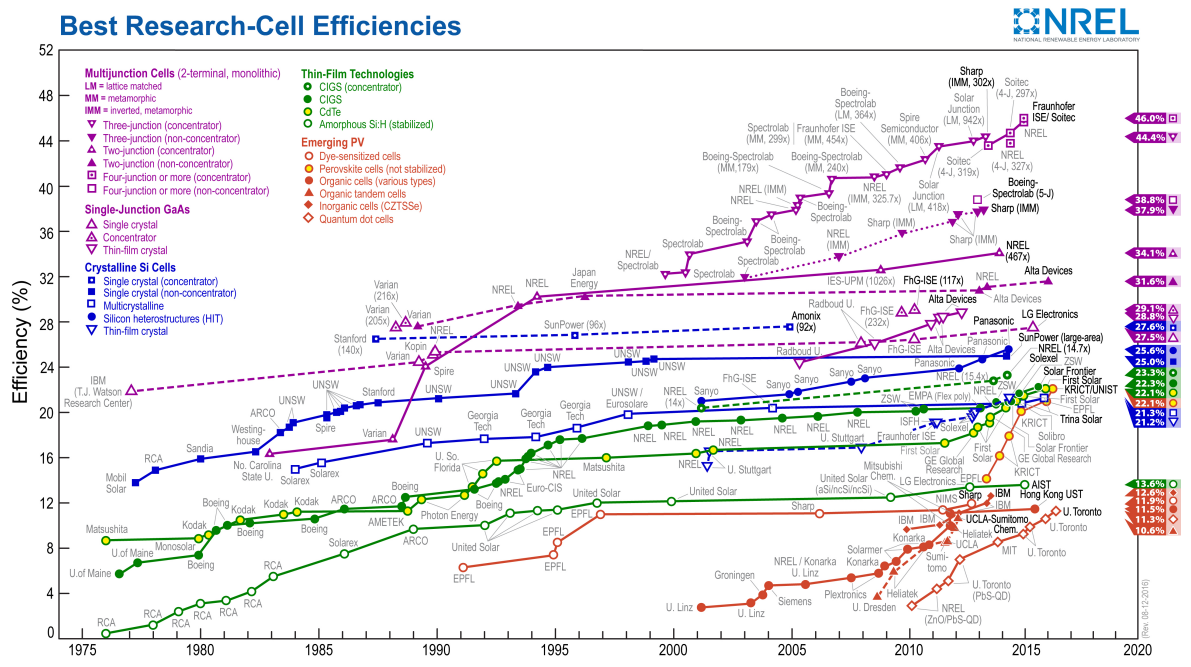


Figure 1.3: Graph showing best laboratory scale solar device efficiencies over time, by material class. This plot is courtesy of the National Renewable Energy Laboratory, Golden, CO.

### 1.3 Organic/Polymer based Solar Cells

On the lower end of Figure 1.3 lies organic solar cells (OSCs) which include polymer based solar cells. Obviously, more advancements need to occur for organic devices to compete with the more mature inorganic ones. However OSCs have other advantages to inorganic devices including the use of less material in the absorber layer for an

equal amount of light absorption, potentially leading to lower materials cost overall.[4] In the same trend, the levelized cost of electricity (LCOE  $\sim$  \$0.13/kWh)[6] and energy payback time (EPBT  $\sim$  2 years)[4] have also been shown to be competitive or even better than inorganics. Interestingly, the LCOE and EPBT were calculated using efficiency assumptions 2 – 4%. Imagine the possibilities if the current, high efficiency ( $>$  10%) polymer solar cells can be economically upscaled and commercialized![7, 8]

Recent steps toward upscaling polymer solar cells has, almost single-handedly, been taken by the Krebs research group. Using the well-known poly(3-hexylthiophene) (P3HT):fullerene absorbing materials, the Krebs group has produced large area devices from commercial roll-to-roll processing technologies.[9–12] In addition, extensive lifetime and stability testing have been performed leading to better understandings of the challenges of upscaling and environmental degradation on polymer solar cells.[13–19] With such a promising future for polymer based solar cells, it is imperative that the research community continues to investigate the properties of these devices, including their morphology, to optimize performance and stability in the hope of better upscaling capability.

### 1.3.1 Device Architecture and Morphology

The polymer solar device structure has been through a few iterations as can be seen in Figure 1.4. The active layer (i.e. the layer containing the main light absorbing material(s)) was improved by adding an electron accepting material to enhance the charge separation and extraction process, thereby increasing photoconversion efficiency. Figure 1.4d shows the theoretical optimal active layer morphology (called a heterojunction) by considering factors such as total layer thickness for maximum light absorption, exciton diffusion length<sup>1</sup> and optimal donor-acceptor ratio. Due to these factors the optimal structure consists of comb-like structures of donor and acceptor that are interdigitated with thin layers of pure material at the respective electrodes.

---

<sup>1</sup> An exciton is an electrostatically bound electron and hole pair. This close binding means that the diffusion length is quite short  $\sim$  10 nm in polymer semiconductors.[20]

Each ‘tooth’ of the comb is on the order of 10 nm wide and 100 nm long: an extremely difficult structure to fabricate with polymer materials. Thus a different solution was proposed where the two materials are mixed in a common solvent and then deposited onto the substrate (i.e. one of the electrodes). The interaction between the two materials and the solvent will cause nanoscale phase separation and create what it termed a bulk heterojunction (BHJ), a depiction of which is in Figure 1.4c. Due to the simplicity of fabrication of the BHJ it has been adapted as the standard strategy for creating the active layer of polymer solar cells.

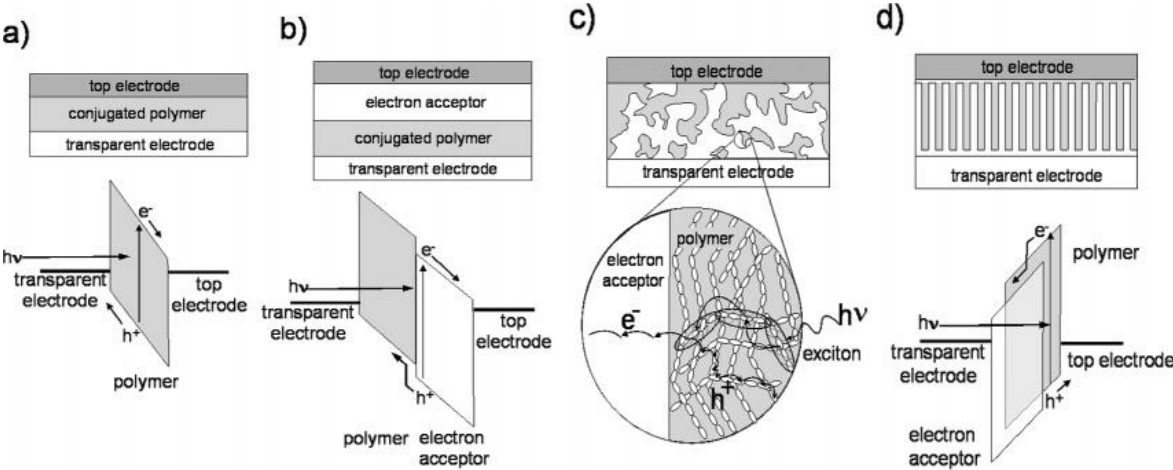


**Figure 1.4:** Illustrations of different polymer solar cell morphologies. A single conjugated polymer sandwiched between two electrodes (a). A layered structure of polymer donor and electron acceptor (b). A bulk heterojunction structure (c). An optimized heterojunction structure (d). Reprinted from Ref. [21] with permission from the American Chemical Society.

In this dissertation the morphology of a BHJ comprised of P3HT and the fullerene derivative phenyl-C<sub>61</sub>-butyric acid methyl ester (PCBM) is investigated as described in the following section. The basic components of a P3HT:PCBM device is illustrated in Figure 1.5. A thin layer ( $\sim 40$  nm) of poly(3,4-ethylene-dioxythiophene) (PEDOT):poly(styrenesulfonate) (PSS) is typically deposited between the BHJ and the transparent conducting electrode (typically indium tin oxide) as an electron blocker. The unique properties of PEDOT:PSS allow it to easily conduct holes, block electrons

and have little parasitic light absorption.[22–24] This makes PEDOT:PSS one of the most difficult materials to replace in the device. In the BHJ, the majority of light absorption occurs in P3HT, where the exciton is formed and diffuses around until it either finds a P3HT:PCBM interface where the electron is transferred to PCBM (as shown in Figure 1.5) or it recombines to create heat.

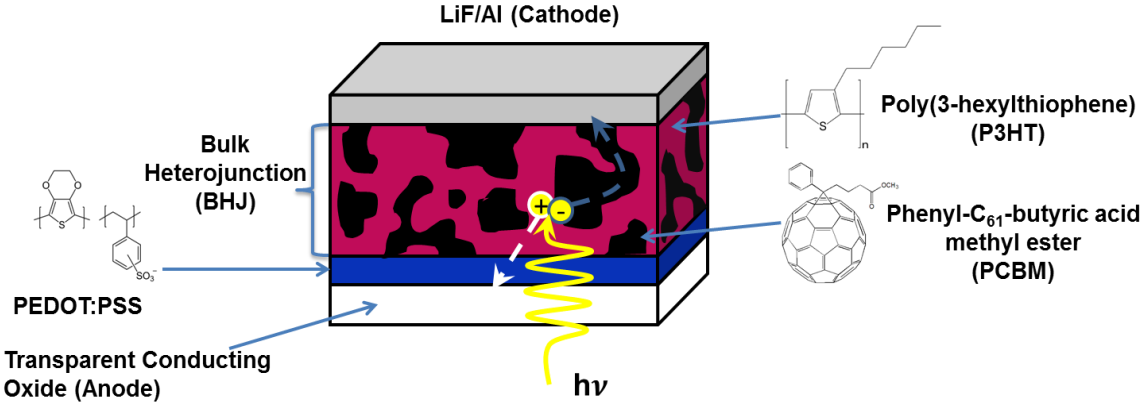


**Figure 1.5:** A diagram of the conventional P3HT:PCBM bulk heterojunction solar cell.

Since the length scales of the BHJ are on the order of nanometers, models were developed to visualize the morphology. These models typically come from small angle neutron scattering,[25–27] neutron reflectivity,[28–30] and X-ray spectroscopy[31–33] with a few from X-ray diffraction as well.[34] A summary of the findings describe the BHJ morphology as bi-continuous with agglomerated PCBM forming one of the continuous phases and a mixture of crystalline P3HT, amorphous P3HT and dissolved PCBM forming the other. This morphology provides high mobility pathways for electron and hole transport from anywhere in the film to their respective electrodes. The interfaces to contain high PCBM concentrations which is only good at the cathode where electrons are transported out of the device. Studies suggest that modification of the surface energy of the adjacent layers can mediate this.[33, 35]

## 1.4 Thesis Outline

Research on polymer based solar cells in the Mackay group has spanned a decade or so. It has mainly been directed towards employing neutron scattering as a fundamental tool to investigate the morphology of the polymer bulk heterojunction (BHJ). Neutron scattering however, has its limits. This thesis seeks to contribute to the understanding of the polymer BHJ by developing calorimetric methods to quantitatively analyze it. This will supplement the knowledge gained from neutron scattering by focusing on the polymer (P3HT) phases rather than the nanoparticle (PCBM) agglomeration.

**Chapter 2** has discussion of a straightforward way of determining the enthalpy of fusion of P3HT using differential scanning calorimetry (DSC), which can be broadly applied to other polymers. Without the enthalpy of fusion, the methods developed after this chapter could only be qualitative, some even impossible.

**Chapter 3** has an introduction to temperature modulated DSC (TMDSC) as a more sensitive technique for the investigation of the weak glass transition of P3HT. This investigation produced a quantitative three phase model for bulk P3HT and applied it to spun cast P3HT thin films as well.

**Chapter 4** has a focus on bulk heterojunction thin films and applies TMDSC in a similar manner to Chapter 3. The complications of annealing on PEDOT:PSS are first highlighted and a solution proposed. Then the crystallinity of the BHJ is calculated. In combination with previous scattering results from our research group a new, comprehensive, four phase BHJ model is proposed with individual donor and acceptor fractions calculated.

**Chapter 5** has an introduction to neutron reflectivity and interfacial characterization. Polymer bilayers are fabricated with PEDOT:PSS being the base layer. There is little research on the diffusion of both P3HT and PCBM into PEDOT:PSS that this chapter addresses. By examining the thermal diffusion of the individual BHJ components into PEDOT:PSS, a proper analysis can be accomplished.

**Chapter 6** is written to summarize the work laid out in this thesis its main

take away points. In addition, it presents directions for furthering the methodology and important areas of focus for future research in polymer photovoltaics.

## BIBLIOGRAPHY

- [1] U.S. Energy Information Administration - International Energy Outlook 2016.
- [2] Environmental Protection Agency - Clean Power Plan.
- [3] U.S. Energy Information Administration - Annual Energy Outlook 2016.
- [4] Seth B. Darling and Fengqi You. The case for organic photovoltaics. *RSC Adv.*, 3(39):17633, 2013.
- [5] William Shockley and Hans J. Queisser. Detailed Balance Limit of Efficiency of p-n Junction Solar Cells. *J. Appl. Phys.*, 32(3):510, 1961.
- [6] Cara J. Mulligan, Chhinder Bilen, Xiaojing Zhou, Warwick J. Belcher, and Paul C. Dastoor. Levelised cost of electricity for organic photovoltaics. *Sol. Energy Mater. Sol. Cells*, 133:26–31, feb 2015.
- [7] Yuhang Liu, Jingbo Zhao, Zhengke Li, Cheng Mu, Wei Ma, Huawei Hu, Kui Jiang, Haoran Lin, Harald Ade, and He Yan. Aggregation and morphology control enables multiple cases of high-efficiency polymer solar cells. *Nat. Commun.*, 5:5293, nov 2014.
- [8] Wenchao Zhao, Deping Qian, Shaoqing Zhang, Sunsun Li, Olle Inganäs, Feng Gao, and Jianhui Hou. Fullerene-Free Polymer Solar Cells with over 11% Efficiency and Excellent Thermal Stability. *Adv. Mater.*, apr 2016.
- [9] Frederik C. Krebs. Fabrication and processing of polymer solar cells: A review of printing and coating techniques. *Sol. Energy Mater. Sol. Cells*, 93(4):394–412, apr 2009.
- [10] Gisele A. dos Reis Benatto, Bérenger Roth, Morten V. Madsen, Markus Hösel, Roar R. Søndergaard, Mikkel Jørgensen, and Frederik C. Krebs. Carbon: The Ultimate Electrode Choice for Widely Distributed Polymer Solar Cells. *Adv. Energy Mater.*, 4(15):n/a–n/a, oct 2014.

- [11] Eva Bundgaard, Francesco Livi, Ole Hagemann, Jon E. Carlé, Martin Helgesen, Ilona M. Heckler, Natalia K. Zawacka, Dechan Angmo, Thue T. Larsen-Olsen, Gisele A. dos Reis Benatto, Bérenger Roth, Morten V. Madsen, Mats R. Andersson, Mikkel Jørgensen, Roar R. Søndergaard, and Frederik C. Krebs. Matrix Organization and Merit Factor Evaluation as a Method to Address the Challenge of Finding a Polymer Material for Roll Coated Polymer Solar Cells. *Adv. Energy Mater.*, 5(10):n/a–n/a, feb 2015.
- [12] Rafael Garcia-Valverde, José A. Villarejo, Markus Hösel, Morten V. Madsen, Roar R. Søndergaard, Mikkel Jørgensen, and Frederik C. Krebs. Scalable single point power extraction for compact mobile and stand-alone solar harvesting power sources based on fully printed organic photovoltaic modules and efficient high voltage DC/DC conversion. *Sol. Energy Mater. Sol. Cells*, 144:48–54, jan 2016.
- [13] Suren a. Gevorgyan, Mikkel Jørgensen, Frederik C. Krebs, and Kristian O. Sylvester-Hvid. A compact multi-chamber setup for degradation and lifetime studies of organic solar cells. *Sol. Energy Mater. Sol. Cells*, 95(5):1389–1397, may 2011.
- [14] Matthew O. Reese, Suren A. Gevorgyan, Mikkel Jørgensen, Eva Bundgaard, Sarah R. Kurtz, David S. Ginley, Dana C. Olson, Matthew T. Lloyd, Pasquale Morvillo, Eugene A. Katz, Andreas Elschner, Olivier Haillant, Travis R. Currier, Vishal Shrotriya, Martin Hermenau, Moritz Riede, Kiril R. Kirov, Gregor Trimmel, Thomas Rath, Olle Inganäs, Fengling Zhang, Mattias Andersson, Kristofer Tvingstedt, Monica Lira-Cantu, Darin Laird, Christine McGuinness, Srinivas (Jimmy) Gowrisanker, Michael Pannone, Min Xiao, Jens Hauch, Roland Steim, Dean M. DeLongchamp, Roland Rösch, Harald Hoppe, Nieves Espinosa, Antonio Urbina, Gülsah Yaman-Uzunoglu, Jörg-Bernd Bonekamp, Albert J.J.M.

- van Breemen, Claudio Girotto, Eszter Voroshazi, and Frederik C. Krebs. Consensus stability testing protocols for organic photovoltaic materials and devices. *Sol. Energy Mater. Sol. Cells*, 95(5):1253–1267, 2011.
- [15] David M. Tanenbaum, Martin Hermenau, Eszter Voroshazi, Matthew T. Lloyd, Yulia Galagan, Birger Zimmermann, Markus Hösel, Henrik F. Dam, Mikkel Jørgensen, Suren A. Gevorgyan, Suleyman Kudret, Wouter Maes, Laurence Lutsen, Dirk Vanderzande, Uli Würfel, Ronn Andriessen, Roland Rösch, Harald Hoppe, Gerardo Teran-Escobar, Monica Lira-Cantu, Agnès Rivaton, Gülsah Y. Uzunoglu, David Germack, Birgitta Andreasen, Morten V. Madsen, Kion Norrman, and Frederik C. Krebs. The ISOS-3 inter-laboratory collaboration focused on the stability of a variety of organic photovoltaic devices. *RSC Adv.*, 2(3):882–893, 2012.
- [16] Roland Rösch, David M. Tanenbaum, Mikkel Jørgensen, Marco Seeland, Maik Bärenklau, Martin Hermenau, Eszter Voroshazi, Matthew T. Lloyd, Yulia Galagan, Birger Zimmermann, Uli Würfel, Markus Hösel, Henrik F. Dam, Suren A. Gevorgyan, Suleyman Kudret, Wouter Maes, Laurence Lutsen, Dirk Vanderzande, Ronn Andriessen, Gerardo Teran-Escobar, Monica Lira-Cantu, Agnès Rivaton, Gülsah Y. Uzunoglu, David Germack, Birgitta Andreasen, Morten V. Madsen, Kion Norrman, Harald Hoppe, and Frederik C. Krebs. Investigation of the degradation mechanisms of a variety of organic photovoltaic devices by combination of imaging techniques – the ISOS-3 inter-laboratory collaboration. *Energy Environ. Sci.*, 5(4):6521, 2012.
- [17] Gerardo Teran-Escobar, David M. Tanenbaum, Eszter Voroshazi, Martin Hermenau, Kion Norrman, Matthew T. Lloyd, Yulia Galagan, Birger Zimmermann, Markus Hösel, Henrik F. Dam, Mikkel Jørgensen, Suren Gevorgyan, Suleyman Kudret, Wouter Maes, Laurence Lutsen, Dirk Vanderzande, Uli Würfel, Ronn Andriessen, Roland Rösch, Harald Hoppe, Agnès Rivaton, Gülsah Y. Uzunoglu,

- David Germack, Birgitta Andreasen, Morten V. Madsen, Eva Bundgaard, Frederik C. Krebs, and Monica Lira-Cantu. On the stability of a variety of organic photovoltaic devices by IPCE and in situ IPCE analyses – the ISOS-3 inter-laboratory collaboration. *Phys. Chem. Chem. Phys.*, 14(33):11824, 2012.
- [18] Birgitta Andreasen, David M. Tanenbaum, Martin Hermenau, Eszter Voroshazi, Matthew T. Lloyd, Yulia Galagan, Birger Zimmermann, Suleyman Kudret, Wouter Maes, Laurence Lutsen, Dirk Vanderzande, Uli Würfel, Ronn Andriessen, Roland Rösch, Harald Hoppe, Gerardo Teran-Escobar, Monica Lira-Cantu, Agnès Rivaton, Gülsah Y. Uzunoglu, David S. Germack, Markus Hösel, Henrik F. Dam, Mikkel Jørgensen, Suren A. Gevorgyan, Morten V. Madsen, Eva Bundgaard, Frederik C. Krebs, and Kion Norrman. TOF-SIMS investigation of degradation pathways occurring in a variety of organic photovoltaic devices – the ISOS-3 inter-laboratory collaboration. *Phys. Chem. Chem. Phys.*, 14(33):11780, 2012.
- [19] Christopher J.M. Emmott, Davide Moia, Philip Sandwell, Nicholas Ekins-Daukes, Markus Hösel, Lukas Lukoschek, Charith Amarasinghe, Frederik C. Krebs, and Jenny Nelson. In-situ, long-term operational stability of organic photovoltaics for off-grid applications in Africa. *Sol. Energy Mater. Sol. Cells*, 149:284–293, may 2016.
- [20] J. Frenkel. On the Transformation of light into Heat in Solids. I. *Phys. Rev.*, 37(1):17–44, jan 1931.
- [21] Kevin M. Coakley and Michael D. McGehee. Conjugated Polymer Photovoltaic Cells. *Chem. Mater.*, 16(23):4533–4542, nov 2004.
- [22] Qibing Pei, Guido Zuccarello, M Ahlskog, and O Inganas. Electrochromic and highly stable poly (3, 4-ethylenedioxythiophene) switches between opaque blue-black and transparent sky blue. *Polymer*, 35(7):1347–1351, 1994.

- [23] Jaehyung Hwang, Fabrice Amy, and Antoine Kahn. Spectroscopic study on sputtered PEDOT:PSS: Role of surface PSS layer. *Org. Electron.*, 7(5):387–396, oct 2006.
- [24] Annika Lenz, Hans Kariis, Anna Pohl, Petter Persson, and Lars Ojamäe. The electronic structure and reflectivity of PEDOT:PSS from density functional theory. *Chem. Phys.*, 384(1-3):44–51, jun 2011.
- [25] Jonathon Kiel, Aaron Eberle, and Michael Mackay. Nanoparticle Agglomeration in Polymer-Based Solar Cells. *Phys. Rev. Lett.*, 105(16):1–4, oct 2010.
- [26] Wen Yin and Mark Dadmun. A New Model for the Morphology of P3HT/PCBM Organic Photovoltaics from Small Angle Neutron Scattering: Rivers and Streams. *ACS Nano*, 5(6):4756–4768, 2011.
- [27] Hao Shen, Wenluan Zhang, and Michael E. Mackay. Dual length morphological model for bulk-heterojunction, polymer-based solar cells. *J. Polym. Sci. Part B Polym. Phys.*, 52(5):387–396, mar 2014.
- [28] Jonathan W. Kiel, Brian J. Kirby, Charles F. Majkrzak, Brian B. Maranville, and Michael E. Mackay. Nanoparticle concentration profile in polymer-based solar cells. *Soft Matter*, 6(3):641–646, 2010.
- [29] J W Kiel, M E Mackay, B J Kirby, B B Maranville, and C F Majkrzak. Phase-sensitive neutron reflectometry measurements applied in the study of photovoltaic films. *J. Chem. Phys.*, 133(7):074902, aug 2010.
- [30] Huipeng Chen, Raghavendra Hegde, J Browning, and M D Dadmun. The miscibility and depth profile of PCBM in P3HT: thermodynamic information to improve organic photovoltaics. *Phys. Chem. Chem. Phys.*, mar 2012.
- [31] Benjamin Watts, Warwick J. Belcher, Lars Thomsen, Harald Ade, and Paul C. Dastoor. A Quantitative Study of PCBM Diffusion during Annealing of P3HT:PCBM Blend Films. *Macromolecules*, 42(21):8392–8397, nov 2009.

- [32] David S. Germack, Calvin K. Chan, Behrang H. Hamadani, Lee J. Richter, Daniel A. Fischer, David J. Gundlach, and Dean M. DeLongchamp. Substrate-dependent interface composition and charge transport in films for organic photovoltaics. *Appl. Phys. Lett.*, 94(23):233303, 2009.
- [33] David S. Germack, Calvin K. Chan, R. Joseph Kline, Daniel A. Fischer, David J. Gundlach, Michael F. Toney, Lee J. Richter, and Dean M. DeLongchamp. Interfacial Segregation in Polymer/Fullerene Blend Films for Photovoltaic Devices. *Macromolecules*, 43(8):3828–3836, apr 2010.
- [34] Neil D. Treat, Chris G. Shuttle, Michael F. Toney, Craig J. Hawker, and Michael L. Chabinyo. In situ measurement of power conversion efficiency and molecular ordering during thermal annealing in P3HT:PCBM bulk heterojunction solar cells. *J. Mater. Chem.*, 21(39):15224, sep 2011.
- [35] David S. Germack, Antonio Checco, and Benjamin M. Ocko. Directed Assembly of P3HT:PCBM Blend Films Using A Chemical Template with Sub-300 nm Features. *ACS Nano*, 7(3):1990–1999, mar 2013.

## Chapter 2

### A FACILE CALCULATION OF THE ENTHALPY OF FUSION OF POLY(3-HEXYLTHIOPHENE)

Adapted with permission from Remy, R.; Weiss, E. D.; Nguyen, N. A.; Wei, S.; Campos, L. M.; Kowalewski, T.; Mackay, M. E. *J. Polym. Sci. Part B Polym. Phys.* 2014, 52, 1469–1475. Copyright 2014 John Wiley and Sons.

#### 2.1 Introduction

Semiconducting polymers have been of interest to the scientific community due to their applications in electronic and photovoltaic devices. Poly(3-hexylthiophene) (P3HT) is a semicrystalline polymer and is one of the most widely studied of the semiconducting polymers due to its high charge carrier mobility.[1, 2] It has been utilized as the main component in organic field effect transistors (OFETs)[3, 4] and solar cells (OSCs) for a number of years. In both OFETs and OSCs, knowing and tuning the morphology (crystallinity and crystal orientation) of P3HT is vital to optimize its transport properties.

An advantage to semiconducting polymers, like P3HT, is their ability to be fabricated via solution casting with low cost technologies such as spin, roll to roll[5, 6] and spray coating.[7, 8] Solution processing allows for deposition on different substrates (including flexible ones) and less material is required in production as compared to their semi-metallic counterparts like silicon. Current research has seen OSC efficiencies reach over 11%.[9] OSCs are typically made of a semiconducting polymer and an electron accepting material, with the most commonly studied donor/acceptor system being P3HT and the electron acceptor phenyl-C<sub>61</sub>-butyric methyl ester (PCBM). They are

mixed in a common solvent and deposited to create an active layer described as a bulk heterojunction (BHJ).

Despite continued advancement in the development of OSCs, much is still unknown on the relation between the morphology of the BHJ and processing conditions. Researchers have realized annealing the BHJ above its glass transition temperature improves the efficiency by causing two major nanoscale changes in the BHJ. First, annealing causes the PCBM to diffuse and agglomerate which leads to improved electron transport through the film.[9–15] Second, X-ray diffraction shows that the crystallinity of P3HT increases from the unannealed to the annealed case.[5, 11, 16–18] While X-ray diffraction has provided a useful comparison of pre and post-annealing P3HT crystallinity, it is difficult to determine absolute crystallinity from this data, although a recent attempt at this has been accomplished.[19]

Moreover, to determine absolute crystallinity of a semicrystalline polymer, one must have a reference point from which to begin. For semicrystalline materials a convenient reference point is the enthalpy of fusion ( $\Delta H_m^\infty$ ), which is the amount of energy (per gram) that is required to melt a *perfect, infinite* crystal of that material. This provides a maximum value from which all other crystals of that material can be compared, to determine their level of perfection, i.e. crystallinity. The difficulties of making such a crystal of a semiconducting polymer are well known[20] and only one successful report has been published to date.[21] Typically, this value is attained through indirect experimentation and theoretical analysis. Malik and Nandi[22] were first to acquire a value of  $\Delta H_m^\infty = 99$  J/g for P3HT. Pascui et al.[23] contested this value stating  $\Delta H_m^\infty = 37$  J/g is a better estimate based on their  $^{13}\text{C}$  solid state nuclear magnetic resonance (NMR) results. Later, Snyder et al.[24] postulated  $\Delta H_m^\infty = 50$  J/g using a combination of  $^{13}\text{C}$ -NMR and differential scanning calorimetry (DSC). Analysis of monodisperse 100% regioregular oligo(3-hexylthiophene)s by Koch et al.[25, 26] resulted in a clear definition of  $\Delta H_m^\infty = 39$  J/g for Form I crystals and  $\Delta H_m^\infty = 99$  J/g for the less stable Form II crystals, lending credibility to the results from Malik and Nandi and Pascui et al. Finally, Lee and Dadmun[27] defined limits of the

Form I P3HT crystal as 37 – 50 J/g by examining P3HT amorphous and crystalline densities using helium pycnometry and DSC. While  $\Delta H_m^\infty$  for the Form I P3HT crystal is being narrowed, many of the techniques are complicated and some require very specific samples to be made.

A simple, alternative method to determine  $\Delta H_m^\infty$  for P3HT is described in this study. The method is derived from that utilized by Dole et al.[28] and Billmeyer[29] to evaluate  $\Delta H_m^\infty$  for linear polyethylene within 95% accuracy, or two sigma standard deviation. By taking data from differential scanning calorimetry (DSC) experiments for a range of polymer molecular weights, one can employ a simple linear extrapolation to obtain  $\Delta H_m^\infty$  for any polymer of interest. Here, this analysis is performed with P3HT and comparison to the results stated above is made. In addition, the onset of chain folding within P3HT crystallites is highlighted based on measurements taken from transmission electron microscopy (TEM) images of the crystals cast from solution. Finally, a modification to  $\Delta H_m^\infty$  based on the crystalline fraction within the samples is performed which increases the accuracy of the DSC result.

## 2.2 Experimental

Two types of regioregular poly(3-hexylthiophene) were used in this work. The first was synthesized via Grignard metathesis polymerization[30, 31] and four highly regioregular molecular weights were produced as described in Table 2.1. The second was an electronic grade commercial sample (labeled CS) purchased from Luminescence Technologies Corp (see Table 2.1). The commercial sample was used without further purification.

Poly(3-hexylthiophene) (P3HT) head-to-tail (HT) ratio, known as regioregularity, is calculated by a method described by McCullough et al.[32, 33] As an example, the analysis of regiorandom P3HT is described here (see Figure 2.1). The major peak at 6.98ppm was assigned as HT-HT aromatic proton, and its integrated value was assigned as 1; the other three peaks at 7.01, 7.03, 7.05 ppm were assigned as non HT-HT

**Table 2.1:** Characteristics of P3HT used in this paper.

Sample Designation	Number average degree of polymerization (DP)	Molecular Weight (g/mol) <sup>a</sup>	PDI <sup>b</sup>	Regioregularity (%) <sup>c</sup>
DP31	31	5146	1.20	98.8%
DP47	47	7802	1.10	97.3%
DP62	62	10292	1.11	98.3%
DP66	66	10956	1.11	98.9%
CS	271	45000	>2	>95%

<sup>a</sup>Calculated from number average degree of polymerization from NMR and monomer molecular weight (166 g/mol). <sup>b</sup>Polydispersity Index from GPC. <sup>c</sup>Calculated from H<sup>1</sup> NMR (see below)

aromatic peaks, and their integration is 0.79. Therefore the regioregularity was determined to be 56% =  $1/(1 + 0.79)$ . This number is consistent with reported values in the literature for samples made with FeCl<sub>3</sub>, which is between 50-70%.<sup>[34]</sup> The chemical resonances upfield of the aromatic protons are attributed to the methylene protons of the hexyl side chain of P3HT and are not used in this analysis. The regioregularity of all samples employed here were calculated in this manner.

A TA Instruments Discovery DSC equipped with an RCS90 cooling accessory was employed for all differential scanning calorimetry experiments. Baseline calibration was performed with sapphire disks while the temperature and the cell constant were calibrated using an indium standard. Empty cell baseline variation was within 10  $\mu$ W over ten cycles after calibration. Standard DSC experiments were performed at 10  $^{\circ}$ C/min heating and cooling rates with a 50 mL/min nitrogen cell purge flow. Three heating and cooling cycles were performed. The second and third heats were almost identical while the first heat showed some effect of the unknown thermal history of the sample. The third heat data was analyzed and is reported in this work.

Transmission electron microscopy (TEM) was performed using a JEM-2010f high resolution TEM. Samples for the TEM study were prepared by depositing a 0.4 mg/ml toluene solution of each P3HT sample onto carbon supported copper TEM grids

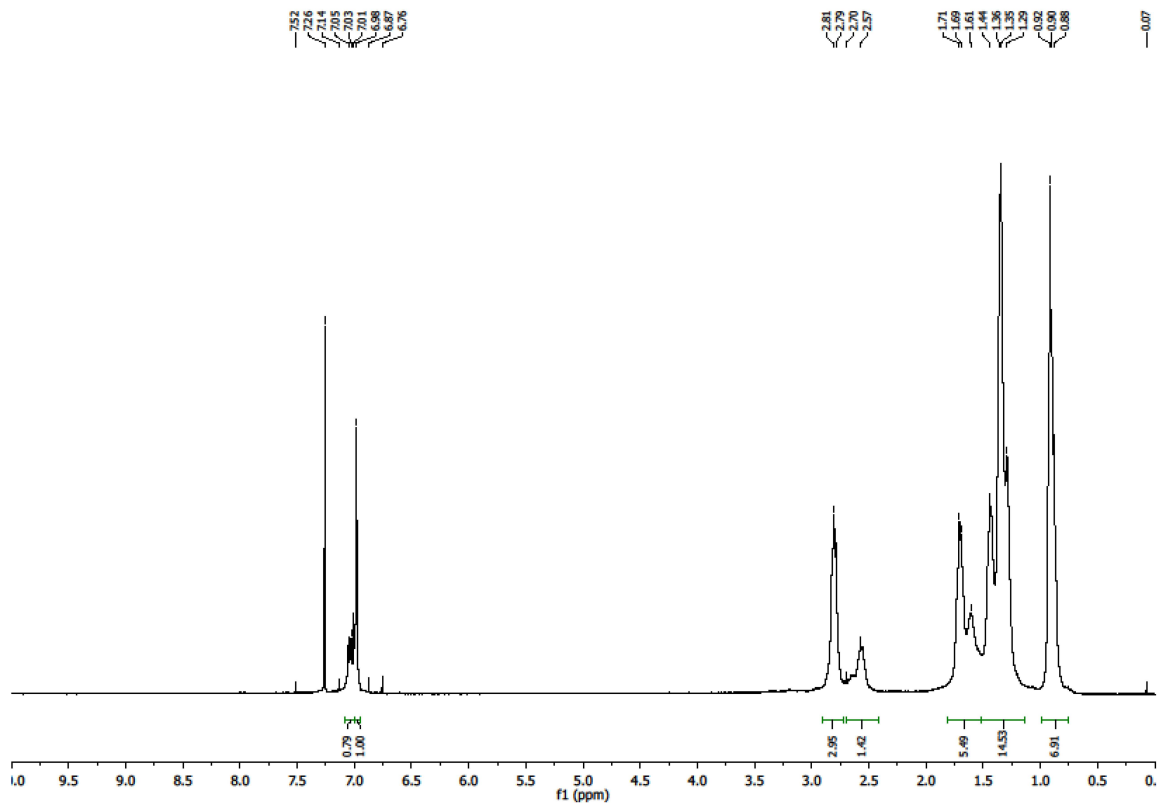


**Figure 2.1:**  $H^1$  NMR of regiorandom P3HT illustrating the process of calculating regioregularity in the P3HT samples employed in this work.

and allowing the solvent to evaporate overnight.

The grazing incidence x-ray scattering images were taken at the Cornell High Energy Synchrotron Source (CHESS) D1 station. A wide bandpass (1.47%) double-bounce multilayer monochromator supplied an intense beam of 10.1 keV photons. These impinged onto the sample surface at various incident angles ranging from below the critical angle of the film and above the critical angle of the substrate. Samples were mounted on a sample goniometer to control the incident angle and the sample azimuth. An accurate calibration of the incident angle was performed in-situ by measuring the X-ray reflectivity from the sample using an ion chamber. Scattering intensities were recorded with an area detector (Medoptics) with a resolution of 47.19  $\mu\text{m}$  per pixel and a total area of about 50 mm by 50 mm at distance of 1180 mm from the sample

for small angle (GISAXS) and at distance of 91 mm from the sample for wide angle (GIWAXS) analysis. The intense scattering in the incident plane was blocked with a 1.5 mm wide tantalum rod. Exposure times under these conditions ranged from 0.03 sec to 0.04 sec for GISAXS and 1.0 sec to 1.5 sec for GIWAXS, depending on the sample scattering intensity.

X-ray reflectivity (XRR) was performed on a regiorandom P3HT thin film sample using a Rigaku Ultima IV X-ray machine with a Cu K $\alpha$  (1.54 Å) source. The sample was prepared by spin casting onto a cleaned silicon wafer from a 30 mg/mL chlorobenzene solution. Regiorandom P3HT was synthesized according to the literature[34], with the result having a molecular weight ( $M_n$ ) = 21.6 kg/mol, PDI = 2.0 (by GPC) and 56% head-to-tail coupling (see H<sup>1</sup> NMR above).

## 2.3 Results and Discussion

### 2.3.1 DSC Analysis

The DSC heat flow curves of the P3HT samples are shown in Figure 2.2(a) and are normalized to the mass of the sample. The melting transition of DP31 occurs at the lowest temperature while the melting transition of the other samples occur at higher temperatures. It is also observed, with the exception of DP31, that there are multiple peaks for each endotherm. This is likely due to chain reorganization and crystal perfection that occurred while heating each sample through its melting transition. This phenomenon, called irreversible (or non-equilibrium) melting, has been well documented for polymers.[35, 36] Figures 2.2(b) and (c) show grazing incidence wide angle scattering (GIWAXS) data of DP31 and DP66 samples, respectively, along with their in plane and out of plane line profiles. Only (h00) reflections corresponding to the Form I P3HT crystal can be observed in the out of plane profile for both samples ( $d_{100} = 1.5$  nm for each). This is supported by the d-spacing of the (020) pi-pi stacking peak observed from the in plane profiles ( $d_{020} = 0.379$  nm and 0.375 nm, respectively) and the melting range observed in the DSC graphs of Figure 2.2(a).[25] Consequently, the calculation of  $\Delta H_m^\infty$  in this work will be only related to the Form I P3HT crystal.

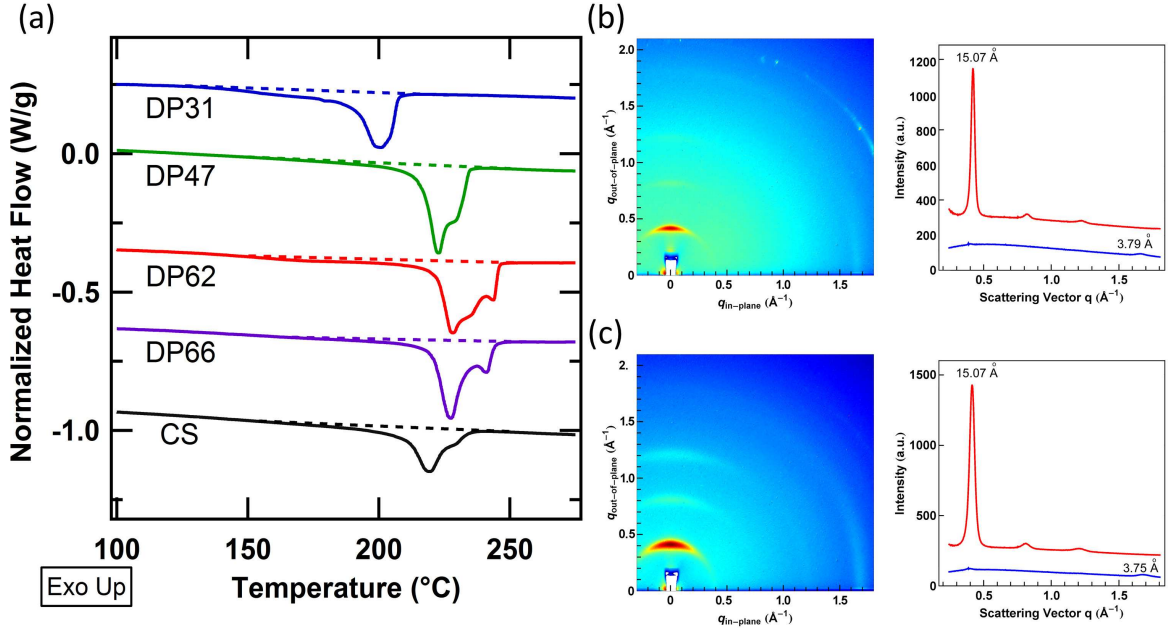


**Figure 2.2:** (a) DSC thermograms of the different P3HT samples used in this work. Dashed lines are tangents drawn to illustrate the integrated area for each sample. Graphs shifted vertically for clarity. GIWAXS data and their associated in (red) and out (blue) of plane line profiles of (b) DP31 and (c) DP66 samples.

Each melting endotherm in Figure 2.2(a) was processed first by fitting a tangent to the baseline, followed by calculation of the area between the tangent and the melting peak within the limits shown. The results of this give the enthalpy of the melting transition ( $\Delta H_m$ ) for each sample which are plotted in Figure 2.3 against their respective inverse number average molecular weights (i.e.  $1/M$ ). Some fractionated crystallization[37] was observed in a few of the samples examined (see Fig. 2.2(a)). The contribution of all crystal fractions, however, were included in the analysis. Also included in Figure 2.3, and in our calculations discussed below, are two values published by Pascui et al.[23] for P3HT samples that have two different molecular weights. It should be noted that their DSC data was not used by them to find  $\Delta H_m^\infty$  for P3HT.

Up to approximately 10,000 g/mol (defined as *Low M region* in Figure 2.3) there is a steady linear increase in the enthalpy of melting as  $M$  increases ( $1/M$  decreases).

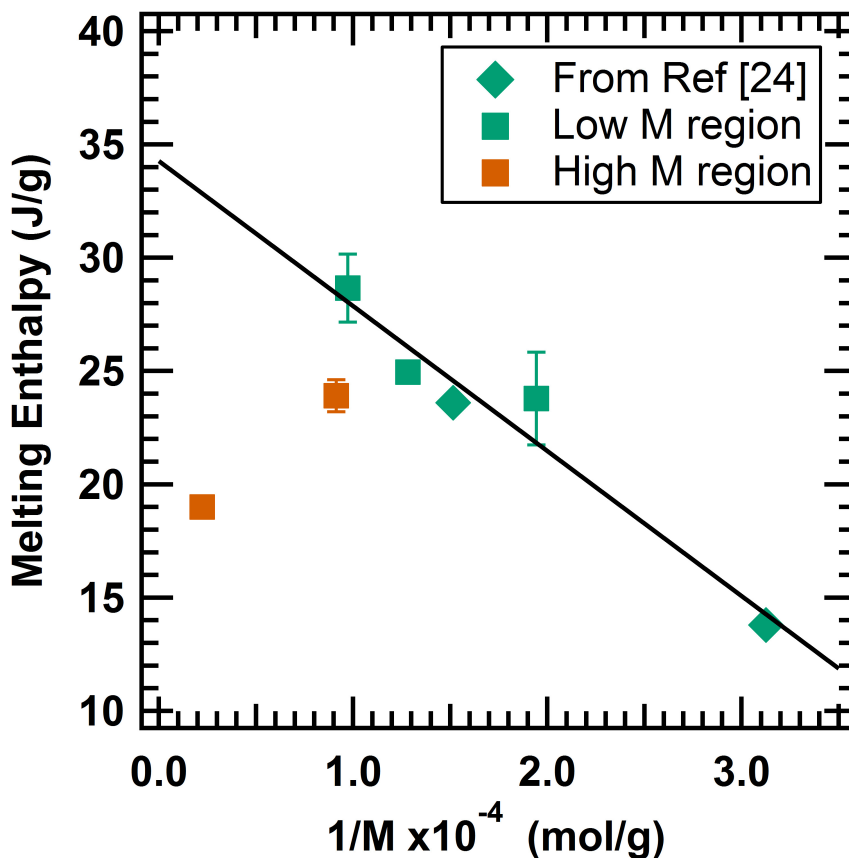


**Figure 2.3:** Graph of melting enthalpy vs.  $1/M$  for P3HT. Straight line drawn using *Low M region* and extrapolated to give the y-intercept ( $\Delta H_m^\infty$ ). The diamonds are from Ref. [23] and is included with the data gathered here.

Above 10,000 g/mol (*High M region*) though, there is a sharp decrease in the melting enthalpy, indicating a decrease in crystallinity. We attribute this decrease to the onset of chain folding of the P3HT molecules which was further investigated and will be discussed in the next section.

Therefore, to evaluate the heat of fusion of P3HT from the data in Figure 2.3 only the points in the Low M region were fitted to a straight line since only they possess the crystal type necessary for this calculation (extended chain crystals are required as explained in the next section). Fitting only the results of Pascui et al. yields  $\Delta H_m^\infty = 32.8$  J/g which differs from their reported value. Fitting only our results gives  $\Delta H_m^\infty = 32.1$  J/g. Combining both data sets and employing a linear fit, we obtain an average

for highly regioregular ( $> 97\%$ ) P3HT of  $\Delta H_m^\infty = 34.3 \pm 1.7$  J/g.

### 2.3.2 Onset of Chain Folding

The rapid drop in the melting enthalpy after a molecular weight of 10,000 g/mol can be explained by the change in crystallization tendency for all polymers with increasing molecular weight. For sufficiently low molecular weights, the P3HT chains adopt the extended chain conformation when crystallizing, i.e. they crystallize like a bunch of rigid rods, like pencils in a box. With an increase in molecular weight, the rods increase in length and edge effects (such as chain ends) play a smaller role and thus the energy required to melt the crystals increases; a principle similar to that of oligomeric polyethylene.[28, 29] Larger molecular weights mean longer, more flexible polymer chains that crystallize via the chain folded mechanism where parts of the polymer chain itself are excluded from the crystal. These excluded sections do not play a role in the crystallinity of the entire sample thus causing a reduction in the measured  $\Delta H_m$  as observed in this work. The onset of chain folding has been studied in-depth for polyethylene[38–41] and poly(ethylene oxide)[41, 42] and parallels between those materials and P3HT can be made.

Evidence of the onset of chain folding for P3HT can be obtained from TEM micrographs shown in Figure 2.4. First, it is observed that the samples self assemble into nanoscale fibrils that are well-defined and oriented. This organization transitions into a more random assembly of nanofibrils as the molecular weight increases. There is also an obvious increase in the dimension associated with the P3HT main chain length (c-axis or nanofibril width), going from DP31 to DP62 as can be observed from the difference in the width of the fibrils. However, the c-axis shrinks in the DP66 and CS samples, though it is not easily observed in the TEM micrograph. The width of the P3HT nanofibrils in each sample was therefore recorded through careful measurements of the micrographs. The average of these measurements along with the standard deviation is given in Table 2.2. These results are compared to theoretical

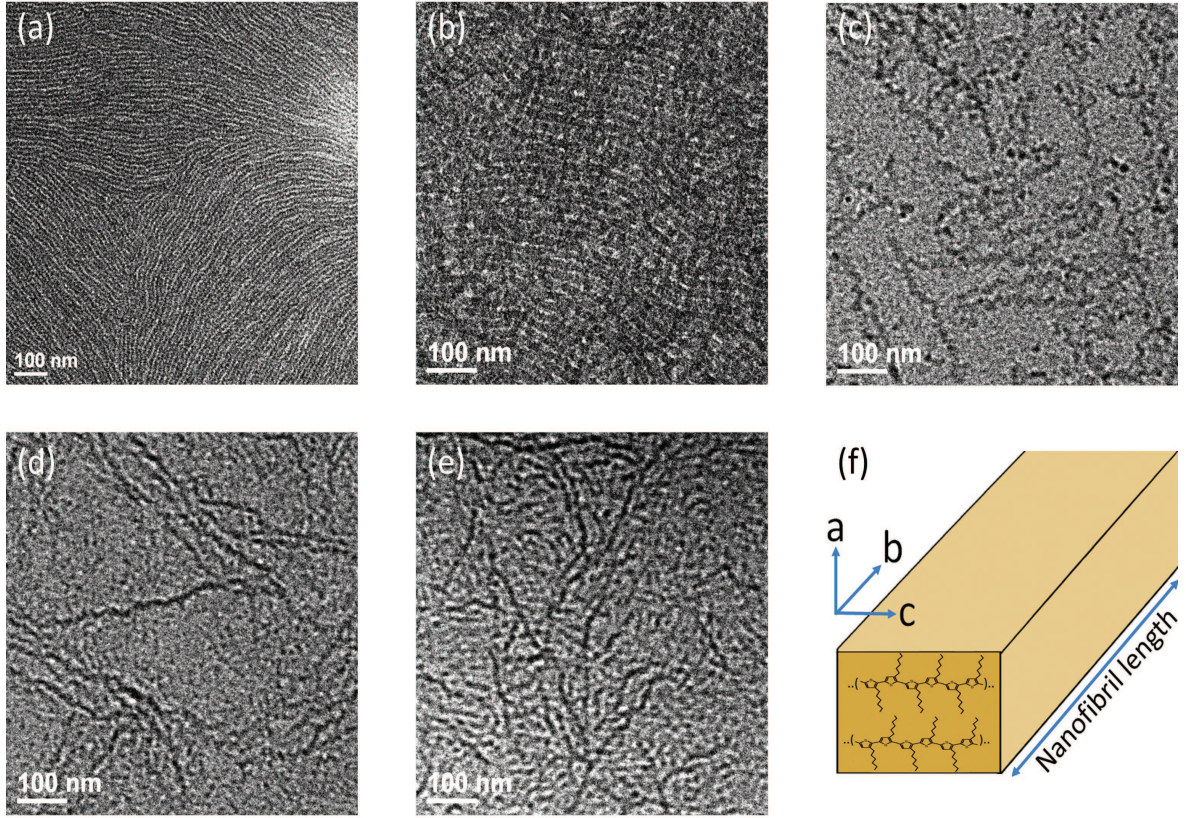


**Figure 2.4:** Shown are TEM micrographs of DP31 (a), DP47 (b), DP62 (c), DP66 (d) and CS (e) nanofibrils. Also shown is a schematic of the typical *edge-on* P3HT crystal orientation (f).

values for the contour length ( $R_{max}$ ) of an *equivalent freely jointed* polymer chain, calculated using the following equation[43]

$$R_{max} = Nb \quad (2.1)$$

where  $b$  is the Kuhn length of P3HT and  $N$  is the number of Kuhn segments. The persistence length of regioregular P3HT is reported as 2.4 nm (or 6 monomer units)[44] which corresponds to one half its Kuhn length. From the data in Table 2.2, there is good agreement between the measured and calculated values for DP31 through DP62. However, the nanofibril width of DP66 and CS deviate greatly from theoretical estimates and are both approximately 14 nm. The nanofibril width of P3HT has been previously measured and has shown to be closely related to the solvent used and the

sample preparation method.[45–47] While our results fall within the range of previous studies, our crystals were formed by the much less controlled means of solvent drop casting, which also explains the larger error in our measurements. The data in Table 2.2 however implies that a minimum of 62 monomer units (or  $\approx 5$  Kuhn segments) is required for the onset of chain folding crystallization for P3HT. The ability to fold results in an inevitable exclusion of part of the polymer chain from the crystal, thus proving the reduced overall crystallinity of DP66 and CS as can be implied from the data in Figure 2.3.

**Table 2.2:** Comparison of measured c-axes of each sample to theoretical values.

Sample	Nanofibril width (c axis) (nm)	
	Theoretical <sup>a</sup>	Measured
DP31	12.4	10.3 $\pm$ 1.3
DP47	18.8	15.6 $\pm$ 1.8
DP62	24.8	19.3 $\pm$ 2.3
DP66	26.4	13.9 $\pm$ 1.7
CS	108.4	14.1 $\pm$ 2.3

<sup>a</sup>Calculated from Eq. 2.1.

### 2.3.3 $\Delta H_m^\infty$ Modification

As can be observed from Table 2.2, the measured nanofibril widths fall short of their theoretical values. This shows that, even in the *Low M region*, the crystal does not contain the entire chain length (i.e. samples are not 100% crystalline). This may be an effect of the polydispersity or chain end exclusion. Thus the value of  $\Delta H_m^\infty$  stated earlier requires modification. A correction factor is therefore developed to adjust the values based on the amount of disorder present in each of the examined samples. From the grazing incidence small angle X-ray scattering (GISAXS) experiments performed on each sample (data not shown), a characteristic length scale called the long period can be measured. The long period corresponds to the average center to center distance from one high density (crystalline) phase to another which includes the low density (amorphous) phase between them. This was extracted from the GISAXS data via a

Porod analysis of the Bragg feature representing the long period, as was previously performed.[46, 48, 49] A crystalline volume fraction is then obtained and is plotted versus the degree of polymerization in Figure 2.5. Clearly, the samples containing extended chain crystals only follow a linear trend while the chain folded crystals of DP66 deviate from it as it does in the DSC data shown previously. Thus the linear fit to the data up to DP62 can be used as a mass fraction correction to the DSC data presented in Figure 2.3.

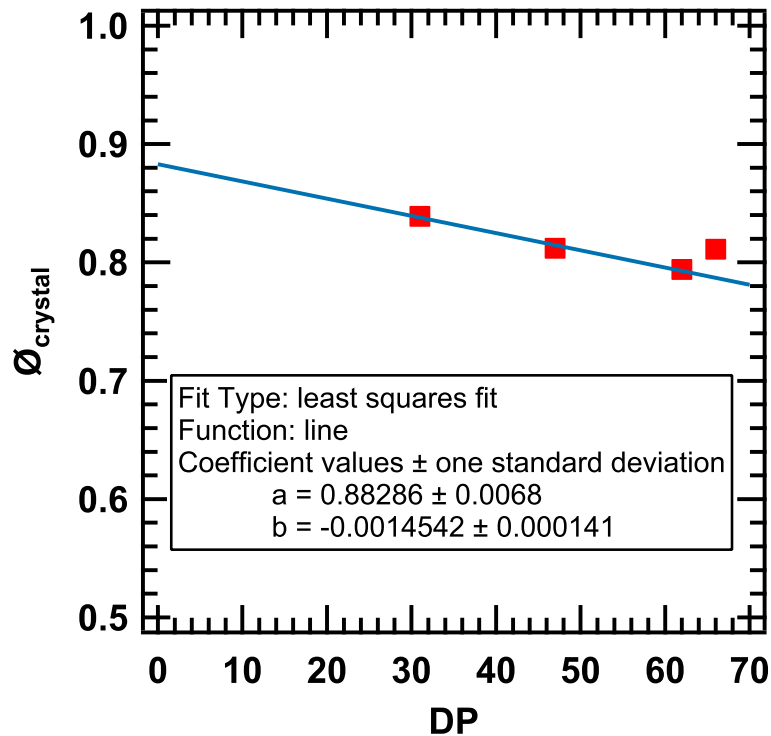


**Figure 2.5:** Plot of crystalline P3HT volume fraction ( $\Phi_{crystal}$ ) vs. degree of polymerization (DP) derived from the Porod analysis of GISAXS data (not shown). Linear region up to DP62 can be used as correction factor for the DSC melting enthalpy of the respective samples.

However, to employ this correction the polymer crystalline and amorphous densities must be known. Prosa et al.[50] calculated the P3HT crystalline density to be  $1.12 \text{ g/cm}^3$ . Lee and Dadmun[27] proposed two different values for amorphous P3HT obtained from He pycnometry. To confirm, a X-ray reflectivity study of a regiorandom

P3HT thin film was performed and the results are displayed in Figure 2.6 and Table 2.3. A value of  $1.09 \text{ g/cm}^3$  was obtained for regiorandom (fully amorphous) P3HT and is thus employed for this calculation.

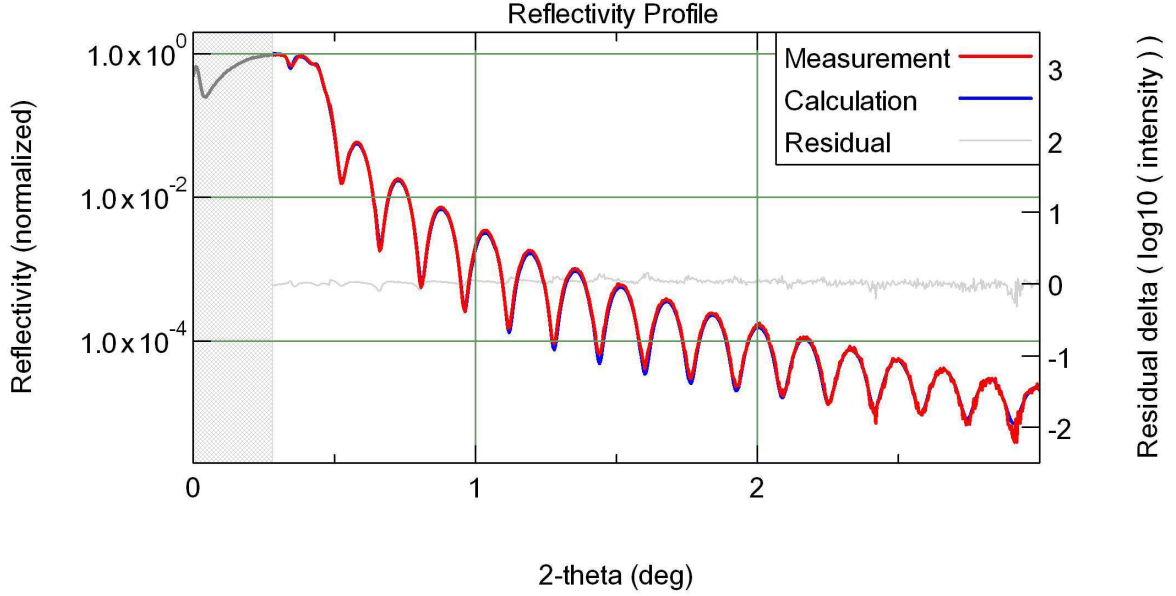


**Figure 2.6:** X-ray reflectivity of regiorandom P3HT on a Si substrate with a natural oxide layer showing the fit to the experimental data.

**Table 2.3:** Results of the X-ray reflectivity fitting procedure.

Material	Thickness (nm)	Density ( $\text{g/cm}^3$ )	Roughness (nm)
P3HT	53.45	1.09	0.66
SiO <sub>2</sub>	2.44	2.64	0.01
Si	N/A	2.33	3.55

By utilizing the correction factor on the data in the *Low M region* of Figure 2.3 (as shown in Figure 2.7), we arrive at a more accurate value of  $\Delta H_m^\infty = 42.9 \pm 2 \text{ J/g}$  for highly regioregular ( $> 97\%$ ) P3HT. It can be observed from Figure 2.7 that even without modification of the data,  $\Delta H_m^\infty$  is still  $\approx 80\%$  of the correct value.

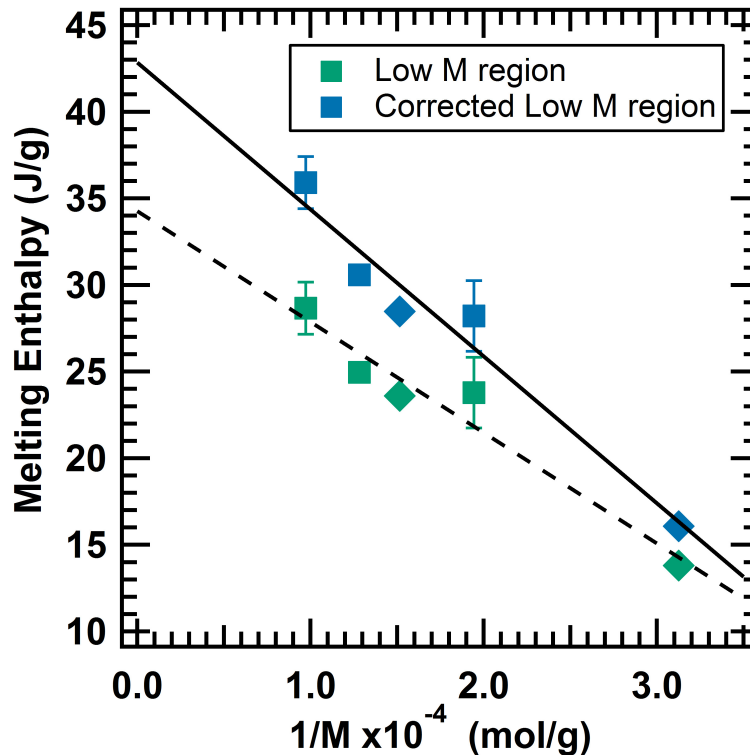


**Figure 2.7:** Graph of *Low M region* showing original and corrected values for the melting enthalpies and their corresponding linear fits.

## 2.4 Secondary Confirmation of Crystallinity

While calorimetry is a straightforward way to measure polymer crystallinity, there are other methods. An alternate route is to utilize the densities of the 100% amorphous ( $\rho_a$ ) and 100% crystalline ( $\rho_c$ ) polymer via the equation:

$$x_c = \frac{\rho_c(\rho_s - \rho_a)}{\rho_s(\rho_c - \rho_a)} \quad (2.2)$$

where  $x_c$  is the crystalline mass fraction and  $\rho_s$  is the sample density. As mentioned in the Introduction, Lee and Dadmun[27] used a variant of this approach to narrow the range of possibilities for  $\Delta H_m^\infty$ , in which the value obtained here firmly lies.

An independent study was therefore performed where the density of a highly crystalline sample was measured using helium pycnometry (AccuPyc 1330 pycnometer).

This sample was crystallized in solution under shear and its characterization revealed the creation of long, single crystal nanofibers.[51] Thus the assumption is made that this material should represent the highest practical density for P3HT and its value can be used as  $\rho_c$  in Equation 2.2. A regiorandom sample and CS were also measured to represent  $\rho_a$  and  $\rho_s$  respectively. The results are graphically displayed in Figure 2.8.

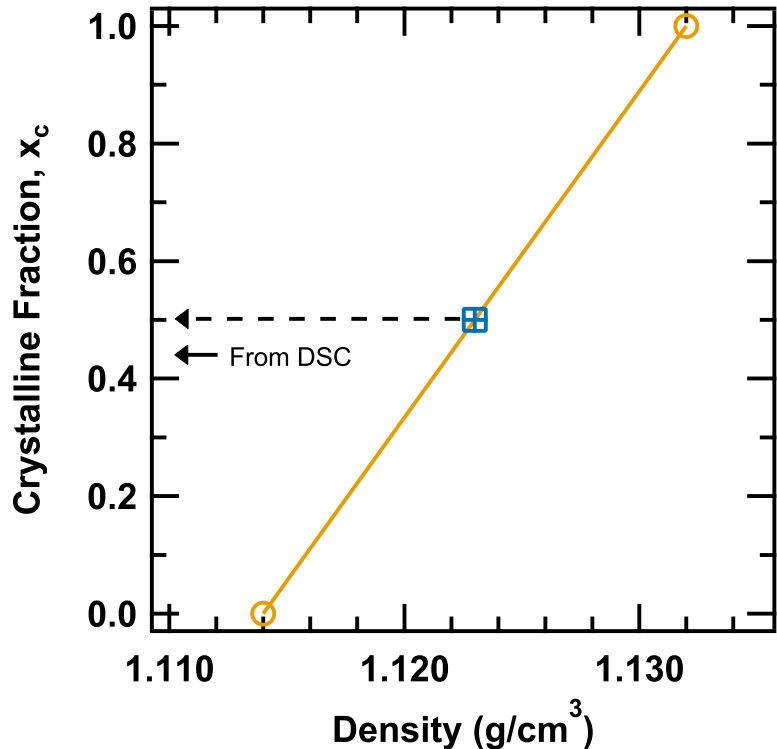


**Figure 2.8:** Graph of P3HT density vs. crystalline fraction. Orange circles and line depict the linear relationship between the fully amorphous ( $\rho_a$ ) and fully crystalline ( $\rho_c$ ) P3HT. Blue square shows that the crystalline fraction in CS from density measurements follows this relationship while the DSC analysis gives a slightly lower result.

Comparing the crystallinity of CS measured by both density and DSC methods described here, it is immediately observed that pycnometry obtained a higher crystallinity (50%) than DSC (44%) and comments about this result should be made.

Mandelkern et al. described,[52, 53] while investigating polyethylene and copolymers thereof, that evaluating polymer crystallinity via pycnometry regularly resulted

in higher values than those from DSC analysis. It was explained that the measured melting enthalpy of the crystal is negatively skewed by interfacial enthalpy of the crystallites, unlike its density. This interfacial enthalpy is the result of a transition region consisting of disordered chains exiting the crystal face and chains connecting neighboring crystallites that forms between the crystal and the surrounding glassy region; a topic that will be investigated further in the next chapter. Furthermore, large crystals and those formed by solution crystallization seem to not have this discrepancy.[52] The latter point gives credence to the assignment of  $\rho_c$  to the density of the shear solution crystallized P3HT.

Another observation is the difference in the measured density of regiorandom P3HT ( $\rho_a$ ) by X-ray reflectivity and pycnometry. The literature has attributed this phenomenon to a local, short range ordering effect persisting in regiorandom P3HT, possibly due to  $\pi$ - $\pi$  interactions[27, 54] or side chain dynamics.[55, 56] In this case, even differences in polymer thin film versus bulk properties may play a role.[57] Until a clear understanding of these effects is acquired, it is best to compare values obtained by the same experimental method. Thus  $\rho_a = 1.114 \text{ g/cm}^3$  was used in Figure 2.8.

Acknowledging the experimental differences and less understood complications with amorphous P3HT, the value of  $x_c$  for sample CS measured by both calorimetry and pycnometry are in agreement. Hence the accuracy of calculations performed on the calorimetric data gathered and the resulting value of  $\Delta H_m^\infty$  is confirmed.

## 2.5 Equilibrium Melting and Entropy

Other properties of P3HT revealed this experiment are the equilibrium melting temperature ( $T_m^\infty$ ) and the entropy of fusion ( $\Delta S_m^\infty$ ) via the same linear extrapolation process. Values of melting temperature ( $T_m$ ) were measured from the DSC thermograms shown in Figure 2.2. As described earlier, only the *Low M region* is relevant for examination. The  $T_m$  data shown in Figure 2.9 was measured at the end of the melting endotherm where the crystals are large and have Gibbs free energy similar to that of

the supercooled liquid at that temperature as was defined by Hoffman and Weeks.[58] Figure 2.9 also shows  $\Delta S_m$  which is given by  $\Delta H_m/T_m$ .

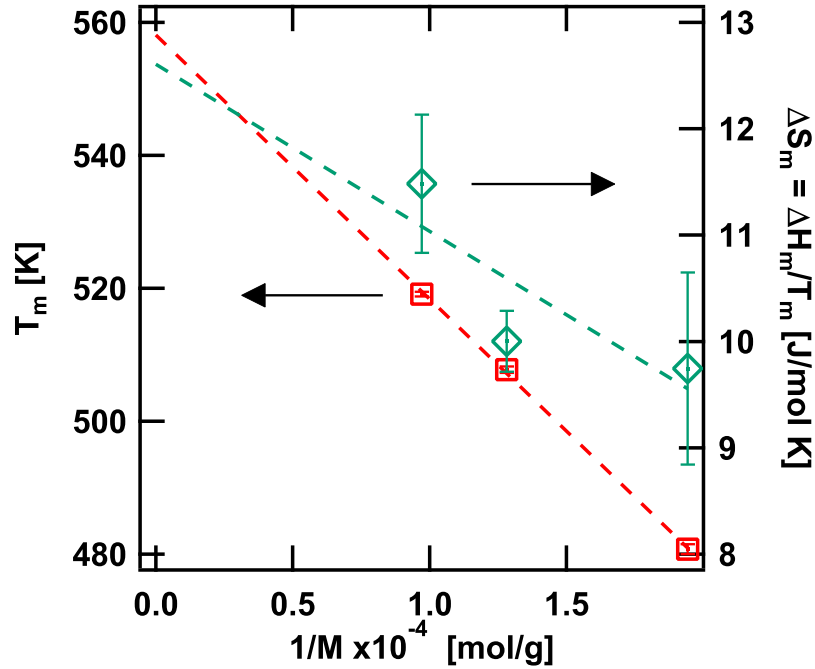


**Figure 2.9:** Graph of  $T_m^\infty$  and  $\Delta S_m^\infty$  versus inverse molecular weight of the *Low M* region. Dashed lines are linear fits to each dataset. Points shown correspond to the average value  $\pm$  one standard deviation.

Both datasets were fitted to a linear trend and the y-intercepts yielded  $285 \pm 1.5$  °C ( $558 \pm 1.5$  K) and  $12.6 \pm 1.5$  J/mol·K for  $T_m^\infty$  and  $\Delta S_m^\infty$  respectively. Gopalan and Mandelkern showed that (with the exception of more stringent experimental parameters than those employed herein) using low molecular weight polymers to extrapolate to  $T_m^\infty$  will result in higher than predicted values.[59] Our value therefore may represent the upper limit for  $T_m^\infty$  and a more careful study with higher molecular weights is likely to provide more accurate results. A recent report by Snyder et al.,[60] where the initial results of Koch et al.[26] were extended to higher molecular weights, found a lower value of  $T_m^\infty$  (272 °C) despite also reporting a larger value of  $\Delta H_m^\infty$  (49 J/g) in the same publication. Due to this, their value of  $\Delta S_m^\infty$  is in close proximity to ours.[61]

## 2.6 Conclusion

We conclude by noting the correct value of  $\Delta H_m^\infty$  must be known to find the crystallinity of P3HT or any of its composites in a quantitative manner. Also, from this study we understand that the onset of chain folding for P3HT occurs at approximately 62 monomer units or 5 Kuhn segments in length ( $19.3 \pm 2.3 \text{ nm}$ ) under normal conditions. The chain folded nanofibrillar structure has a width of 14 nm under the conditions of this experiment. Utilizing data from GISAXS studies, a correction factor was applied to the DSC results yielding a  $\approx 20\%$  increase in  $\Delta H_m^\infty$  to  $42.9 \pm 2 \text{ J/g}$ . Independent polymer density analysis confirms this value. Conveniently,  $T_m^\infty$  and  $\Delta S_m^\infty$  can also be calculated with this technique and  $T_m^\infty$  was recently used to find the surface energy of single crystal P3HT fibers.[51] Future studies will include application of the correct  $\Delta H_m^\infty$  to quantify the percent crystallinity within P3HT thin films. Knowledge of these quantities will advance understanding of the role degree of crystallinity has for semiconducting polymers with the structure/property relationships of devices fabricated from them.

## BIBLIOGRAPHY

- [1] JF Chang, B Sun, and DW Breiby. Enhanced mobility of poly (3-hexylthiophene) transistors by spin-coating from high-boiling-point solvents. *Chem. Mater.*, 16(23):4772–4776, 2004.
- [2] V. D. Mihailetschi, H. X. Xie, B. de Boer, L. J. A. Koster, and P. W. M. Blom. Charge Transport and Photocurrent Generation in Poly(3-hexylthiophene): Methanofullerene Bulk-Heterojunction Solar Cells. *Adv. Funct. Mater.*, 16(5):699–708, mar 2006.
- [3] A Assadi, C Svensson, M Wiilander, and O Inganäs. Field-effect mobility of poly (3-hexylthiophene). *Appl. Phys. Lett.*, 53(195), 1988.
- [4] H. Sirringhaus, P. J. Brown, R. H. Friend, M. M. Nielsen, K. Bechgaard, B. M. W. Langeveld-Voss, A. J. H. Spiering, R. A. J. Janssen, E. W. Meijer, P. Herwig, and D. M. de Leeuw. Two-dimensional charge transport in self-organized, high-mobility conjugated polymers. *Nature*, 401(6754):685–688, oct 1999.
- [5] APL Böttiger, Mikkel Jørgensen, A Menzel, Frederik C. Krebs, and JW Andreasen. High-throughput roll-to-roll X-ray characterization of polymer solar cell active layers. *J. Mater. Chem.*, 22:22501–22509, 2012.
- [6] Jon E. Carlé, Thomas R. Andersen, Martin Helgesen, Eva Bundgaard, Mikkel Jørgensen, and Frederik C. Krebs. A laboratory scale approach to polymer solar cells using one coating/printing machine, flexible substrates, no ITO, no vacuum and no spincoating. *Sol. Energy Mater. Sol. Cells*, 108:126–128, jan 2013.
- [7] Gianpaolo Susanna, Luigi Salamandra, Thomas M. Brown, Aldo Di Carlo, Francesca Brunetti, and Andrea Reale. Airbrush spray-coating of polymer bulk-heterojunction solar cells. *Sol. Energy Mater. Sol. Cells*, 95(7):1775–1778, jul 2011.

- [8] Claudio Girotto, Davide Moia, Barry P. Rand, and Paul Heremans. High-Performance Organic Solar Cells with Spray-Coated Hole-Transport and Active Layers. *Adv. Funct. Mater.*, 21(1):64–72, jan 2011.
- [9] Jonathan W. Kiel, Brian J. Kirby, Charles F. Majkrzak, Brian B. Maranville, and Michael E. Mackay. Nanoparticle concentration profile in polymer-based solar cells. *Soft Matter*, 6(3):641–646, 2010.
- [10] J W Kiel, M E Mackay, B J Kirby, B B Maranville, and C F Majkrzak. Phase-sensitive neutron reflectometry measurements applied in the study of photovoltaic films. *J. Chem. Phys.*, 133(7):074902, aug 2010.
- [11] Jonathon Kiel, Aaron Eberle, and Michael Mackay. Nanoparticle Agglomeration in Polymer-Based Solar Cells. *Phys. Rev. Lett.*, 105(16):1–4, oct 2010.
- [12] Andrew J Parnell, Alan D F Dunbar, Andrew J Pearson, Paul A Staniec, Andrew J C Dennison, Hiroshi Hamamatsu, Maximilian W A Skoda, David G Lidzey, and Richard A L Jones. Depletion of PCBM at the cathode interface in P3HT/PCBM thin films as quantified via neutron reflectivity measurements. *Adv. Mater.*, 22(22):2444–7, jun 2010.
- [13] Wen Yin and Mark Dadmun. A New Model for the Morphology of P3HT/PCBM Organic Photovoltaics from Small Angle Neutron Scattering: Rivers and Streams. *ACS Nano*, 5(6):4756–4768, 2011.
- [14] Dian Chen, Atsuhiko Nakahara, Dongguang Wei, Dennis Nordlund, and Thomas P Russell. P3HT/PCBM bulk heterojunction organic photovoltaics: correlating efficiency and morphology. *Nano Lett.*, 11(2):561–7, feb 2011.
- [15] BW Guralnick, BJ Kirby, C F Majkrzak, and M E Mackay. Morphological characterization of plastic solar cells using polarized neutron reflectivity. *Appl. Phys. Lett.*, 102:083305, 2013.

- [16] Neil D. Treat, Michael A. Brady, Gordon Smith, Michael F. Toney, Edward J. Kramer, Craig J. Hawker, and Michael L. Chabinyc. Interdiffusion of PCBM and P3HT Reveals Miscibility in a Photovoltaically Active Blend. *Adv. Energy Mater.*, 1(1):82–89, jan 2011.
- [17] Tiziano Agostinelli, Samuele Lilliu, John G. Labram, Mariano Campoy-Quiles, Mark Hampton, Ellis Pires, Jonathan Rawle, Oier Bikondoa, Donal D. C. Bradley, Thomas D. Anthopoulos, Jenny Nelson, and J. Emyr Macdonald. Real-Time Investigation of Crystallization and Phase-Segregation Dynamics in P3HT:PCBM Solar Cells During Thermal Annealing. *Adv. Funct. Mater.*, 21(9):1701–1708, may 2011.
- [18] Monamie Sanyal, Benjamin Schmidt-Hansberg, Michael F.G. Klein, Carmen Munuera, Alexei Vorobiev, Alexander Colsmann, Philip Scharfer, Uli Lemmer, Wilhelm Schabel, Helmut Dosch, and Esther Barrena. Effect of Photovoltaic Polymer/Fullerene Blend Composition Ratio on Microstructure Evolution during Film Solidification Investigated in Real Time by X-ray Diffraction. *Macromolecules*, 44(10):3795–3800, may 2011.
- [19] Jens Balko, Ruth H. Lohwasser, Michael Sommer, Mukundan Thelakkat, and Thomas Thurn-Albrecht. Determination of the Crystallinity of Semicrystalline Poly(3-hexylthiophene) by Means of Wide-Angle X-ray Scattering. *Macromolecules*, 46:9642–9651, dec 2013.
- [20] Jung Ah Lim, Feng Liu, Sunzida Ferdous, Murugappan Muthukumar, and Alejandro L. Briseno. Polymer semiconductor crystals. *Mater. Today*, 13(5):14–24, may 2010.
- [21] Khosrow Rahimi, Ioan Botiz, Natalie Stingelin, Navaphun Kayunkid, Michael Sommer, Felix Peter Vinzenz Koch, Ha Nguyen, Olivier Coulembier, Philippe

- Dubois, Martin Brinkmann, and Günter Reiter. Controllable processes for generating large single crystals of poly(3-hexylthiophene). *Angew. Chemie Int. Ed.*, 51(44):11131–5, oct 2012.
- [22] Sudip Malik and Arun K. Nandi. Crystallization mechanism of regioregular poly(3-alkyl thiophene)s. *J. Polym. Sci. Part B Polym. Phys.*, 40(18):2073–2085, sep 2002.
- [23] Ovidiu F. Pascui, Ruth Lohwasser, Michael Sommer, Mukundan Thelakkat, Thomas Thurn-Albrecht, and Kay Saalwachter. High Crystallinity and Nature of Crystal–Crystal Phase Transformations in Regioregular Poly(3-hexylthiophene). *Macromolecules*, 43(22):9401–9410, nov 2010.
- [24] Chad R. Snyder, Jessica S. Henry, and Dean M. DeLongchamp. Effect of Regioregularity on the Semicrystalline Structure of Poly(3-hexylthiophene). *Macromolecules*, 44:7088–7091, aug 2011.
- [25] Felix P V Koch, Paul Smith, and Martin Heeney. "Fibonacci's route" to regioregular oligo(3-hexylthiophene)s. *J. Am. Chem. Soc.*, 135(37):13695–8, sep 2013.
- [26] Felix Peter Vinzenz Koch, Martin Heeney, and Paul Smith. Thermal and structural characteristics of oligo(3-hexylthiophene)s (3HT)<sub>n</sub>, n = 4-36. *J. Am. Chem. Soc.*, 135(37):13699–709, sep 2013.
- [27] Cameron S. Lee and Mark D. Dadmun. Important thermodynamic characteristics of poly(3-hexyl thiophene). *Polymer*, 55(1):4–7, jan 2014.
- [28] Malcolm Dole, W. P. Hettlinger, N. R. Larson, and J. A. Wethington. Specific Heat of Synthetic High Polymers. I. A Study of Polyethylene Including a Statistical Theory of Crystallite Length. *J. Chem. Phys.*, 20(5):781, dec 1952.
- [29] Fred W. Billmeyer. Lattice Energy of Crystalline Polyethylene. *J. Appl. Phys.*, 28(10):1114, 1957.

- [30] Robert S. Loewe, Sonya M. Khersonsky, and Richard D. McCullough. A Simple Method to Prepare Head-to-Tail Coupled, Regioregular Poly(3-alkylthiophenes) Using Grignard Metathesis. *Adv. Mater.*, 11(3):250–253, mar 1999.
- [31] Robert S. Loewe, Paul C. Ewbank, Jinsong Liu, Lei Zhai, and Richard D. McCullough. Regioregular, Head-to-Tail Coupled Poly(3-alkylthiophenes) Made Easy by the GRIM Method: Investigation of the Reaction and the Origin of Regioselectivity. *Macromolecules*, 34(13):4324–4333, jun 2001.
- [32] Richard D. McCullough, Renae D. Lowe, Manikandan Jayaraman, and Deborah L. Anderson. Design, synthesis, and control of conducting polymer architectures: structurally homogeneous poly(3-alkylthiophenes). *J. Org. Chem.*, 58(4):904–912, feb 1993.
- [33] Richard D. McCullough and Renae D. Lowe. Enhanced electrical conductivity in regioselectively synthesized poly(3-alkylthiophenes). *J. Chem. Soc. Chem. Commun.*, (1):70, jan 1992.
- [34] Richard D. McCullough. The Chemistry of Conducting Polythiophenes. *Adv. Mater.*, 10(2):93–116, jan 1998.
- [35] Bernhard Wunderlich. *Thermal Analysis of Polymeric Materials*. Springer, New York, 2005.
- [36] Mike Reading and Douglas J Hourston, editors. *Modulated Temperature Differential Scanning Calorimetry: Theoretical and Practical Applications in Polymer Characterisation*. Springer, 2006.
- [37] P. Kohn, S. Huettner, U. Steiner, and M. Sommer. Fractionated Crystallization of Defect-Free Poly(3-hexylthiophene). *ACS Macro Lett.*, 1(10):1170–1175, oct 2012.
- [38] G Ungar, J Stejny, A Keller, I Bidd, and M C Whiting. The crystallization of ultralong normal paraffins: the onset of chain folding. *Science*, 229(4711):386–9, jul 1985.

- [39] S. J. Organ and A. Keller. The onset of chain folding in ultralong n-alkanes: An electron microscopic study of solution-grown crystals. *J. Polym. Sci. Part B Polym. Phys.*, 25(12):2409–2430, dec 1987.
- [40] John D Hoffman. Transition from extended-chain to once-folded behaviour in pure n-paraffins crystallized from the melt. *Polymer*, 32(15):2828–2841, 1991.
- [41] Paul G. Higgs and Goran Ungar. The growth of polymer crystals at the transition from extended chains to folded chains. *J. Chem. Phys.*, 100(1):640, jan 1994.
- [42] John D. Hoffman. Onset of chain folding in low-molecular-weight poly(ethylene oxide) fractions crystallized from the melt. *Macromolecules*, 19(4):1124–1128, jul 1986.
- [43] Michael Rubenstein and Ralph H Colby. *Polymer Physics*. Oxford University Press, 2003.
- [44] GW Heffner and DS Pearson. Molecular characterization of poly (3-hexylthiophene). *Macromolecules*, 24(23):6295–6299, 1991.
- [45] Kyo Jin Ihn, Jeff Moulton, and Paul Smith. Whiskers of poly(3-alkylthiophene)s. *J. Polym. Sci. Part B Polym. Phys.*, 31(6):735–742, may 1993.
- [46] Rui Zhang, Bo Li, Mihaela C Iovu, Malika Jeffries-El, Geneviève Sauv e, Jessica Cooper, Shijun Jia, Stephanie Tristram-Nagle, Detlef M Smilgies, David N Lambeth, Richard D McCullough, and Tomasz Kowalewski. Nanostructure Dependence of Field-Effect Mobility in Regioregular Poly (3-hexylthiophene) Thin Film Field Effect Transistors. *J. Am. Chem. Soc.*, 128(11):3480–3481, 2006.
- [47] J Liu, M Arif, J Zou, SI Khondaker, and L Zhai. Controlling poly (3-hexylthiophene) crystal dimension: nanowhiskers and nanoribbons. *Macromolecules*, 42:9390–9393, 2009.

- [48] G. Porod. Die Röntgenkleinwinkelstreuung von dichtgepackten kolloiden Systemen. *Kolloid-Zeitschrift*, 124(2):83–114, nov 1951.
- [49] Junying Liu, Dahlia Haynes, Courtney Balliet, Rui Zhang, Tomasz Kowalewski, and Richard D. McCullough. Self Encapsulated Poly(3-hexylthiophene)-poly(fluorinated alkyl methacrylate) Rod-Coil Block Copolymers with High Field Effect Mobilities on Bare SiO<sub>2</sub>. *Adv. Funct. Mater.*, 22(5):1024–1032, mar 2012.
- [50] T. J. Prosa, M. J. Winokur, Jeff Moulton, Paul Smith, and A. J. Heeger. X-ray structural studies of poly(3-alkylthiophenes): an example of an inverse comb. *Macromolecules*, 25(17):4364–4372, aug 1992.
- [51] Ngoc A. Nguyen. *Flow Induced/ Refined Solution Crystallization of a Semiconducting Polymer*. PhD thesis, University of Delaware, 2016.
- [52] Leo Mandelkern, A. L. Allou, and M. R. Gopalan. Enthalpy of fusion of linear polyethylene. *J. Phys. Chem.*, 72(1):309–318, jan 1968.
- [53] Leo Mandelkern. The Relation between Structure and Properties of Crystalline Polymers. *Polym. J.*, 17(1):337–350, jan 1985.
- [54] Xiaobo Shen, Weiguo Hu, and Thomas P. Russell. Measuring the Degree of Crystallinity in Semicrystalline Regioregular Poly(3-hexylthiophene). *Macromolecules*, 49(12):4501–4509, jun 2016.
- [55] Shireesh Pankaj, Elke Hempel, and Mario Beiner. Side-Chain Dynamics and Crystallization in a Series of Regiorandom Poly(3-alkylthiophenes). *Macromolecules*, 42(3):716–724, feb 2009.
- [56] Ryan C. Nieuwendaal, Chad R. Snyder, and Dean M. DeLongchamp. Measuring Order in Regioregular Poly(3-hexylthiophene) with Solid-State <sup>13</sup>C CPMAS NMR. *ACS Macro Lett.*, 3(2):130–135, feb 2014.

- [57] James A. Forrest and Johan Mattsson. Reductions of the glass transition temperature in thin polymer films: Probing the length scale of cooperative dynamics. *Phys. Rev. E*, 61(1):R53–R56, jan 2000.
- [58] John D. Hoffman and James J. Weeks. Melting process and the equilibrium melting temperature of polychlorotrifluoroethylene. *J. Res. Natl. Bur. Stand. Sect. A Phys. Chem.*, 66A(1):13–28, 1962.
- [59] M. R. Gopalan and Leo Mandelkern. Effect of crystallization temperature and molecular weight on the melting temperature of linear polyethylene. *J. Phys. Chem.*, 71(12):3833–3841, nov 1967.
- [60] Chad R. Snyder, Ryan C. Nieuwendaal, Dean M. DeLongchamp, Christine K. Luscombe, Prakash Sista, and Shane D. Boyd. Quantifying Crystallinity in High Molar Mass Poly(3-hexylthiophene). *Macromolecules*, 47(12):3942–3950, jun 2014.
- [61] Chad R. Snyder, R. Joseph Kline, Dean M. DeLongchamp, Ryan C. Nieuwendaal, Lee J. Richter, Martin Heeney, and Iain McCulloch. Classification of semiconducting polymeric mesophases to optimize device postprocessing. *J. Polym. Sci. Part B Polym. Phys.*, pages n/a–n/a, aug 2015.

## Chapter 3

### QUANTIFYING THE RIGID AMORPHOUS FRACTION IN POLY(3-HEXYLTHIOPHENE)

Adapted with permission from Remy, R.; Wei, S.; Campos, L. M.; Mackay, M. E. *ACS Macro Lett.* 2015, 4, 1051–1055. Copyright 2015 American Chemical Society.

#### 3.1 Introduction

Semiconducting polymers have shown great utility in applications such as field effect transistors, light emitting diodes and solar cells. Poly(alkylthiophene)s, especially poly(3-hexylthiophene) (P3HT), are the most widely investigated polymers for these applications but the performance of these materials is highly dependent on their morphology. Regioregular P3HT (rrP3HT) is a semicrystalline polymer and it has been shown[1] that its crystallinity is important in determining its electrical properties which directly influences device performance; a classic materials science challenge to relate morphology to performance.

The most facile method of determining quantitative polymer crystallinity is via differential scanning calorimetry (DSC). All that is required is knowledge of the enthalpy of fusion of an infinitely large crystal ( $\Delta H_m^\infty$ ) for the polymer in question. For some time there has been conflict in the literature about this value for rrP3HT.[2–5] Recently though, we have determined  $\Delta H_m^\infty = 42.9$  J/g for rrP3HT using an approach derived from the literature on linear polyethylene,[6] that agrees well with the value given by Snyder et al.[7] Now it is possible to quantitatively determine the crystallinity of a P3HT specimen using DSC to address the above challenge.

While polymer crystallinity is important, it has also been shown that more attention should be directed to the disordered or amorphous component of these

materials.[8–15] It is well known that the hole mobility for rrP3HT, and other semiconducting polymers by extension, increases with molecular weight.[8–13] The reason is due to an increase in the number of entanglements so the material consists of crystallites that are interconnected by amorphous chain segments spanning them (also known as tie chains). This point was expounded upon further by Noriega et al. who discovered that the measured paracrystallinity (or degree of disorder) in these materials is correlated to their charge transport properties and that poorly ordered materials have a tolerance to charge traps within aggregates.[14] Utilizing cyclic voltammetry, UV-vis absorption and ultraviolet photoelectron spectroscopy, Sweetnam et al. observed valence band offsets between amorphous and crystalline portions of semiconducting polymers and blends containing a fullerene donor that act as a driving force for hole extraction from the mixed phase, thereby improving charge separation.[15] Due to the importance of morphological details to charge transport properties, we present a method that provides quantitative data representing the physical fractions of crystalline and amorphous material present in rrP3HT to deepen the understanding of the multi-phase morphology of semiconducting polymers.

From the polymer physics perspective, the amorphous polymer phase can be further divided into two fractions. The first fraction consists of the traditional amorphous chains where they are free to move according to the standard polymer kinetics models above the glass transition temperature ( $T_g$ ). This is called the mobile amorphous fraction (MAF). The second fraction consists of constrained, yet still disordered, chains called the rigid amorphous fraction (RAF). These terms were first coined by Wunderlich and coworkers while investigating the glass transition of poly(oxyethylene).[16] RAF has since been discovered in many other semicrystalline polymers[17] and is thought to exist at crystal/amorphous interfaces as well as interfaces between polymers and fillers in composites.[18, 19] With regard to semiconducting polymers, there has been literature mentioning its existence, mainly in relation to anomalies or deviations in data sets, although the quantity present was not determined.[2, 20–24]

Temperature modulated DSC (TMDSC) has been previously proven effective at

elucidating the weak  $T_g$  of rrP3HT and has been used to construct phase diagrams of rrP3HT and fullerene mixtures.[25–27] Here, TMDSC is utilized to examine rrP3HT samples for the presence of all three polymer phases defined above. First we describe the TMDSC criteria for accurate data collection which allows for a comprehensive analysis in one experiment. The step change in heat capacity at  $T_g$  ( $\Delta C_{p,amor}$ ) for fully amorphous regiorandom P3HT (ranP3HT) is then evaluated for use in determining the RAF. By focusing on the  $T_g$  of rrP3HT, analysis can be performed to properly elucidate its nature as a three step transition which involves the devitrification of different parts of the polymer chain in sequence. Thus, the first calculation of rrP3HT MAF and RAF in the literature to date is accomplished. Finally, this study is extended to thin films of both ranP3HT and rrP3HT to reveal and explain deviations from bulk behavior due to processing.

### 3.2 Experimental

Experiments in this report were performed on rrP3HT purchased from Luminescence Technologies Corp ( $M_w \sim 45$  kg/mol, PDI  $> 2$ , regioregularity  $>95\%$ ) and were used without further purification. ranP3HT also employed here was synthesized according to the literature[28] ( $M_n = 21.6$  kg/mol, PDI = 2.0 and 56% H-T coupling determined by NMR). DSC measurements were done at  $10^\circ\text{C}/\text{min}$  and TMDSC measurement parameters are displayed in the respective figures below. For bulk analysis, rrP3HT specimens were first crystallized from the melt at  $10^\circ\text{C}/\text{min}$  to impart identical thermal histories while ranP3HT samples were quenched from  $300^\circ\text{C}$  to preserve its amorphous nature.

Thin films of both ranP3HT and rrP3HT were fabricated via spin coating from 30mg/mL chlorobenzene solutions that were prepared by stirring overnight at room temperature. Glass substrates were prepared by cleaning with soapy water, acetone then isopropyl alcohol, followed by UV ozone treatment for 30 minutes. The substrates were then coated with a 40nm layer of PEDOT:PSS and placed in an oven for 15 minutes. They were then cooled and transferred to a  $\text{N}_2$  glovebox where the P3HT

solutions were spun coat at 600rpm for 60 seconds to produce  $\approx 220$  nm thick, uniform films. The P3HT films were finally released from the substrates by slow immersion into deionized water that dissolved the underlying PEDOT:PSS layer leaving the P3HT layer to be collected, dried (under vacuum and room temperature for 48 hours) and tested. The thin films are subjected to two TMDSC heating scans to 300 °C separated by a quench, in the case of ranP3HT, or a 10 °C/min cooling scan for rrP3HT.

### 3.3 Results and Discussion

#### 3.3.1 MDSC Technique and Parameter Optimization

While typical DSC has only one parameter, the heating rate ( $b$  in °C/min), TMDSC has three; the heating rate ( $b$ ), the amplitude of modulation ( $B$  in °C) and the period of modulation ( $p$  in sec), each of which affects the data output according to the relation:

$$T(t) = T_0 + bt + B \sin\left(\frac{2\pi}{p}t\right) \quad (3.1)$$

where  $T(t)$  is the temperature at a given time  $t$  and  $T_0$  is the initial temperature. Full mathematical descriptions of TMDSC have been published elsewhere.[29, 30] Moreover, the method by which data is extracted involves a deconvolution procedure (in most cases a Fourier Transform) which requires *sufficient* oscillations within a given transition to produce a correct result with a satisfactorily small error. Therefore, to obtain the the most accurate information from TMDSC, the experimental parameters must be optimized.

To this end, we refer to the early work of Reading and coworkers.[31–33] They showed that TMDSC is virtually indistinguishable from conventional DSC of the same heating rate by overlaying the total heat flow from TMDSC and the heat flow from conventional DSC.[33] It was also illustrated that there is little loss of quantitative information with a change in experimental method. Figure 3.1 displays this overlay plot for rrP3HT with two different TMDSC parameter sets. The parameters for Figures 3.1a and b were obtained from recent literature,[24] while Figures 3.1c and d are

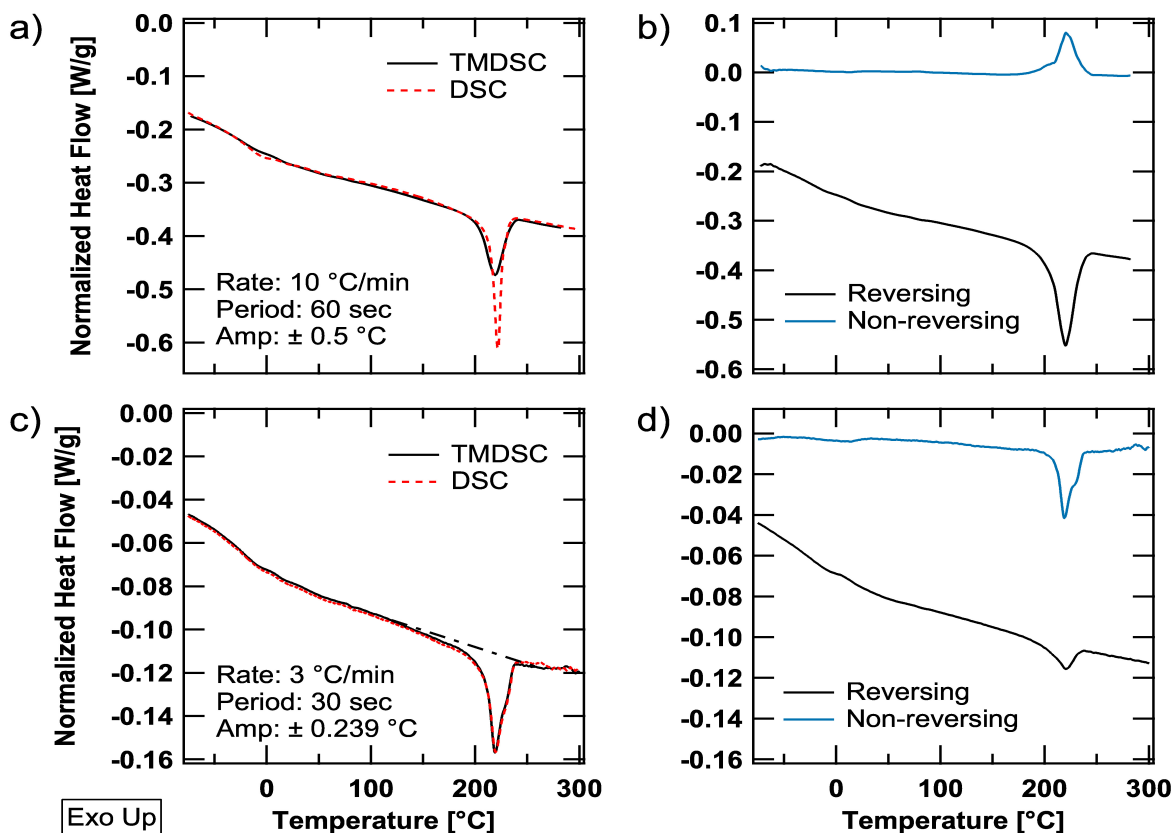


**Figure 3.1:** Deconvoluted data from two TMDSC experiments on rrP3HT. Total heat flow thermograms are shown in (a) and (c) with their experimental parameters. An overlay of their respective heat flow signals from a typical DSC experiment (red dashed lines) is also shown to illustrate the similarity in the resultant data of both methods. Black dot-dashed line in (c) defines the area used to calculate sample crystallinity. Reversing and non-reversing heat flow thermograms for (a) and (c) are displayed in (b) and (d), respectively.

the parameters employed in the present study. Clearly, the experimental conditions used to produce the data in Figure 3.1c are in agreement with the expected result.

A difference in the data is also observed in the reversing and non-reversing signals. In fact, another requirement mentioned by Reading and coworkers is the necessity for multiple temperature oscillations over a given transition, such as the melting point (achieved by lowering the heating rate and period of oscillation), which reduces the deconvolution error associated with the analysis.[31–33] While it could be said that

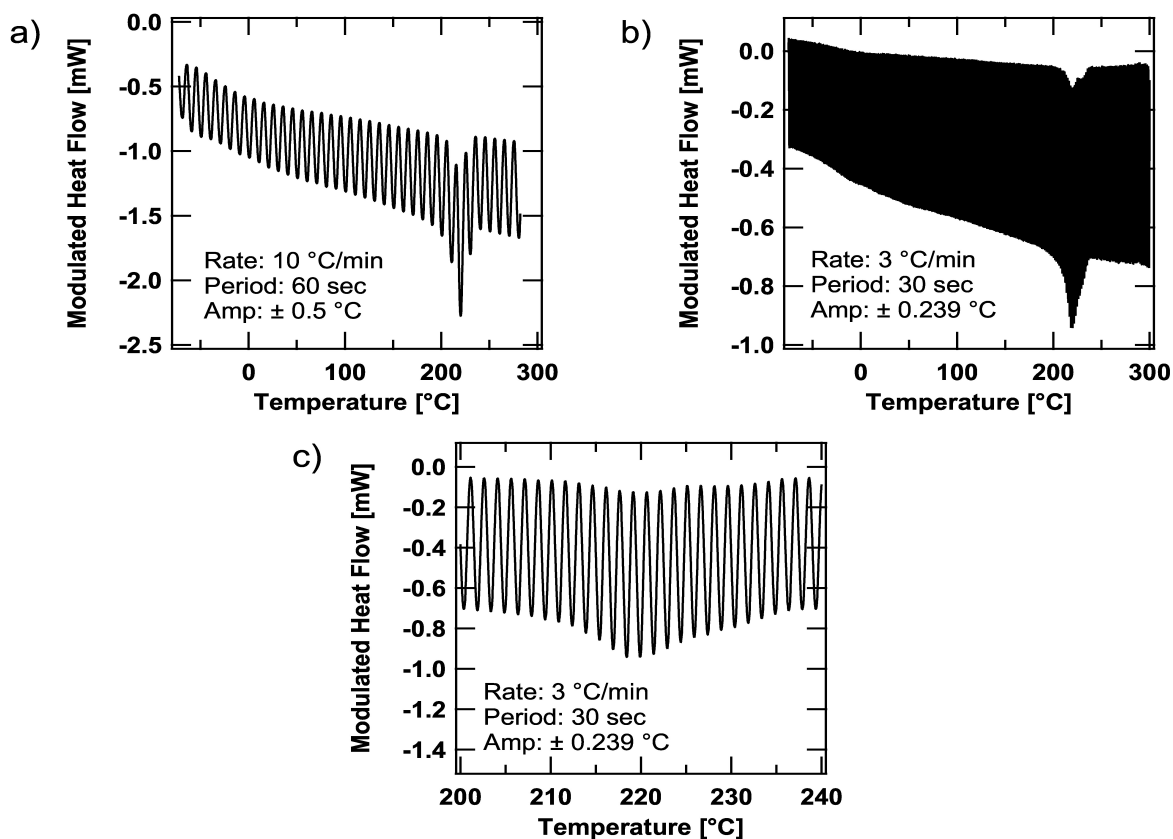


**Figure 3.2:** Raw TMDSC data from both experimental parameters. (a) Parameters taken from Ref. [24] and (b) parameters used in this study. (c) shows a magnified view of the melting transition in (b). It can be observed that the parameters used here more than double the oscillations across the melting transition resulting in more accurate deconvolution.

Figure 3.1b shows recrystallization and reorganization during melting, the incorrect parameters and low oscillation density across the melting transition render this description false. This is clearly depicted in Figure 3.2 where the density of oscillations achieved using the parameters in this study is higher than that taken from the previously published study.[24] Therefore the accuracy in our analysis is maximized.

Thus Figure 3.1d correctly shows the bulk of the melting process occurring in the non-reversing signal since melting should not follow the applied temperature oscillations. We contend, therefore, that care must be taken in the choice of TMDSC

experimental parameters and the results of Beckingham et al.[24] may require additional evidence to properly support their claim.

In addition to the stated TMDSC requirements, to obtain quantitative crystallinity measurements, the sample should not be allowed to cool (and therefore crystallize) during the experiment. Thus, the oscillation amplitude was reduced to where the instantaneous heating rate is never negative (i.e.  $dT(t)/dt \geq 0$ ). The technique utilizing this restriction is called *heat-only TMDSC* and is applied to all subsequent data shown in this work.

### 3.3.2 RAF Calculation for Bulk rrP3HT

The rigid amorphous fraction (RAF) is calculated according to the equation:[16, 17]

$$RAF = 1 - \frac{\Delta H_m}{\Delta H_m^\infty} - \frac{\Delta C_{p,sam}}{\Delta C_{p,amor}} \quad (3.2)$$

where  $\Delta H_m$  is the sample enthalpy of melting,  $\Delta H_m^\infty$  is the enthalpy of fusion of a perfect, infinite P3HT crystal,  $\Delta C_{p,sam}$  is the step change in heat capacity at  $T_g$  of the sample and  $\Delta C_{p,amor}$  is the step change in heat capacity at  $T_g$  of 100% amorphous P3HT. The second term in Figure 3.2 is the sample's crystallinity and the final term is its MAF. We have previously determined  $\Delta H_m^\infty$  for rrP3HT[6] and  $\Delta H_m$  is directly measured from the total heat flow data (or the sum of the reversing and non-reversing melting transitions, whichever is easier. See Figure 3.1). However, the final term (or MAF) of the expression has never been evaluated for P3HT.

While it is difficult to obtain 100% amorphous rrP3HT, ranP3HT is naturally amorphous and of identical chemical composition. Therefore,  $\Delta C_{p,amor}$  can be directly measured from the  $T_g$  of ranP3HT as depicted in Figure 3.3. From the derivative curve (Figure 3.3c) it is obvious that the  $T_g$  of ranP3HT is one single transition at 15°C and a value of  $\Delta C_{p,amor} = 0.32 \pm 0.02$  J/g°C is obtained. Wunderlich explained that the step change in heat capacity at the glass transition ( $\Delta C_{p,amor}$ ) of an amorphous polymer can be calculated by dividing the monomer unit into "mobile beads," each of which contributes approximately 11 J/mol°C.[34] These beads are related to the hole

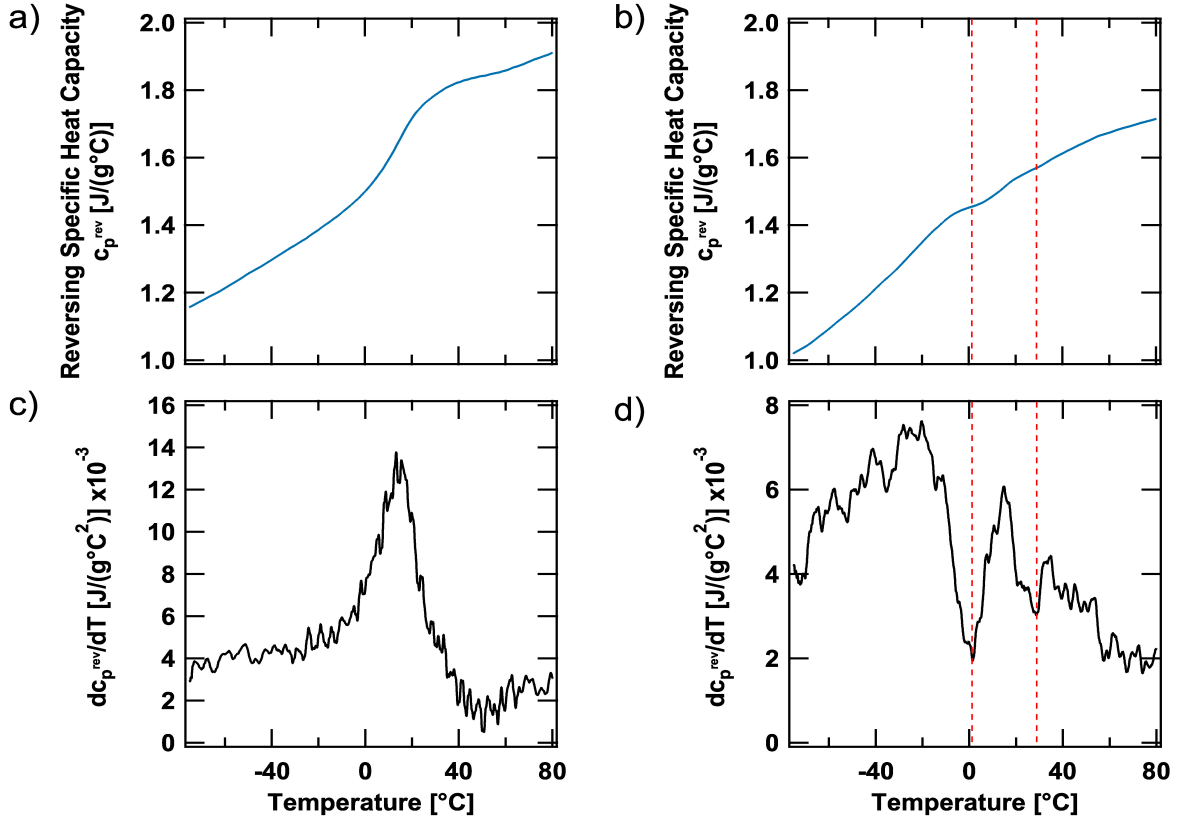


**Figure 3.3:** TMDSC thermograms showing  $c_p^{rev}$  of ranP3HT (a) and rrP3HT (b), along with their respective derivatives,  $dc_p^{rev}/dT$ , in (c) and (d). The red dashed lines in (b) and (d) identify the local minima in  $dc_p^{rev}/dT$  for rrP3HT used to assign regions I, II and III.

theory of liquids as described by Hirai et al.[35, 36] used to describe bulk viscosity and other thermodynamic quantities such as heat capacity, compressibility and thermal expansion. The theory describes them as the smallest molecular unit of a liquid (glass) that can affect the hole equilibrium in that liquid (glass). At  $T_g$ , the number of holes is assumed constant so the change in heat capacity of the material is related to the number of mobile beads interacting with the holes at that temperature.

Using P3HT monomer molecular weight (166.28 g/mol) to convert our result, we obtain 53.2 J/mol°C for  $\Delta C_{p,amor}$ . This means  $\approx 5$  beads contribute to the measured value. We propose P3HT is divided into these beads as shown in Figure 3.4 where the thiophene ring is one "large" bead that contributes the energy equivalent of two

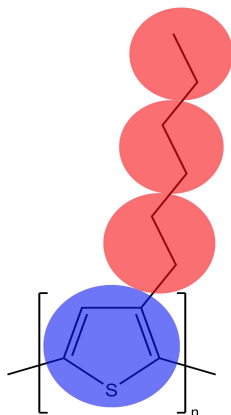


**Figure 3.4:** Illustration defining the proposed "mobile beads" that comprise a P3HT monomer unit. Blue represents the large bead that provides twice the energy as the small beads (red).

"small" beads, similar to the benzene ring in polystyrene, for example.[37] In contrast, the  $T_g$  and derivative curve of rrP3HT, shown in Figure 3.3b and d respectively, is more complicated.

First, there is a transition that culminates at approximately 0°C but extends to temperatures below the instrument's capabilities. Previous research has described that this is likely from configurational dynamics of the side chains[23] with an onset just before -75°C.[22] Interestingly, this is not noticeable in ranP3HT suggesting that it may originate from the side chains within the crystallites but confirmation of this is beyond the scope of this paper. Immediately afterwards, the  $T_g$  of the polymer occurs, so the measurement of  $\Delta C_{p,sam}$  for rrP3HT was first taken between 0°C and 65°C, where the derivative curve plateaus (see Figure 3.3c). It should be mentioned that no side chain melting was observed in this experiment as was seen for lower molecular weight rrP3HT[3, 38, 39] (see Figure 3.1d). With all of the necessary information, the resultant RAF for rrP3HT is  $\approx 2\%$ .

Yet, this value is uncharacteristically low for a polymer with such high crystallinity (see Table 3.1). Reconsidering the derivative curve for rrP3HT reveals the  $T_g$  as a two step transition evidenced by the minimum in the derivative at  $\approx 30^\circ\text{C}$  (see

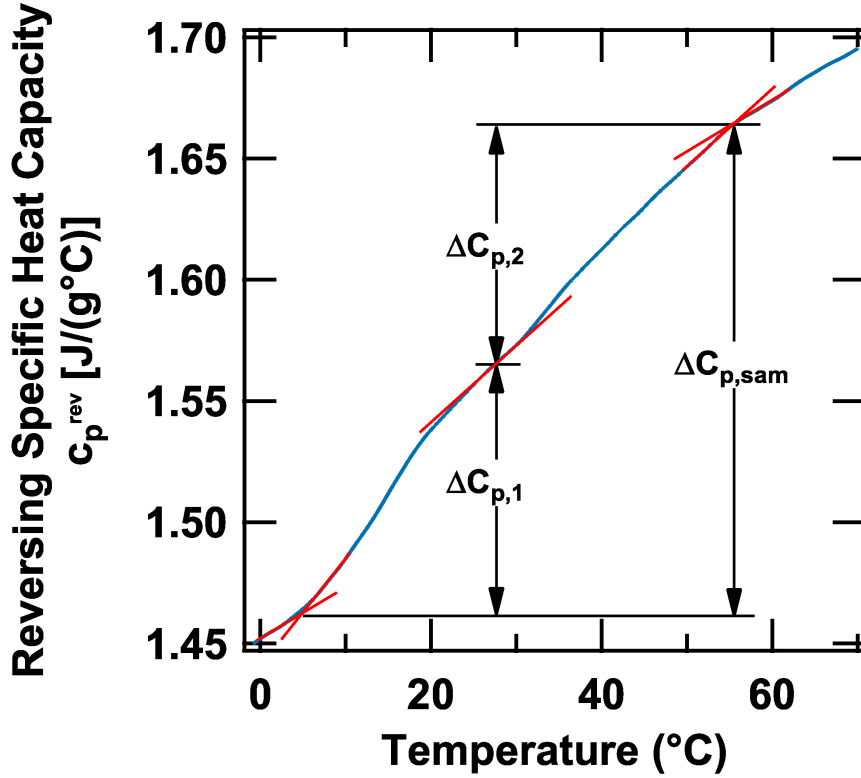


**Figure 3.5:** A closer view of  $c_p^{rev}$  of rrP3HT showing how  $\Delta C_{p,sam}$  was split into  $\Delta C_{p,1}$  and  $\Delta C_{p,2}$  for the calculation of MAF and RAF respectively.

Figure 3.3d). In this light, an alternate calculation was performed whereby  $\Delta C_{p,sam}$  was divided into  $\Delta C_{p,1}$  and  $\Delta C_{p,2}$ , as shown in Figure 3.5, to represent the devitrification of the MAF then RAF successively. Since  $\Delta C_{p,1}$  occurs in the same location as the fully mobile ranP3HT  $T_g$ , this transition is due to the MAF which means  $\Delta C_{p,2}$  is therefore the relaxation of the RAF in rrP3HT. By dividing  $\Delta C_{p,1}$  and  $\Delta C_{p,2}$  by  $\Delta C_{p,amor}$  the mass percentages of MAF and RAF were found, respectively, and are shown in Table 3.1. One can also use  $\Delta C_{p,1}$  as  $\Delta C_{p,sam}$  in Equation 3.2 to obtain a similar RAF to Table 3.1. The similar result from both methods validates the assignment of  $\Delta C_{p,2}$  as the RAF transition. Finally, a summation of all three phases gives 97.6% which, although less than 100%, is accurate considering the error in  $\Delta C_{p,amor}$  is  $\approx 6\%$ . These results are comparable with calculations performed on other semicrystalline polymers.[16]

**Table 3.1:** Measurements from TMDSC of rrP3HT

	Crystalline Fraction	MAF	RAF	Sum
Measured Values	$\Delta H_m = 18.0 \text{ J/g}$	$\Delta C_{p,1} = 0.097 \text{ J/g}^\circ\text{C}$	$\Delta C_{p,2} = 0.081 \text{ J/g}^\circ\text{C}$	
Calculated Percentage	42.0%	30.3%	25.3%	97.6%

The RAF calculated here represents at least a fraction of the tie molecules and dangling chain ends that protrude from the rrP3HT crystallites formed from the non-isothermal crystallization performed prior to data collection, as was described earlier. This would be the only location where amorphous polymer chains are under constraint in this experiment. Due to this, the RAF is potentially an essential part of the charge transfer interface between crystalline and amorphous polymer regions (i.e. MAF) or between crystallites and fullerene aggregates in solar cells. Changes in this morphology due to spin coating is discussed in the following sections.

### 3.3.3 RAF Calculation for Thin Film ranP3HT

While analyzing the physical properties of bulk P3HT is fundamental to the understanding of the material itself, the polymer is typically processed into thin films and fibers for use in optoelectronic devices. Thus, how the previously discussed phases change when going from bulk to thin film must be investigated. To this end, 220 nm films of both ranP3HT and rrP3HT were prepared by spin coating from individual chlorobenzene solutions onto PEDOT:PSS coated glass substrates. There are two reasons why PEDOT:PSS was coated onto the glass substrates. First, in the conventional polymer solar cell architecture, PEDOT:PSS is deposited as a common electron blocking layer between the bulk heterojunction and the anode (or in this case the glass substrate). This directly links these results to such applications. Second, in contrast to P3HT, PEDOT:PSS is water soluble which makes it an appropriate sacrificial material to aid in the release of the top P3HT layer from the substrate for TMDSC analysis. This approach to obtain in tact thin films has been applied in previous research from this group.[40, 41] Further details of film fabrication and removal can be found in the experimental section of this chapter.

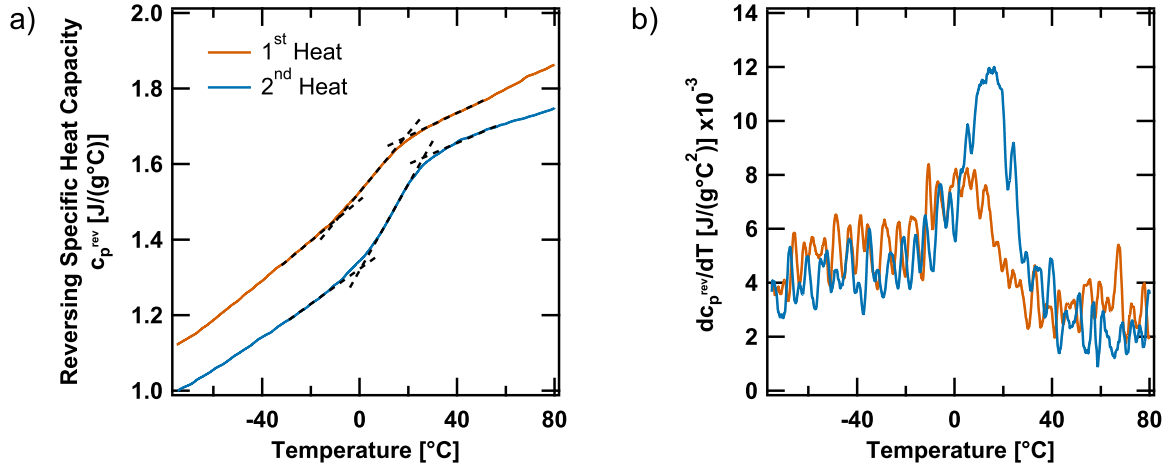


**Figure 3.6:** Graphs showing  $c_p^{rev}$  in the  $T_g$  region of a ranP3HT thin film (a) and its derivative (b). Both first heat and second heat data are shown to illustrate the difference in  $\Delta C_p$  due to thin film effects. Graphs in (a) are vertically offset for clarity.

Figure 3.6 shows TMDSC first and second heating scans of a ranP3HT thin film sample in the  $T_g$  region. There is a clear difference in  $\Delta C_p$  of the sample in the two runs. The second heat is similar to the bulk ranP3HT that was described in the previous section ( $\Delta C_p = 0.30$  J/g°C  $\approx \Delta C_{p,amor}$ ). This confirms that the material has returned to its bulk state after quenching from 300°C. However, the lower  $\Delta C_{p,sam} = 0.20$  J/g°C of the first heat clearly shows that some of the material is *missing* from this transition as is evident in the derivative curves also (see Figure 3.6b). Additionally, there is a reduction in  $T_g$  to  $\sim 8^\circ\text{C}$ . There is a wealth of information concerning changes in thermal properties due to interfacial effects in polymer thin films from which an explanation of this data can be devised.

Research has shown that depending on the nature of the interaction at the polymer/substrate interface, differences in thermal expansion, chain mobility and stiffness between polymer chains close to the interface and in the bulk film will arise.[42–50] This can cause deviations (mainly an increase) in the  $T_g$  though its effective range is limited; only becoming a factor in films  $\leq 50$  nm thick which is not the case here. It should be noted that Huang et al.[51] showed that PEDOT:PSS and P3HT have the ability

to chemically react at the interface on annealing, which suggests the characteristics of this interface may play at least a minor role in the observed behavior.

With regard to the free polymer surface, thin polymer films have a liquid-like behavior (higher mobility) which depresses the overall  $T_g$  as observed by various methods.[42, 52–58] Experiments and simulations demonstrating this have mainly employed polystyrene and poly(methyl methacrylate) as model systems, showing an effective range of  $\leq 100$  nm. It is therefore practical to assume that the inter- and intramolecular interactions present in P3HT,[5, 22, 23, 59] coupled with both interface and free surface effects, will extend these ranges and alter the properties of the films studied in this section. Since the outcome is a reduced  $T_g$  in the thin film as compared to the bulk, the free surface effect clearly dominates in the case of ranP3HT.

While it follows that the interactions in ranP3HT thin films are similar to other amorphous polymers, further analysis using the  $\Delta C_{p,sam}$  value obtained from Figure 3.6a can be accomplished. With knowledge of the film thickness ( $t$ ) and  $\Delta C_{p,amor}$ , the thickness of the layer formed at the air interface ( $t_{int}$ ) can be calculated using the equation:[60]

$$t_{int} = t \left( 1 - \frac{\Delta C_{p,sam}}{\Delta C_{p,amor}} \right) \quad (3.3)$$

The bracketed term is simply the *missing* fraction of a 100% amorphous (i.e. zero crystalline fraction) material which is valid for ranP3HT. Treating the ranP3HT film as a bilayer, one bulk-like and one liquid-like, Equation 3.3 can be used to calculate the thickness of the liquid-like top layer of the ranP3HT film: an approach that has proven effective in the past.[42] The result  $t_{int} = \mathbf{82.5\ nm}$  represents **37.5%** of the total film thickness that, in comparison, is  $\sim 20$  nm thicker than the same layer found in polystyrene thin films according to simulations.[45] This supports the aforementioned claim of the additional effect of inter- and intramolecular forces in P3HT. It is important to note that the liquid-like layer — by its very definition — should not be referred to as a RAF since that would cause an increase in  $T_g$  as in the section above or show a second  $T_g$  like bulk rrP3HT.

### 3.3.4 RAF Calculation for Thin Film rrP3HT

Attention is now directed towards the semicrystalline rrP3HT thin films. As is displayed in Figure 3.7a and b, the MAF transition seems to be the most affected by spin coating, evidenced by the difference in intensity of the derivative curve in that region (see Figure 3.7b). The other two regions (RAF and side chain regions to the right and left respectively) appear unchanged between first and second heating of the thin film sample. So where did the rest of material that should be in the MAF region go?

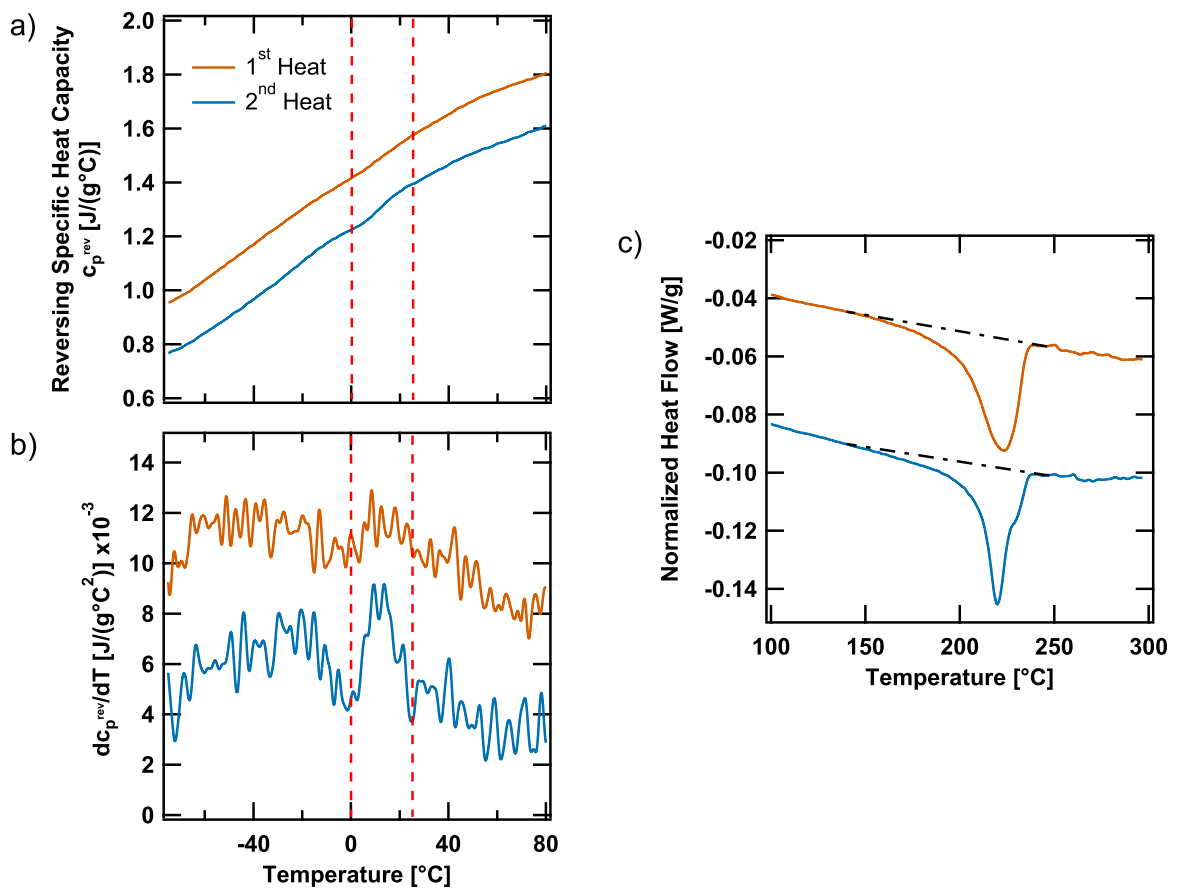


**Figure 3.7:** Graphs showing  $c_p^{rev}$  in the  $T_g$  region of a rrP3HT thin film (a) and its derivative (b) as well as a magnification of the melting region (c). Red dashed lines in (a) and (b) indicate side chain, MAF and RAF regions respectively. Black dot-dashed line in (c) illustrates the baseline from which crystallinity was measured. Graphs are vertically offset for clarity.

It is immediately observed that the melting region shown in Figure 3.7c is also different between the first and second heat. As opposed to the peak and shoulder outline of bulk rrP3HT melting curve, the thin film melting curve exhibits a single broad peak. This might imply an increased distribution of crystal sizes present in the spun cast film, which is a direct result of the kinetic processes involved in spin coating, compared to the bulk.

**Table 3.2:** Calculated percentages of the three phases in rrP3HT thin films.

	Crystallinity	MAF	RAF	Sum
1 <sup>st</sup> Heat (thin film)	48.0 ± 3.8%	23.5 ± 3.2%	25.5 ± 6.4%	97.0%
2 <sup>nd</sup> Heat (bulk-like)	43.0 ± 3.2%	28.9 ± 2.4%	25.4 ± 4.1%	97.3%

To confirm the above observations, the three polymer phases were quantified as was done for bulk rrP3HT in Section 2.3.2 and the results tabulated in Table 3.2. As was stated above, the MAF is smaller in the thin film than the bulk. Notably, the second heating scan shows identical results to the previously calculated bulk rrP3HT, confirming the return of the thin film sample to the bulk state after non-isothermal crystallization from the melt. Interestingly, the  $\sim 5\%$  decrease of MAF accompanies a similar increase in the polymer thin film crystallinity compared to bulk values. Schönher and Frank reported,[61, 62] while investigating poly(ethylene oxide), that the theory for bulk crystallization holds in thin films but absolute crystallinity decreases with film thickness. The films in this study did not suffer this loss of crystallinity, negating this effect. However, Tsuruta et al. have recently reported polymer chain orientation due to spin coating close to the interface in polystyrene/quartz samples which does not relax until well above  $T_g$ . [63] This orientation could reduce MAF in the film and potentially nucleate crystals at the polymer/substrate interface. Therefore forces involved in spin coating produced a thin film with both increased crystal size distribution and overall crystallinity yet with a similar RAF to the bulk polymer. This constant RAF may be an indication that the interfacial width between a crystal and

surrounding amorphous chains (MAF) arrived at an equilibrium value in the pure material — at least within the boundaries of this experiment. In contrast to the ranP3HT thin film, no evidence of a liquid-like layer is observed as the sum of all polymer phases in Table 3.2 accounts for the total mass of the rrP3HT thin film sample, within error. The ability of the polymer to crystallize therefore nullified the surface effect observed in thin film ranP3HT.

### 3.4 Conclusion

In conclusion, it has been found that the amorphous regions of rrP3HT relax before a rather modest 65°C, well below typical P3HT annealing temperatures (120 – 140°C). The result not only represents the first quantification of these morphological entities in rrP3HT, but also has implications in the description of the charge transfer interface in electronic devices made from it. Qualitative confirmation of the results from bulk rrP3HT was recently published[59] highlighting the growing attention towards better insight into the RAF for semiconducting polymers.

Thin films of ranP3HT contain a 82.5 nm liquid-like layer similar to that discovered at the surface of other amorphous polymers. The characteristics of this layer lead to  $T_g$  depression which distinguishes it from the RAF found in rrP3HT. Compared to bulk rrP3HT, crystallinity and MAF for thin film rrP3HT were increased and decreased respectively and are attributed to effects of spin coating on the film morphology.

This study underlines the non-trivial nature of the morphology of semicrystalline, semiconducting polymers and the thin films fabricated from them. In both the bulk and thin film state, a three phase model should always be used to fully describe the material’s morphology. Additionally, many of the high performance semiconducting polymers being studied currently are completely amorphous which places even more importance on the MAF and RAF that are formed in these systems. It was also shown that interfacial effects in the thin film state should always be included when considering amorphous semiconducting polymers. Quantitative research into the disordered

phases of polymer semiconductors will deepen the understanding of the morphology necessary to optimize electronic device performance.

## BIBLIOGRAPHY

- [1] Svetlana S. van Bavel, Maik Bärenklau, Gijsbertus de With, Harald Hoppe, and Joachim Loos. P3HT/PCBM Bulk Heterojunction Solar Cells: Impact of Blend Composition and 3D Morphology on Device Performance. *Adv. Funct. Mater.*, 20(9):1458–1463, apr 2010.
- [2] Sudip Malik and Arun K. Nandi. Crystallization mechanism of regioregular poly(3-alkyl thiophene)s. *J. Polym. Sci. Part B Polym. Phys.*, 40(18):2073–2085, sep 2002.
- [3] Ovidiu F. Pascui, Ruth Lohwasser, Michael Sommer, Mukundan Thelakkat, Thomas Thurn-Albrecht, and Kay Saalwachter. High Crystallinity and Nature of Crystal–Crystal Phase Transformations in Regioregular Poly(3-hexylthiophene). *Macromolecules*, 43(22):9401–9410, nov 2010.
- [4] Jens Balko, Ruth H. Lohwasser, Michael Sommer, Mukundan Thelakkat, and Thomas Thurn-Albrecht. Determination of the Crystallinity of Semicrystalline Poly(3-hexylthiophene) by Means of Wide-Angle X-ray Scattering. *Macromolecules*, 46:9642–9651, dec 2013.
- [5] Cameron S. Lee and Mark D. Dadmun. Important thermodynamic characteristics of poly(3-hexyl thiophene). *Polymer*, 55(1):4–7, jan 2014.
- [6] Roddel Remy, Emily Daniels Weiss, Ngoc A. Nguyen, Sujun Wei, Luis M. Campos, Tomasz Kowalewski, and Michael E. Mackay. Enthalpy of fusion of poly(3-hexylthiophene) by differential scanning calorimetry. *J. Polym. Sci. Part B Polym. Phys.*, 52(22):1469–1475, nov 2014.
- [7] Chad R. Snyder, Ryan C. Nieuwendaal, Dean M. DeLongchamp, Christine K. Luscombe, Prakash Sista, and Shane D. Boyd. Quantifying Crystallinity in High Molar Mass Poly(3-hexylthiophene). *Macromolecules*, 47(12):3942–3950, jun 2014.

- [8] R.J. Kline, M.D. McGehee, E.N. Kadnikova, J. Liu, and J.M.J. Fréchet. Controlling the Field-Effect Mobility of Regioregular Polythiophene by Changing the Molecular Weight. *Adv. Mater.*, 15(18):1519–1522, sep 2003.
- [9] RJ Kline, MD McGehee, EN Kadnikova, Jinsong Liu, Jean MJ Frechet, and Michael F Toney. Dependence of regioregular poly (3-hexylthiophene) film morphology and field-effect mobility on molecular weight. *Macromolecules*, 38:3312–3319, 2005.
- [10] Rui Zhang, Bo Li, Mihaela C Iovu, Malika Jeffries-El, Geneviève Sauvé, Jessica Cooper, Shijun Jia, Stephanie Tristram-Nagle, Detlef M Smilgies, David N Lambeth, Richard D McCullough, and Tomasz Kowalewski. Nanostructure Dependence of Field-Effect Mobility in Regioregular Poly (3-hexylthiophene) Thin Film Field Effect Transistors. *J. Am. Chem. Soc.*, 128(11):3480–3481, 2006.
- [11] Jui-Fen Chang, Jenny Clark, Ni Zhao, Henning Sirringhaus, Dag W. Breiby, Jens W. Andreasen, Martin M. Nielsen, Mark Giles, Martin Heeney, and Iain McCulloch. Molecular-weight dependence of interchain polaron delocalization and exciton bandwidth in high-mobility conjugated polymers. *Phys. Rev. B*, 74(11):115318, sep 2006.
- [12] Ajay A Virkar, Stefan Mannsfeld, Zhenan Bao, and Natalie Stingelin. Organic semiconductor growth and morphology considerations for organic thin-film transistors. *Adv. Mater.*, 22(34):3857–75, sep 2010.
- [13] Felix Peter Vinzenz Koch, Jonathan Rivnay, Sam Foster, Christian Müller, Jonathan M. Downing, Ester Buchaca-Domingo, Paul Westacott, Liyang Yu, Mingjian Yuan, Mohammed Baklar, Zhuping Fei, Christine Luscombe, Martyn A. McLachlan, Martin Heeney, Garry Rumbles, Carlos Silva, Alberto Salleo, Jenny Nelson, Paul Smith, and Natalie Stingelin. The impact of molecular weight on

- microstructure and charge transport in semicrystalline polymer semiconductors—poly(3-hexylthiophene), a model study. *Prog. Polym. Sci.*, 38(12):1978–1989, dec 2013.
- [14] Rodrigo Noriega, Jonathan Rivnay, Koen Vandewal, Felix P V Koch, Natalie Stingelin, Paul Smith, Michael F Toney, and Alberto Salleo. A general relationship between disorder, aggregation and charge transport in conjugated polymers. *Nat. Mater.*, 12(11):1038–44, nov 2013.
- [15] Sean Sweetnam, Kenneth R Graham, Guy O Ngongang Ndjawa, Thomas Heumüller, Jonathan A Bartelt, Timothy M Burke, Wentao Li, Wei You, Aram Amassian, and Michael D McGehee. Characterization of the polymer energy landscape in polymer:fullerene bulk heterojunctions with pure and mixed phases. *J. Am. Chem. Soc.*, 136(40):14078–88, oct 2014.
- [16] Hidematsu Suzuki, Janusz Grebowicz, and Bernhard Wunderlich. Glass transition of poly (oxymethylene). *Br. Polym. J.*, 17:1–3, 1985.
- [17] B Wunderlich. Reversible crystallization and the rigid-amorphous phase in semicrystalline macromolecules. *Prog. Polym. Sci.*, 28:383–450, 2003.
- [18] Albert Sargsyan, Anahit Tonoyan, Sevan Davtyan, and Christoph Schick. The amount of immobilized polymer in PMMA SiO<sub>2</sub> nanocomposites determined from calorimetric data. *Eur. Polym. J.*, 43(8):3113–3127, aug 2007.
- [19] Andreas Wurm, Mohamed Ismail, Bernd Kretzschmar, Doris Pospiech, and Christoph Schick. Retarded Crystallization in Polyamide/Layered Silicates Nanocomposites caused by an Immobilized Interphase. *Macromolecules*, 43(3):1480–1487, feb 2010.
- [20] Sharon Xin Lu and Peggy Cebe. Effects of annealing on relaxation behavior and charge trapping in film-processed poly(phenylene sulfide). *J. Appl. Polym. Sci.*, 61(3):473–483, jul 1996.

- [21] Susmita Pal and Arun K. Nandi. Cococrystallization mechanism of poly(3-alkyl thiophenes) with different alkyl chain length. *Polymer*, 46(19):8321–8330, sep 2005.
- [22] Shireesh Pankaj, Elke Hempel, and Mario Beiner. Side-Chain Dynamics and Crystallization in a Series of Regiorandom Poly(3-alkylthiophenes). *Macromolecules*, 42(3):716–724, feb 2009.
- [23] Ryan C. Nieuwendaal, Chad R. Snyder, and Dean M. DeLongchamp. Measuring Order in Regioregular Poly(3-hexylthiophene) with Solid-State  $^{13}\text{C}$  CP/MAS NMR. *ACS Macro Lett.*, 3(2):130–135, feb 2014.
- [24] Bryan S. Beckingham, Victor Ho, and Rachel A. Segalman. Formation of a Rigid Amorphous Fraction in Poly(3-(2'-ethyl)hexylthiophene). *ACS Macro Lett.*, pages 684–688, jul 2014.
- [25] Jun Zhao, Ann Swinnen, Guy Van Assche, Jean Manca, Dirk Vanderzande, and Bruno Van Mele. Phase diagram of P3HT/PCBM blends and its implication for the stability of morphology. *J. Phys. Chem. B*, 113(6):1587–91, feb 2009.
- [26] Jun Zhao, Sabine Bertho, Joke Vandenbergh, Guy Van Assche, Jean Manca, Dirk Vanderzande, Xiaoqing Yin, Jingdan Shi, Thomas Cleij, Laurence Lutsen, Bruno Van Mele, Guy Van Assche, and Bruno Van Mele. Phase behavior of PCBM blends with different conjugated polymers. *Phys. Chem. Chem. Phys.*, 13(26):12285–92, jul 2011.
- [27] Trinh Tung Ngo, Duc Nghia Nguyen, and Van Tuyen Nguyen. Glass transition of PCBM, P3HT and their blends in quenched state. *Adv. Nat. Sci. Nanosci. Nanotechnol.*, 3(4):045001, sep 2012.
- [28] Richard D. McCullough. The Chemistry of Conducting Polythiophenes. *Adv. Mater.*, 10(2):93–116, jan 1998.

- [29] Bernhard Wunderlich, Yimin Jin, and Andreas Boller. Mathematical description of differential scanning calorimetry based on periodic temperature modulation. *Thermochim. Acta*, 238:277–293, jun 1994.
- [30] A. A. Lacey, C. Nikolopoulos, and M. Reading. A mathematical model for Modulated Differential Scanning Calorimetry. *J. Therm. Anal.*, 50(1-2):279–333, sep 1997.
- [31] P. S. Gill, S. R. Sauerbrunn, and M. Reading. Modulated differential scanning calorimetry. *J. Therm. Anal.*, 40(3):931–939, feb 1993.
- [32] M. Reading, D. Elliott, and V. L. Hill. A new approach to the calorimetric investigation of physical and chemical transitions. *J. Therm. Anal.*, 40(3):949–955, feb 1993.
- [33] Mike Reading. Modulated Differential Scanning Calorimetry - A New Way Forward in Materials Characterization. *Trends Polym. Sci.*, 1(8):248 – 253, 1993.
- [34] B Wunderlich. Study of the change in specific heat of monomeric and polymeric glasses during the glass transition. *J. Phys. Chem.*, 64:1052–1056, 1960.
- [35] Nishio Hirai and Henry Eyring. Bulk Viscosity of Liquids. *J. Appl. Phys.*, 29(5):810, jun 1958.
- [36] Nishio Hirai and Henry Eyring. Bulk viscosity of polymeric systems. *J. Polym. Sci.*, 37(131):51–70, may 1959.
- [37] Bernhard Wunderlich. *Thermal Analysis of Polymeric Materials*. Springer, New York, 2005.
- [38] Zhiyong Wu, Albrecht Petzold, Thomas Henze, Thomas Thurn-Albrecht, Ruth H. Lohwasser, Michael Sommer, and Mukundan Thelakkat. Temperature and Molecular Weight Dependent Hierarchical Equilibrium Structures in Semiconducting Poly(3-hexylthiophene). *Macromolecules*, 43(10):4646–4653, may 2010.

- [39] Yuan Yuan, Jianming Zhang, Jiaqian Sun, Jian Hu, Tongping Zhang, and Yongxin Duan. Polymorphism and Structural Transition around 54 C in Regioregular Poly(3-hexylthiophene) with High Crystallinity As Revealed by Infrared Spectroscopy. *Macromolecules*, 44(23):9341–9350, dec 2011.
- [40] Jonathon Kiel, Aaron Eberle, and Michael Mackay. Nanoparticle Agglomeration in Polymer-Based Solar Cells. *Phys. Rev. Lett.*, 105(16):1–4, oct 2010.
- [41] Hao Shen, Wenluan Zhang, and Michael E. Mackay. Dual length morphological model for bulk-heterojunction, polymer-based solar cells. *J. Polym. Sci. Part B Polym. Phys.*, 52(5):387–396, mar 2014.
- [42] Joseph L. Keddie, Richard A. L. Jones, and Rachel A. Cory. Interface and surface effects on the glass-transition temperature in thin polymer films. *Faraday Discuss.*, 98(0):219, 1994.
- [43] W. E. Wallace, J. H. van Zanten, and W. L. Wu. Influence of an impenetrable interface on a polymer glass-transition temperature. *Phys. Rev. E*, 52(4):R3329–R3332, oct 1995.
- [44] John H. van Zanten, William E. Wallace, and Wen-li Wu. Effect of strongly favorable substrate interactions on the thermal properties of ultrathin polymer films. *Phys. Rev. E*, 53(3):R2053–R2056, mar 1996.
- [45] J. A. Torres, P. F. Nealey, and J. J. de Pablo. Molecular Simulation of Ultrathin Polymeric Films near the Glass Transition. *Phys. Rev. Lett.*, 85(15):3221–3224, oct 2000.
- [46] David S. Fryer, Paul F. Nealey, and Juan J. de Pablo. Scaling of  $T_{\text{sub g}}$  and reaction rate with film thickness in photoresist: A thermal probe study. *J. Vac. Sci. Technol. B Microelectron. Nanom. Struct.*, 18(6):3376, 2000.
- [47] Christopher L. Soles, Eric K. Lin, Joseph L. Lenhart, Ronald L. Jones, Wen-li Wu, Dario L. Goldfarb, and Marie Angelopoulos. Thin film confinement effects

- on the thermal properties of model photoresist polymers. *J. Vac. Sci. Technol. B Microelectron. Nanom. Struct.*, 19(6):2690, 2001.
- [48] Charles D. Wood, Lawrence Chen, Craig Burkhart, Karl W. Putz, John M. Torkelson, and L. Catherine Brinson. Measuring interphase stiffening effects in styrene-based polymeric thin films. *Polymer*, 75:161–167, sep 2015.
- [49] Shadid Askar, Christopher M. Evans, and John M. Torkelson. Residual stress relaxation and stiffness in spin-coated polymer films: Characterization by ellipsometry and fluorescence. *Polymer*, 76:113–122, oct 2015.
- [50] Manabu Inutsuka, Ayanobu Horinouchi, and Keiji Tanaka. Aggregation States of Polymers at Hydrophobic and Hydrophilic Solid Interfaces. *ACS Macro Lett.*, 4(10):1174–1178, oct 2015.
- [51] David M. Huang, Scott A. Mauger, Stephan Friedrich, Simon J. George, Daniela Dumitriu-LaGrange, Sook Yoon, and Adam J. Moulé. The Consequences of Interface Mixing on Organic Photovoltaic Device Characteristics. *Adv. Funct. Mater.*, 21(9):1657–1665, may 2011.
- [52] Kevin F. Mansfield and Doros N. Theodorou. Molecular dynamics simulation of a glassy polymer surface. *Macromolecules*, 24(23):6283–6294, nov 1991.
- [53] G Reiter. Mobility of Polymers in Films Thinner than Their Unperturbed Size. *Europhys. Lett.*, 23(8):579–584, sep 1993.
- [54] J. L Keddie, R. A. L Jones, and R. A Cory. Size-Dependent Depression of the Glass Transition Temperature in Polymer Films. *Europhys. Lett.*, 27(1):59–64, jul 1994.
- [55] B. Frank, A. P. Gast, T. P. Russell, H. R. Brown, and C. Hawker. Polymer Mobility in Thin Films. *Macromolecules*, 29(20):6531–6534, jan 1996.

- [56] James A. Forrest and Johan Mattsson. Reductions of the glass transition temperature in thin polymer films: Probing the length scale of cooperative dynamics. *Phys. Rev. E*, 61(1):R53–R56, jan 2000.
- [57] David S. Fryer, Paul F. Nealey, and Juan J. de Pablo. Thermal Probe Measurements of the Glass Transition Temperature for Ultrathin Polymer Films as a Function of Thickness. *Macromolecules*, 33(17):6439–6447, aug 2000.
- [58] J. Mattsson, J. A. Forrest, and L. Börjesson. Quantifying glass transition behavior in ultrathin free-standing polymer films. *Phys. Rev. E*, 62(4):5187–5200, oct 2000.
- [59] Xiaobo Shen, Weiguo Hu, and Thomas P. Russell. Measuring the Degree of Crystallinity in Semicrystalline Regioregular Poly(3-hexylthiophene). *Macromolecules*, 49(12):4501–4509, jun 2016.
- [60] B. Morèse-Séguéla, M. St-Jacques, J. M. Renaud, and J. Prod’homme. Microphase Separation in Low Molecular Weight Styrene-Isoprene Diblock Copolymers Studied by DSC and  $^{13}\text{C}$  NMR. *Macromolecules*, 13(1):100–106, jan 1980.
- [61] Holger Schönherr and Curtis W. Frank. Ultrathin Films of Poly(ethylene oxides) on Oxidized Silicon. 1. Spectroscopic Characterization of Film Structure and Crystallization Kinetics. *Macromolecules*, 36(4):1188–1198, feb 2003.
- [62] Holger Schönherr and Curtis W. Frank. Ultrathin Films of Poly(ethylene oxides) on Oxidized Silicon. 2. In Situ Study of Crystallization and Melting by Hot Stage AFM. *Macromolecules*, 36(4):1199–1208, feb 2003.
- [63] Hirofumi Tsuruta, Yoshihisa Fujii, Naoki Kai, Hiroshi Kataoka, Takashi Ishizone, Masao Doi, Hiroshi Morita, and Keiji Tanaka. Local Conformation and Relaxation of Polystyrene at Substrate Interface. *Macromolecules*, 45(11):4643–4649, jun 2012.

## Chapter 4

### REFINING THE DESCRIPTION OF THE POLYMER:FULLERENE BULK HETEROJUNCTION

#### 4.1 Introduction

In the last two chapters, the enthalpy of fusion for regioregular P3HT (rrP3HT) was found and applied to bulk and thin film morphologies to evaluate the polymer's crystallinity under those conditions. The discussion in this chapter goes one step further to calculate rrP3HT crystallinity in a thin film blended with phenyl-C<sub>61</sub>-butyric acid methyl ester (PCBM) in a morphology known as a bulk heterojunction (BHJ).

BHJs have been studied in the past by using scattering techniques.[1–4] These methods typically take advantage of the contrast created between P3HT and PCBM, especially when PCBM is phase separated. Thus quantitative knowledge of the extent of PCBM phase separation and its relative distribution in the BHJ is easily available. However, the lack of contrast within individual phases of the BHJ, whether pure or mixed, is the Achilles heel of these techniques.[1] Diffraction, both X-ray and electron, has been able to identify changes in P3HT crystallinity and some BHJ models have been proposed from this information.[5–7] Unfortunately, the results of these measurements still remain qualitative in nature.

Calorimetric studies have shown promise in this field. Differential scanning calorimetry has enabled the acquisition of information about the melting behavior, glass transition ( $T_g$ ) and crystallization events of pure components and BHJ mixtures.[8, 9] By investigating a range of PCBM concentrations in various donor polymers, phase diagrams have been constructed that can describe the BHJ morphology under different conditions.[10–14] The eutectic point on these diagrams, for example, has been shown to be related to the optimal PCBM concentration for best solar device performance.[11]

A limiting factor of calorimetric analysis is the lack of information about the enthalpy of fusion ( $\Delta H_m^\infty$ ) of the pure materials which would allow for a fully quantitative study. For that reason, identifying  $\Delta H_m^\infty$  for P3HT was imperative.

Conclusions from calorimetry also come from bulk measurements, where assumptions about equilibrium mixing can be made. Applications of BHJs in solar cells typically require films on the order of 100 – 200 nm thick, in which non-equilibrium structures may be present and must be understood. A quantitative analysis of 1:1 P3HT:PCBM BHJ thin films is discussed in this chapter, thereby refining what is currently known about polymer:fullerene BHJ morphology.

## 4.2 Experimental

BHJs were made by mixing 1:1 ratio of P3HT (Luminescence Technologies Corp) and PCBM (Nano-C) in chlorobenzene (Acros Organics) to make a total solution concentration of 30 mg/mL. The solution was first stirred at 40 °C for a few hours to facilitate the dissolution of larger aggregates. Then the heat was turned off and the solution left to stir overnight.

Borosilicate glass substrates measuring 4" dia.  $\times$  1/8" thick, were used in this work, compared to 1" squares used for device fabrication, to increase the total film mass for TMDSC experiments. The substrates were thoroughly cleaned using soapy water, deionized water, acetone and isopropyl alcohol. Finally they were treated with UV ozone for at least 30 minutes. PEDOT:PSS dispersion (Clevios Al 4083) was then spun onto the cleaned substrates at 3000 rpm and dried in an oven at 130 °C for 15 minutes. Finally the P3HT:PCBM solution was deposited and spun at 600 rpm for 1 minute in a N<sub>2</sub> glovebox to create the BHJ film. Final thicknesses were 40 nm and 190 nm for PEDOT:PSS and BHJ respectively, measured by X-ray reflectivity (Rigaku Ultima IV, CuK $\alpha$ ,  $\lambda$ = 0.154 nm).

Retrieving the films for experimentation involved immersing them in deionized water, which dissolved the underlying PEDOT:PSS, releasing them from the substrate. Films were collected from the water's surface and vacuum dried at room temperature

for 2 days after which they were placed into aluminum DSC pans for testing (two films per sample pan amounting to  $\sim 4$  mg). Any reference to annealing refers to a heat treatment at 140 °C for 20 minutes unless stated otherwise. Annealing of the BHJ films were performed under two different conditions; on a hotplate in a N<sub>2</sub> glovebox while still on the substrate or in the DSC after being removed from the substrate (see next section).

For comparison to the more traditional DSC sample preparation method, drop cast samples were also made by depositing some of the BHJ solution onto a cleaned glass slide. This was done in a N<sub>2</sub> glovebox where it was left to dry for 24 hours. The films were then scratched off of the slide to make a DSC sample.

TMDSC experiments were done with a TA Instruments Discovery DSC in *heat-only* mode to ensure accurate crystallinity measurements (see full TMDSC explanation in Chapter 3.2 and calibration procedure in Chapter 1.2). The parameters are 3 °C/min, 30 seconds and  $\pm 0.239$  °C for the heating rate, oscillation period and amplitude respectively.

## 4.3 Results and Discussion

### 4.3.1 Chemical Reaction at the PEDOT:PSS Interface

To properly characterize the BHJ films in the annealed state, it must be shown that the PEDOT:PSS layer was completely removed. Huang et al.[15] showed that with annealing, P3HT mixes and reacts with the PSS enriched surface of PEDOT:PSS to form an insoluble interfacial layer while Guralnick et al.[16] showed that it may be possible for PCBM to diffuse across that interface as well. Despite some unanswered questions in both reports, this undertaking could be hampered by these processes due to mass fraction changes in the films. Thus preliminary experiments were performed to investigate the potential effect of these processes on TMDSC results. Xu et al. was able to identify "residue" of PEDOT:PSS on BHJ films by X-ray photoelectron spectroscopy (XPS) and a similar study is carried out here.[17]

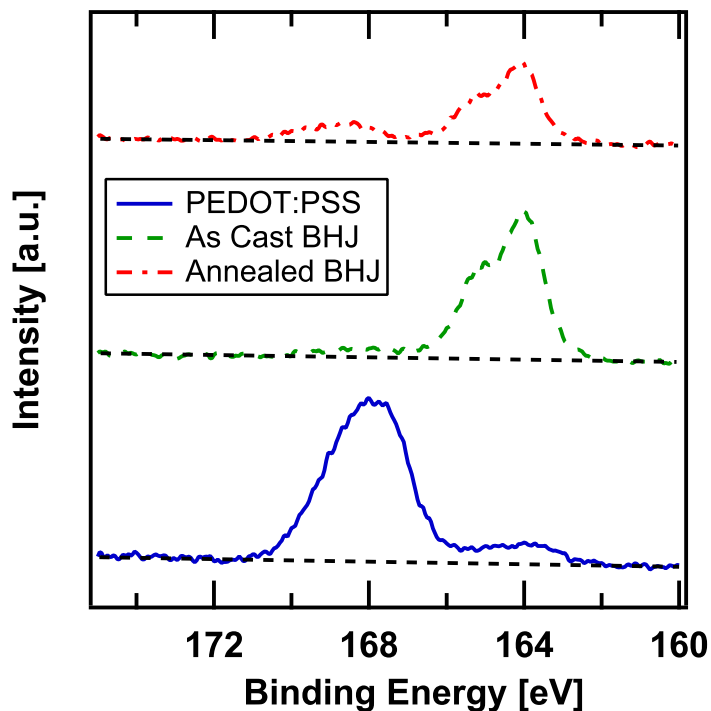


**Figure 4.1:** S(2p) XPS spectra of PEDOT:PSS (bottom), as cast (middle) and annealed (top) BHJ films. The BHJ film spectra are of the backside of the film that was in contact with the PEDOT:PSS sub-layer. Dashed lines linearly connect the data at either end of the observed peaks and are guides to the eye.

Figure 4.1 shows XPS spectra in the S(2p) region of three samples. A PEDOT:PSS thin film was examined as a control which is clearly dominated by the binding energy peak at 168 eV corresponding to the sulfur atoms in PSS. The minor peak at 164 eV is due to the sulfur atoms in PEDOT which would be chemically identical to the sulfur atoms in P3HT. The significantly larger PSS signal is indicative of the PSS enriched surface of the PEDOT:PSS film and can be used as an identifier for PEDOT:PSS diffusion.[18] Two BHJ films, as cast and annealed, were made (see Experimental Section) and inverted onto bare silicon substrates so that the interface that was in contact with PEDOT:PSS could be analyzed. It is clear the annealed film contains residue of insoluble PSS likely from the interfacial chemical reaction as the

literature suggests.[15] Also note the decrease in intensity of the overlapping peaks at 164 and 165 eV likely signifies an increase in PCBM concentration at that interface.[17]

As a secondary confirmation, a DSC experiment was performed on PEDOT:PSS (see Figure 4.2a) at 10°C/min and the first heat displays a large endotherm ascribed to the evaporation of water from the material due to the hygroscopic nature of PSS.[19] TMDSC of BHJ films annealed on PEDOT:PSS (Figure 4.2b) unfortunately shows the same behavior in a similar region and even some PEDOT:PSS degradation above 250 °C (downturn in heat flow baseline).[19] Consequently, an alternative annealing method whereby the BHJ films are removed in the as cast state, dried, annealed in the DSC at the same temperature and time, then quenched to the starting temperature prior to testing is employed here and shown in Figure 4.2b. Since the films are annealed after removal from the substrate, no trace of PEDOT:PSS is present and the heat flow shows similar, if not more refined, transitions. Thus a full quantitative analysis of annealed BHJ films can be accomplished with this method.

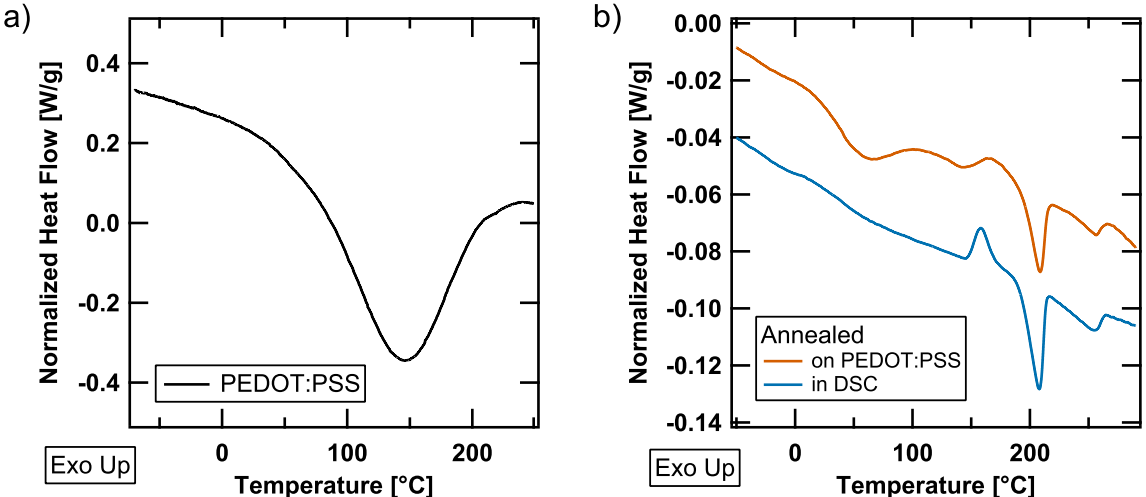


**Figure 4.2:** (a) 1<sup>st</sup> heat DSC of PEDOT:PSS showing the release of water on heating. (b) TMDSC total heat flow of BHJ samples annealed on a PEDOT:PSS coated substrate (showing evidence of PSS residue) and in the DSC. Data in (b) shifted vertically for clarity.

### 4.3.2 TMDSC and Crystallinity Analysis

Figure 4.3 shows the results of TMDSC experiments for the examined spun cast and drop cast samples. Only first heat data is examined since it contains all of the processing history of the sample which is the main focus of this research. Also, Leman et al. has recently warned against thermal cycling of C<sub>60</sub> derivatives, like PCBM, as "thermally induced oligomerization" may occur.[20] The glass transitions (T<sub>g</sub>s) in Figure 4.3 have all been properly separated from the overlapping signals and all crystallization events appear in the non-reversing heat flow, as well as the majority of the melting transition. Melting transitions (especially of polymers) are typically dependent on oscillation period and amplitude[21] and its separation into reversing and non-reversing components seen here is a result of the parameters described in the Experimental Section. There is also the observation of reversible melting in many systems[22], including P3HT.[23]

From Figure 4.3, differences among the films are obvious. The spun:as cast films show two distinct crystallization exotherms at  $\sim 60$  °C and  $\sim 165$  °C while the others show only the higher temperature exotherm. Despite this, all samples exhibit two melting transitions at  $\sim 200$  °C and  $\sim 250$  °C. Spun:as cast and drop cast samples show polymer relaxation at their respective T<sub>g</sub>s which might be the result of polymer confinement at the substrate surface, but the spun:annealed samples would have had time to relax those chains during annealing and thus shows no sign of it. Though it may be simple to assign the lower temperature exotherm and endotherm to rrP3HT crystallization and melting respectively, an independent confirmation is worthwhile.

To achieve this, an X-ray analysis was performed on a spun coat BHJ film as a function of annealing temperature and is given in Figure 4.4. The film was prepared in a similar manner to those employed in TMDSC measurements but was left on the PEDOT:PSS coated substrate and annealed on a hotplate in a N<sub>2</sub> glovebox for 5 minutes at the temperatures shown in Figure 4.4. The growth of the (100) reflection of rrP3HT was used to monitor its crystallization with increasing annealing temperatures. rrP3HT crystallinity generally increases from the as cast film, which shows low

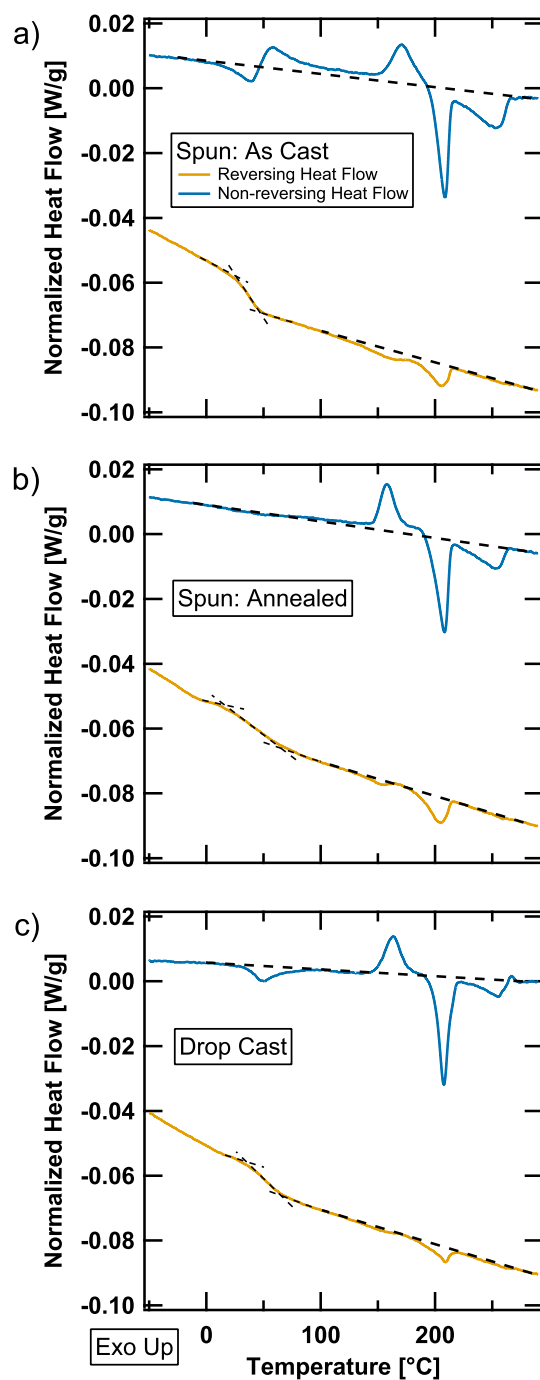


**Figure 4.3:** TMDSC thermograms of spun cast BJJ films in the as cast (a) and annealed (b) states along with a drop cast sample (c). Dashed lines illustrate baselines for used for crystallinity and  $T_g$  analyses.

**Table 4.1:** Measurements taken from the TMDSC experiments shown in Figure 4.3.

Sample	$T_g$ [°C]	$\Delta C_p$ [J/g°C]	Polymer $\Delta H_m$ [J/g]	Polymer Crystallinity* [%]
Spun: As Cast	$36.5 \pm 1.6$	$0.217 \pm 0.007$	$0.45 \pm 1.21$	$1.1 \pm 2.8$
Spun: Annealed	$40.0 \pm 2.7$	$0.248 \pm 0.021$	$13.41 \pm 0.70$	$31.3 \pm 1.7$
Drop Cast	$52.3 \pm 0.8$	$0.221 \pm 0.012$	$19.99 \pm 4.68$	$46.6 \pm 10.9$

\*Polymer Crystallinity calculated using  $\Delta H_m^\infty = 42.9$  J/g [24, see also Chap. 2]

crystallinity, up to 140 °C proving that the low temperature exotherm in the spun:as cast BHJ is indeed the cold crystallization of P3HT. Of note is the decreased intensity when annealed at 175 °C which seems to signify crystal melting. Indeed the reversing heat flow of both spun coat films show a melting onset at  $\sim 150$  °C which could be attributed to the melting of smaller crystallites that are formed during the experiment.

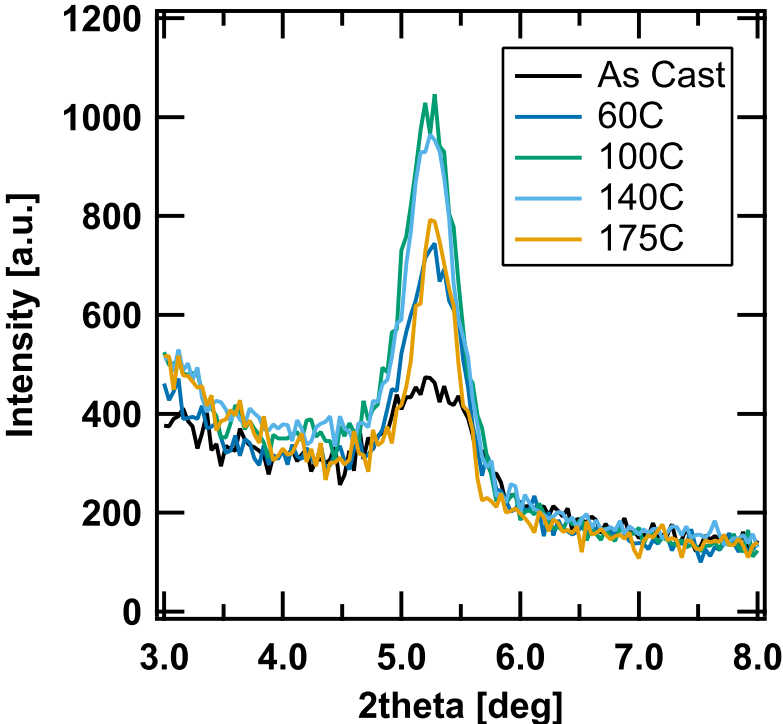


**Figure 4.4:** Grazing incidence X-ray diffraction of a BHJ film showing the (100) reflection of P3HT with different annealing temperatures. The same film was annealed for 5 minutes at each temperature. Angle of incidence was fixed at 0.4° (Rigaku Ultima IV).

It follows that the exotherm at  $\sim 165$  °C is the formation of PCBM crystallites which then melt at  $\sim 250$  °C. This makes sense since the  $T_g$  of PCBM is 130 °C[12, see App. A] and it has recently been shown that PCBM is capable of crystallizing below its  $T_g$ . [25] Optical microscopy assisted in the confirmation of PCBM crystallization as micrometer sized crystallites were seen in the BHJ after annealing at 175 °C for 10 minutes (see Figure 4.5). PCBM crystallites were neither observed before annealing

nor after annealing at 140 °C for 20 mins; the method applied to BHJ films to give the data in Figure 4.3b.

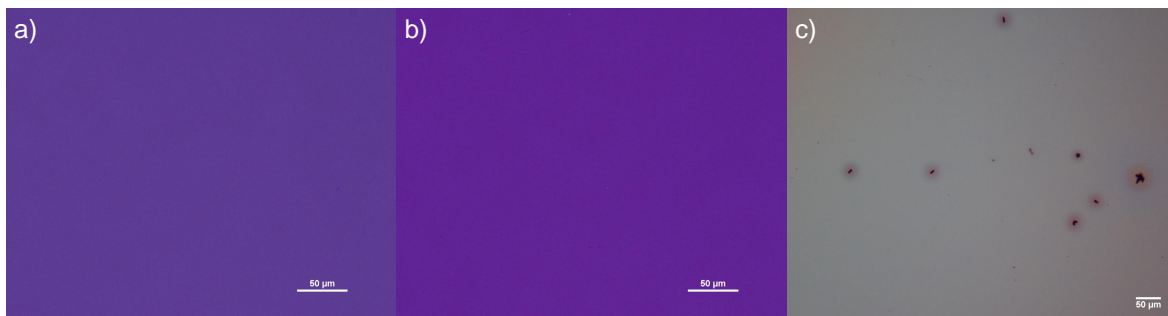


**Figure 4.5:** Optical microscopy images of BHJ films. a) As cast, b) annealed at 140 °C for 20 minutes and c) annealed at 175 °C for 10 minutes. Images taken with a Nikon Eclipse LV100 microscope equipped with a Nikon DS-Ri1 camera attachment.

With the correct assignment of the crystallization peaks and knowledge of the melting temperatures of P3HT and PCBM, crystallinity calculations can proceed. Importantly, it was noticed that the areas under the PCBM exotherm at 165 °C and the PCBM melting endotherm ( $\sim 250$  °C) were equal in magnitude for spun:as cast and annealed samples. This offers further evidence that PCBM remains amorphous after heat treatment of the BHJ. However, the drop cast film did sometimes show some excess PCBM melting energy ( $\sim 3$  J/g) which indicates a different morphology in the drop cast film. These samples however, were still treated as containing fully amorphous PCBM and the results are reported for comparative purposes only. The results of calculated P3HT crystallinity and measurements of the  $T_g$  and step change in heat capacity at  $T_g$  ( $\Delta C_p$ ) are given in Table 4.1.

Surprisingly, the spun:as cast sample has an average crystallinity close to zero. Also the measurement error (which is purely based on sample-to-sample variation) is larger than the average, which delineates that rrP3HT is completely amorphous in the BHJ thin film: a direct result of processing (i.e. spin coating). This is despite it showing a (albeit very weak) diffraction pattern in Figure 4.4. We suspect the diffraction

may be from an average random chain packing in the film. The amorphous polymer structure in the spun:as cast BHJ film is responsible for the poor performance of photovoltaic devices made in this manner due to the difference in charge mobility of amorphous versus semi-crystalline P3HT. Also noticeable in Table 4.1 is large difference in crystallinity between spun cast and drop cast samples. This again shows the difference in morphology and the large error in calculated crystallinity might imply the presence of PCBM crystallites formed during solvent evaporation as was indicated earlier.

Another important result from Table 4.1 is that the spun cast BHJ films show an increase in rrP3HT crystallinity to  $\sim 30\%$  when annealed. In Figure 4.3, it is clear that the peak previously assigned to rrP3HT crystallization has disappeared which means that the annealing step gave the polymer enough time to form and develop crystallites and there is no residual crystallization during the test. Thus, under the conditions of this experiment, 30% is possibly the highest crystallinity that rrP3HT can attain. Other experiments performed in the group have also given similar results employing 2-ethylnaphthalene as a common solvent and a rapid precipitation method.[26] Furthermore, a computational model of the BHJ was generated from neutron reflectivity (NR) and small angle neutron scattering (SANS) data obtained by Kiel et al.[1, 27] and the results reported a best fit correlating to 30% crystalline P3HT.[28] These reports all highlight a critical rrP3HT crystallinity of  $\sim 30\%$  for a 1:1 P3HT:PCBM BHJ.

### 4.3.3 $T_g$ and the Amorphous Fraction

While the above crystallinity calculations represent a major outcome of this study, it is a noticeably small fraction of the total mass of the BHJ. The amorphous content should also be analyzed to provide a complete view of the BHJ morphology determined with TMDSC. This is can be accomplished by first measuring the  $T_g$  and  $\Delta C_p$  of the spun cast films as is displayed in Table 4.1. Recall though the presence of a rigid amorphous fraction (RAF) in pure rrP3HT which exhibits its own transition.[29, see Chap. 3] Hence a closer look is required as is shown in Figure 4.6.

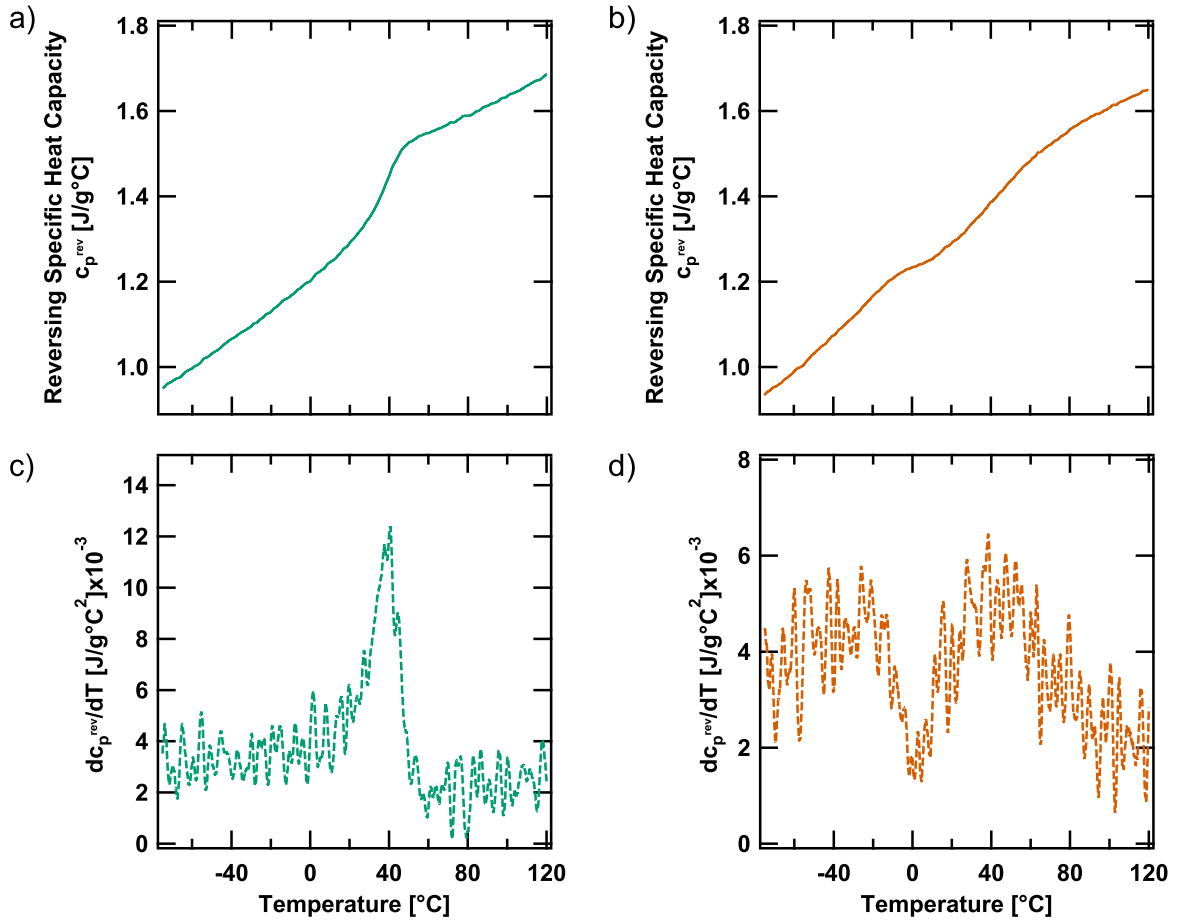


**Figure 4.6:** Reversing specific heat capacity (a,b) and the corresponding derivatives (c,d) of Spun:as cast (left column) and Spun:annealed (right column) BJJ films showing the  $T_g$  region.

The  $T_g$  region has clearly been shifted to higher temperatures for both samples which tells that the  $T_g$  observed is due to a mixture of rrP3HT and PCBM. The spun:as cast films show a single  $T_g$ , characteristic of a fully amorphous material while the annealed films show two transitions separated at 0 °C. The transitions are identified by the minimum in the derivative curve in Figure 4.6d and the transition below 0 °C was previously alluded to as a possible characteristic of semicrystalline rrP3HT,[29, see Chap. 3] confirmed by the above crystallinity calculations. For the spun:as cast BJJ films, its  $T_g$  region resembles that of a partially miscible blend with a symmetric,

singular and relatively narrow transition ( $\Delta T \approx 60$  °C).[30, see Fig.4.6c] The  $T_g$  region of the spun:annealed BHJ film shown in Figures 4.6b and d displays a very broad transition as compared to the as cast material ( $\Delta T \approx 100$  °C). This could define a system with much less miscibility (i.e. more demixing);[30] but it also could be the blending of the MAF of the BHJ with the devitrification of the rrP3HT RAF. Unfortunately, no signal from the RAF of rrP3HT can be discerned so neither can be disproved at this stage.

To begin the quantitative analysis of the amorphous phases in the the BHJ thin films, the measured  $T_g$ s were compared to the expected values based on the equation developed by Couchman:[31]

$$\ln T_g = \frac{W_{P3HT}\Delta C_{p,P3HT} \ln T_{g,P3HT} + W_{PCBM}\Delta C_{p,PCBM} \ln T_{g,PCBM}}{W_{P3HT}\Delta C_{p,P3HT} + W_{PCBM}\Delta C_{p,PCBM}} \quad (4.1)$$

$$T_{g,P3HT} = 15^\circ C \ (288K), \ \Delta C_{p,P3HT} = 0.32 \ J/g^\circ C \ [29]$$

$$T_{g,PCBM} = 130^\circ C \ (403K), \ \Delta C_{p,PCBM} = 0.11 \ J/g^\circ C \ [see \ Appendix \ A]$$

$W$  is the mass fraction of the respective component noted in the subscript. Note also that  $W_{P3HT} + W_{PCBM} = 1$  meaning that the mass fractions are normalized to the part of the sample exhibiting the  $T_g$ , which (especially in this case) may not be the entire sample. Equation 4.1 is preferred to the simpler Fox equation since the requirement  $T_{g,P3HT}\Delta C_{p,P3HT} \approx T_{g,PCBM}\Delta C_{p,PCBM}$  is not satisfied.[31, 32] Expected values of the BHJ  $T_g$  are calculated by assuming the total amorphous fraction (i.e. everything that is not crystalline) contributes to the resulting  $T_g$  and are displayed as hollow squares in Figure 4.7. Equation 4.1 was also used to calculate the actual  $W_{PCBM}$  according to the measured BHJ  $T_g$ . Those results are displayed as filled squares in Figure 4.7. It is evident that the expected values overestimate reality, even in the drop cast films. Since PCBM has the higher  $T_g$ , Equation 4.1 is overestimating the  $W_{PCBM}$  present in the mixed phase responsible for the observed  $T_g$ . This suggests some of the PCBM is

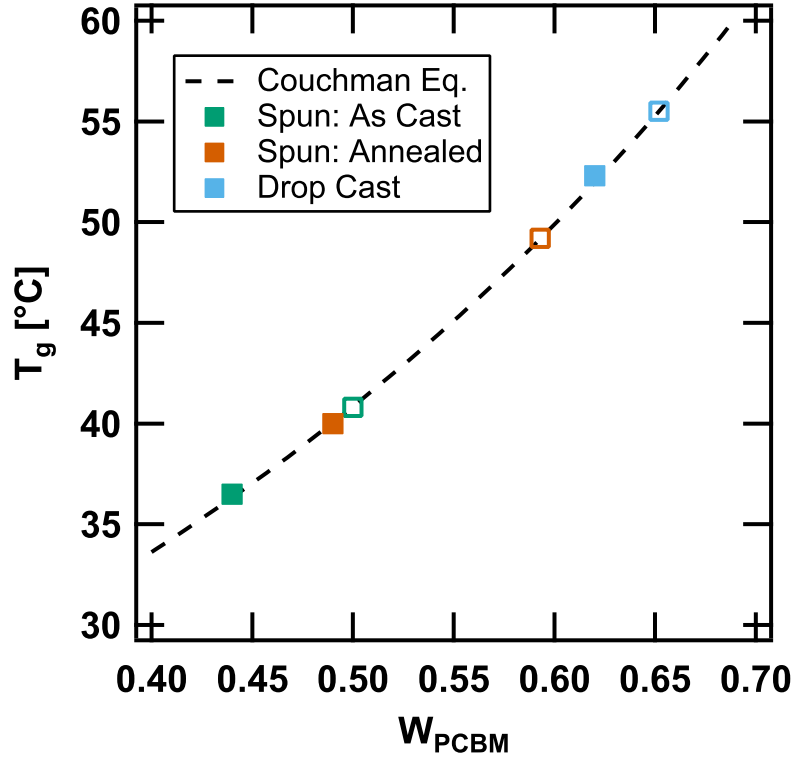


**Figure 4.7:** Graph of glass transition ( $T_g$ ) vs. PCBM mass fraction ( $W_{PCBM}$ ). Shown are the  $T_g$ s of the measured samples (filled squares) mapped onto the theoretical trendline and calculated values (open squares) based on the total amorphous fraction in the respective samples. Trendline is from Eq. 4.1 and the filled symbols were used in Table 4.2.

confined and therefore does not participate in the  $T_g$ ; lowering it from the predicted value.

Figure 4.7 however shows that the mixed phase contains 45% and 49% PCBM in the spun:as cast and annealed BHJs respectively. It is expected that this PCBM is mixed with the mobile amorphous fraction (MAF) of rrP3HT – assuming that a rrP3HT RAF exists and does not mix with PCBM – and that the remainder is agglomerated.

Thus far, TMDSC analysis has led to the quantification of rrP3HT crystalline fraction and the mass fraction of PCBM mixed into rrP3HT MAF. Two other material fractions need to be accounted for; the RAF of rrP3HT and agglomerated PCBM. If

a RAF exists for the polymer, then more information is needed in order to quantify it; namely the agglomerated PCBM fraction. The following section describes how scattering provides the final piece of the puzzle.

#### 4.3.4 Combination of SANS and MDSC for RAF Calculation

It is well known that SANS experiments on BHJs employ two phase models for data fitting because of the lack of contrast between crystalline and amorphous rrP3HT phases as described in the introduction to this chapter. Thus only PCBM aggregates within a "mixed" phase can be distinguished. On the other hand, TMDSC has just proven capable of identifying crystalline P3HT and a "mixed" phase of amorphous rrP3HT and PCBM, with some indication of PCBM agglomerates. Hence it is proposed that by combining the strengths of these characterization methods, the identification of all polymer and nanoparticle phases (and quantities thereof) may be possible. This tag-team approach will shed light on the ambiguous "mixed" phase present in both analyses.

To perform the calculations we assume the following four phases (or fractions) are present in the rrP3HT:PCBM BHJ:

1. Crystalline rrP3HT fraction ( $W_{P3HT}^{cryst}$ ) measured by TMDSC (see Table 4.1).
2. PCBM agglomerate fraction ( $\phi_{PCBM}^{agg}$ ) measured by SANS. Data is taken from the Ph.D. thesis of Hao Shen.[3]
3. A mixed fraction comprising rrP3HT MAF ( $W_{P3HT}^{maf}$ ) and PCBM ( $W_{PCBM}^{maf}$ ) of which  $W_{PCBM}^{maf}$  is calculated from BHJ  $T_g$  data and Equation 4.1.
4. RAF of rrP3HT ( $W_{P3HT}^{raf}$ ) which does not contain any PCBM.

where  $W$  and  $\phi$  are the mass and volume fractions of the materials in the subscript respectively. The superscript specifies phase. Conservation of mass requires:

$$M_{P3HT} = M_{P3HT}^{cryst} + M_{P3HT}^{maf} + M_{P3HT}^{raf} \quad (4.3a)$$

$$M_{PCBM} = M_{PCBM}^{agg} + M_{PCBM}^{maf} \quad (4.3b)$$

$$\text{and } \dots M_{P3HT} = M_{PCBM} \text{ (initial condition)} \quad (4.3c)$$

where  $M$  is mass in grams. Equations 4.3a and 4.3b would be identical in terms of  $\phi$  as well. Equation 4.3c is due to the concentration of rrP3HT and PCBM in the solution used to make the films. Also for this mathematical treatment the densities of rrP3HT ( $\rho_{P3HT}$ ) and PCBM ( $\rho_{PCBM}$ ) were 1.15 g/cm<sup>3</sup> and 1.3 g/cm<sup>3</sup>, respectively, in accordance with the SANS data[3] and are used for conversions to and from  $\phi$  given by (for example):

$$\phi_{PCBM}^{agg} = \frac{M_{PCBM}^{agg} / \rho_{PCBM}}{M_{PCBM} / \rho_{PCBM} + M_{P3HT} / \rho_{P3HT}} \quad (4.4)$$

Changes in  $\rho_{P3HT}$  or  $\rho_{PCBM}$  do not affect the trends and comparisons derived from the outcome of these calculations.

A summary of the results is given in Table 4.2 and some intriguing observations can be made. At first glance, the measured  $T_g$ s for the BHJ films suggest an increase in PCBM content in the MAF when the films are thermally annealed (see Fig. 4.7). Table 4.2 suggests that it is the dramatic decrease in rrP3HT concentration due to crystallization that shifts the  $T_g$  to a higher temperature. Actually, the  $\Delta C_p$  measurements of the blended films shown in Table 4.1 agree with this conclusion (i.e. higher  $\Delta C_p$  means higher rrP3HT concentration), implying that  $\Delta C_p$  may be a more sensitive indicator of material mixing in this system.

Reported here for the first time are values of the RAF of rrP3HT in BHJ thin films. The spun:as cast BHJ contains 30 vol.% RAF corresponding to 57 vol.% of rrP3HT. This large RAF is likely a result of the kinetic trapping and centrifugal forces of spin coating,[33] as well as the intermolecular interactions between rrP3HT and PCBM. The RAF may also contain areas of weak, short range order[34] which could explain why a weak diffraction signal was still detected (see Fig. 4.4). With thermal annealing, rrP3HT crystallizes and the RAF decreases. Possibly, the RAF facilitated rrP3HT crystallization by being free of PCBM molecules, offering phase pure sites for nucleation. However, the spun:annealed BHJ still contains a substantial amount of RAF (23 vol.%, 43 vol.% of rrP3HT) which means that the film fabrication process likely has lasting effects on its properties. The spun:annealed film has approximately

**Table 4.2:** Measured and calculated BHJ phases from TMDSC and SANS

BHJ Sample	$\phi_{P3HT}^{crys}$ ( $W_{P3HT}^{crys}$ )	$\phi_{PCBM}^{agg}$ ( $W_{PCBM}^{agg}$ )	Mixed Fraction (MAF)		$\phi_{P3HT}^{raf}$ ( $W_{P3HT}^{raf}$ )	Sum
			$\phi_{P3HT}^{maf}$ ( $W_{P3HT}^{maf}$ )	$\phi_{PCBM}^{maf}$ ( $W_{PCBM}^{maf}$ )		
Spun: As Cast	0.00 (0.00)	0.31 (0.33)	0.23 (0.22)	0.16 (0.17)	0.30 (0.28)	1.00 (1.00)
Spun: Annealed	0.17 (0.16)	0.36 (0.38)	0.13 (0.12)	0.11 (0.12)	0.23 (0.22)	1.00 (1.00)

twice the RAF of pure rrP3HT films (see Chapter 3) which underscores the influence of PCBM on the morphology of the polymer and the entire BHJ film by extension.

#### 4.4 Conclusion

TMDSC has proven an essential tool in the characterization of rrP3HT:PCBM BHJs. By preparing and testing thin films of the polymer:fullerene blend, the morphology of rrP3HT can be quantified. It was discovered that as cast films do not contain any crystalline regions which explains the poor device performance from these films. Annealing causes rrP3HT to crystallize to 30% and it was postulated that this may be the maximum crystallinity achievable under the experimental conditions defined in this work. An improved, four phase model was introduced in this chapter to fully capture the BHJ morphology. A combined analytical approach using both TMDSC and SANS revealed that large polymer RAFs exist in both as cast and annealed thin films that does not contain PCBM. The RAF is formed during spin coating and from the intermolecular interactions with PCBM. It is also significantly larger than the RAF found in pure rrP3HT thin films examined in the previous chapter. Hence BHJ characterization using TMDSC and SANS enables quantification and tracking of changes in all possible polymer and fullerene phases due to film fabrication and post processing. Knowing the significant RAF present in BHJ thin films may spur investigations of its role in the photovoltaic performance of polymer:fullerene solar devices.

## BIBLIOGRAPHY

- [1] Jonathon Kiel, Aaron Eberle, and Michael Mackay. Nanoparticle Agglomeration in Polymer-Based Solar Cells. *Phys. Rev. Lett.*, 105(16):1–4, oct 2010.
- [2] Brett W. Guralnick. *Plastic Solar Cell Interface and Morphological Characterization*. PhD thesis, University of Delaware, 2012.
- [3] Hao Shen. *Morphology Control in Semiconducting Polymer-Nanoparticle Mixtures for use in Photovoltaics*. PhD thesis, University of Delaware, 2015.
- [4] Wenluan Zhang. *Morphology Control of Polymer:Fullerene Solar Cells by Nanoparticle Self-Assembly*. PhD thesis, University of Delaware, 2016.
- [5] Xiaoni Yang, Joachim Loos, Sjoerd C Veenstra, Wiljan J H Verhees, Martijn M Wienk, Jan M Kroon, Matthias A J Michels, and René A J Janssen. Nanoscale morphology of high-performance polymer solar cells. *Nano Lett.*, 5(4):579–83, apr 2005.
- [6] Svetlana S. van Bavel, Maik Bärenklau, Gijsbertus de With, Harald Hoppe, and Joachim Loos. P3HT/PCBM Bulk Heterojunction Solar Cells: Impact of Blend Composition and 3D Morphology on Device Performance. *Adv. Funct. Mater.*, 20(9):1458–1463, apr 2010.
- [7] Hsueh-Chung Liao, Cheng-Si Tsao, Tsung-Han Lin, Chih-Min Chuang, Charn-Ying Chen, U-Ser Jeng, Chiu-Hun Su, Yang-Fang Chen, and Wei-Fang Su. Quantitative nanoorganized structural evolution for a high efficiency bulk heterojunction polymer solar cell. *J. Am. Chem. Soc.*, 133(33):13064–73, aug 2011.
- [8] Yue Zhao, Guoxiong Yuan, Philippe Roche, and Mario Leclerc. A calorimetric study of the phase transitions in poly(3-hexylthiophene). *Polymer*, 36(11):2211–2214, jan 1995.

- [9] Trinh Tung Ngo, Duc Nghia Nguyen, and Van Tuyen Nguyen. Glass transition of PCBM, P3HT and their blends in quenched state. *Adv. Nat. Sci. Nanosci. Nanotechnol.*, 3(4):045001, sep 2012.
- [10] Jung Yong Kim and C. Daniel Frisbie. Correlation of Phase Behavior and Charge Transport in Conjugated Polymer/Fullerene Blends. *J. Phys. Chem. C*, 112(45):17726–17736, nov 2008.
- [11] Christian Müller, Toby A. M. Ferenczi, Mariano Campoy-Quiles, Jarvist M. Frost, Donal D. C. Bradley, Paul Smith, Natalie Stingelin-Stutzmann, and Jenny Nelson. Binary Organic Photovoltaic Blends: A Simple Rationale for Optimum Compositions. *Adv. Mater.*, 20(18):3510–3515, aug 2008.
- [12] Jun Zhao, Ann Swinnen, Guy Van Assche, Jean Manca, Dirk Vanderzande, and Bruno Van Mele. Phase diagram of P3HT/PCBM blends and its implication for the stability of morphology. *J. Phys. Chem. B*, 113(6):1587–91, feb 2009.
- [13] Jun Zhao, Sabine Bertho, Joke Vandenberghe, Guy Van Assche, Jean Manca, Dirk Vanderzande, Xiaoqing Yin, Jingdan Shi, Thomas Cleij, Laurence Lutsen, Bruno Van Mele, Guy Van Assche, and Bruno Van Mele. Phase behavior of PCBM blends with different conjugated polymers. *Phys. Chem. Chem. Phys.*, 13(26):12285–92, jul 2011.
- [14] Fiona C. Jamieson, Ester Buchaca Domingo, Thomas McCarthy-Ward, Martin Heeney, Natalie Stingelin, and James R. Durrant. Fullerene crystallisation as a key driver of charge separation in polymer/fullerene bulk heterojunction solar cells. *Chem. Sci.*, 3(2):485, jan 2012.
- [15] David M. Huang, Scott A. Mauger, Stephan Friedrich, Simon J. George, Daniela Dumitriu-LaGrange, Sook Yoon, and Adam J. Moulé. The Consequences of Interface Mixing on Organic Photovoltaic Device Characteristics. *Adv. Funct. Mater.*, 21(9):1657–1665, may 2011.

- [16] BW Guralnick, BJ Kirby, C F Majkrzak, and M E Mackay. Morphological characterization of plastic solar cells using polarized neutron reflectivity. *Appl. Phys. Lett.*, 102:083305, 2013.
- [17] Zheng Xu, Li-Min Chen, Guanwen Yang, Chun-Hao Huang, Jianhui Hou, Yue Wu, Gang Li, Chain-Shu Hsu, and Yang Yang. Vertical Phase Separation in Poly(3-hexylthiophene): Fullerene Derivative Blends and its Advantage for Inverted Structure Solar Cells. *Adv. Funct. Mater.*, 19(8):1227–1234, apr 2009.
- [18] G Greczynski, Th Kugler, and W.R Salaneck. Characterization of the PEDOT-PSS system by means of X-ray and ultraviolet photoelectron spectroscopy. *Thin Solid Films*, 354(1-2):129–135, oct 1999.
- [19] Jian Zhou, Dalaver H. Anjum, Long Chen, Xuezhu Xu, Isaac Aguilar Ventura, Long Jiang, and Gilles Lubineau. The temperature-dependent microstructure of PEDOT/PSS films: insights from morphological, mechanical and electrical analyses. *J. Mater. Chem. C*, 2(46):9903–9910, sep 2014.
- [20] Deborah Leman, Mary Allison Kelly, Stuart Ness, Sebastian Engmann, Andrew Herzing, Chad Snyder, Hyun Wook Ro, R. Joseph Kline, Dean M. DeLongchamp, and Lee J. Richter. In situ characterization of polymer-fullerene bilayer stability. *Macromolecules*, 48(2):383–392, jan 2015.
- [21] P. S. Gill, S. R. Sauerbrunn, and M. Reading. Modulated differential scanning calorimetry. *J. Therm. Anal.*, 40(3):931–939, feb 1993.
- [22] B Wunderlich. Reversible crystallization and the rigid-amorphous phase in semicrystalline macromolecules. *Prog. Polym. Sci.*, 28:383–450, 2003.
- [23] Chad R. Snyder, R. Joseph Kline, Dean M. DeLongchamp, Ryan C. Nieuwendaal, Lee J. Richter, Martin Heeney, and Iain McCulloch. Classification of semiconducting polymeric mesophases to optimize device postprocessing. *J. Polym. Sci. Part B Polym. Phys.*, pages n/a–n/a, aug 2015.

- [24] Roddel Remy, Emily Daniels Weiss, Ngoc A. Nguyen, Sujun Wei, Luis M. Campos, Tomasz Kowalewski, and Michael E. Mackay. Enthalpy of fusion of poly(3-hexylthiophene) by differential scanning calorimetry. *J. Polym. Sci. Part B Polym. Phys.*, 52(22):1469–1475, nov 2014.
- [25] Niko Van den Brande, Guy Van Assche, and Bruno Van Mele. Isothermal Crystallization of PC 61 BM in Thin Layers Far below the Glass Transition Temperature. *Cryst. Growth Des.*, page 151014090453004, oct 2015.
- [26] Ngoc A. Nguyen. *Flow Induced/ Refined Solution Crystallization of a Semiconducting Polymer*. PhD thesis, University of Delaware, 2016.
- [27] Jonathan W. Kiel, Brian J. Kirby, Charles F. Majkrzak, Brian B. Maranville, and Michael E. Mackay. Nanoparticle concentration profile in polymer-based solar cells. *Soft Matter*, 6(3):641–646, 2010.
- [28] Daniel P. Olds, Phillip M. Duxbury, Jonathan W. Kiel, and Michael E. Mackay. Percolating bulk heterostructures from neutron reflectometry and small-angle scattering data. *Phys. Rev. E*, 86(6):061803, dec 2012.
- [29] Roddel Remy, Sujun Wei, Luis M. Campos, and Michael E. Mackay. Three-Phase Morphology of Semicrystalline Polymer Semiconductors: A Quantitative Analysis. *ACS Macro Lett.*, 4(9):1051–1055, sep 2015.
- [30] Mike Reading and Douglas J Hourston, editors. *Modulated Temperature Differential Scanning Calorimetry: Theoretical and Practical Applications in Polymer Characterisation*. Springer, 2006.
- [31] P. R. Couchman. Compositional Variation of Glass-Transition Temperatures. 2. Application of the Thermodynamic Theory to Compatible Polymer Blends. *Macromolecules*, 11(6):1156–1161, nov 1978.
- [32] Paul C Hiemenz and Timothy P Lodge. *Polymer Chemistry*. CRC Press, 2nd edition, 2007.

- [33] Shadid Askar, Christopher M. Evans, and John M. Torkelson. Residual stress relaxation and stiffness in spin-coated polymer films: Characterization by ellipsometry and fluorescence. *Polymer*, 76:113–122, oct 2015.
- [34] Xiaobo Shen, Weiguo Hu, and Thomas P. Russell. Measuring the Degree of Crystallinity in Semicrystalline Regioregular Poly(3-hexylthiophene). *Macromolecules*, 49(12):4501–4509, jun 2016.

## Chapter 5

### INVESTIGATION OF INTERFACIAL PCBM DIFFUSION BY NEUTRON REFLECTIVITY

#### 5.1 Introduction

Neutron scattering techniques have proven vital to the polymer solar cell community. It has allowed researchers to peer into the vertical compositional profile of bulk heterojunction (BHJ) thin films with sub-nm precision. Ever since the first papers on neutron reflectivity (NR) of P3HT:PCBM BHJs were published though, there has been discord in the results obtained.[1, 2] Kiel et al. employed phase sensitive NR and described the BHJ as consisting of a mixed P3HT:PCBM phase in the center of the thin film with high concentrations of PCBM at the substrate and air interfaces.[3] Parnell et al. observed high PCBM concentrations at the substrate but depleted PCBM at the air interface, of which some was recovered on annealing.[2]

In this chapter we revisit NR and address the issue of PCBM diffusion from a different perspective. This study will now focus on its mixing with PEDOT:PSS to obtain maximum possible concentrations that can exist in this layer. Bilayer structures are the simplest way to observe diffusive phenomenon via NR since the materials are initially separate and are then allowed to diffuse by thermal annealing procedures. Thus it is used here to observe the mixing of individual BHJ materials with PEDOT:PSS to understand the changes that occur at that interface. Due to the simplicity of the study and the distinct differences in scattering length density of the materials used, phase sensitive or polarized NR is unnecessary.

## 5.2 Experimental

All samples were prepared on 3" diameter silicon substrates that were cleaved from an ingot on the (111) face. The substrates were cleaned by rinsing with soapy water, deionized water, acetone and isopropyl alcohol. They were finally prepared by UV-ozone treatment for 30 minutes.

PEDOT:PSS (Clevios AL 4083) was spun coat on all samples at 3000 rpm then annealed at 130 °C for 15 minutes to create 40 nm thick films. To create bilayers, regioregular P3HT (Luminescence Technologies Corp) or PCBM (Nano-C) were spun coat on top of the PEDOT:PSS layer from chlorobenzene solutions at 2500 rpm for 1 minute. The P3HT solution concentration was 15 mg/mL while the PCBM solution was 30 mg/mL. Initial thicknesses were 69 nm and 75 nm for P3HT and PCBM respectively. These were used as initial inputs for fitting of reflectivity profiles. Thermal annealing was performed at 140 °C for 20 minutes unless otherwise told. A vacuum oven with a constant flow of nitrogen was used for annealing to prevent sample degradation and to ensure all solvent is evaporated.[4] The same specimen was tested in "As Cast" and "Annealed" states so direct comparisons can be made.

Neutron reflectivity was carried out on the Polarized Beam Reflectometer (PBR) on the NG-D beamline at the National Institute for Standards and Technology (NIST) Center for Neutron Research (NCNR). The 4.75 Å monochromatic beam was used in standard mode (unpolarized).

Reflectivity fitting was done using Refl1D software[5] that was uploaded onto the University of Delaware's Venus computing cluster. Multiple nodes were used simultaneously — depending on availability — to shorten overall computing time. A DREAM[6] fitting algorithm was used that involves a Markov Chain Monte Carlo uncertainty analysis, as was previously applied to polarized neutron reflectivity of similar systems.[7] Pure PEDOT:PSS and its bilayers with P3HT and PCBM were fitted by assigning each layer to a *slab* defined by a thickness ( $z$ ), neutron scattering length density ( $\rho$ ) and interfacial roughness. Best fit profiles determined by the lowest  $\chi^2$  error are presented in this chapter.

Interlayer mixing was calculated by measuring the volume fraction ( $\phi$ ) of the diffusing component using the relation

$$\phi_j = \frac{\rho(z) - \rho_i}{\rho_j - \rho_i} \quad (5.1)$$

where  $\rho$  is SLD and  $i$  and  $j$  represent the major (matrix) and minor (diffused) components at a thickness ( $z$ ) in the film. The initial  $\rho$  for the respective components are given in Table 5.1 below. These values were allowed to float (within sensible limits) during the fitting procedure. The  $\rho$  for the silicon substrate and natural oxide layer were fixed at  $2.07$  and  $3.49 \times 10^{-6} \text{ \AA}^{-2}$  respectively.

**Table 5.1:** Table of initial  $\rho$  for each examined component.

	Bulk PEDOT:PSS	PSS-rich	P3HT	PCBM
$\rho (\times 10^{-6} \text{ \AA}^{-2})$	1.8	1.6	0.7	3.6

## 5.3 Results and Discussion

### 5.3.1 PEDOT:PSS Layer Modeling

To begin this study it is essential to know the general morphology of a single PEDOT:PSS thin film. Hence an abbreviated NR profile was obtained and is shown in Figure 5.1. Annealing of the pure PEDOT:PSS film was done to observe any changes that may effect the investigation of bilayers that will be examined next.

The best fit for this profile corresponded to a two slab model of which the top layer is thin and of a lower SLD than the rest of the film. The ratio of PEDOT to PSS in this formula is 1:6 according to the supplier. Therefore, the excess PSS phase separates and forms an almost pure layer on the surface of the film. PSS surface segregation has been previously observed via photoelectron spectroscopy,[8–11] scanning-tunneling microscopy[12, 13] and reflectivity[14–16] experiments. In fact, much research has gone into understanding[17–20] and modifying[15, 21–24] the morphology of PEDOT:PSS thin films to increase conductivity for electronic applications.

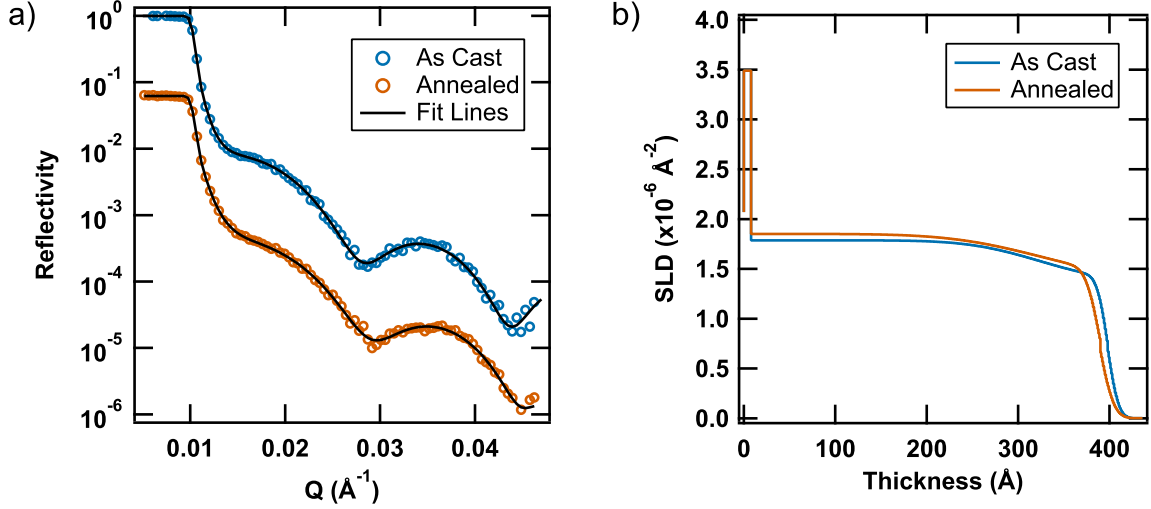


**Figure 5.1:** Reflectivity (a) and SLD (b) profiles of a pure PEDOT:PSS film before and after annealing. Data in (a) were shifted vertically for clarity.

Interpretation of the literature places the natural PSS-rich layer thickness at 4 – 15 nm depending on initial PEDOT to PSS ratio and thermal treatment conditions, although no clear trend for the latter is observed.[9, 11, 14–16] The data presented here is in agreement with the literature and even displays a similar gradual transition to the bulk PEDOT:PSS concentration as you go deeper into the film. Interestingly, these observations were possible without deuterating PSS.[14, 15] In addition, there is a 3.6% increase in the SLD as well as some film shrinkage of the annealed sample compared to as cast. These changes can be attributed to atmospheric water uptake by hydrophilic PSS during sample transport.[25, 26] This water was quickly eliminated on annealing while the general film morphology remained unchanged. With this fundamental knowledge, an analysis of the diffusion of other materials into the PEDOT:PSS layer can proceed.

### 5.3.2 P3HT/PEDOT:PSS bilayer

Figure 5.2 displays the reflectivity fit and SLD profile of a P3HT/PEDOT:PSS bilayer sample. A three slab model was the best fit for this sample which implies

that the bulk PEDOT:PSS, PSS-rich and pure P3HT layers can all be distinguished in the profile. Since the SLD of P3HT is lower than that of PEDOT:PSS, diffusion on annealing would therefore result in a reduction of the PEDOT:PSS SLD and perhaps an alteration of the film morphology as well.

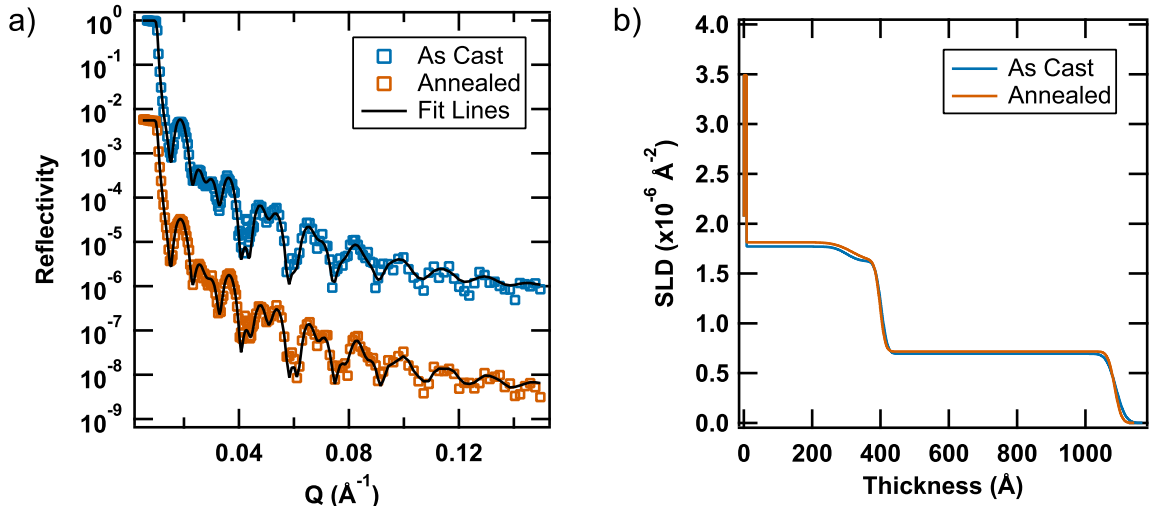


**Figure 5.2:** Reflectivity (a) and SLD (b) profiles of a PEDOT:PSS/P3HT bilayer before and after annealing. Data in (a) were shifted vertically for clarity.

However, something different occurred. Annealing has increased the SLD of PEDOT:PSS by 2.4% and left the P3HT layer virtually unchanged. It is believed the SLD increase was caused by the same process noted in the previous section, albeit with reduced effect since P3HT is hydrophobic and will serve as a water barrier for the PEDOT:PSS sub layer with possible exception of the film edges. Thus the water desorption from PEDOT:PSS on annealing is the only noticeable change in this experiment. This directly shows that the polymers are immiscible.

Huang et al.[27] showed that P3HT and the PSS-rich layer physically mix, then undergo a red-ox reaction creating  $\text{P3HT}^+$  and  $\text{PSS}^-$  species during annealing. While this work does not dispute the possibility of a chemical reaction, there are a few differences between the two studies that must be mentioned. First, their study seems to have only fitted the reflectivity data to a single slab model that, as illustrated in the

previous section, is not sufficient to properly describe the PEDOT:PSS layer. Thus physical mixing can not be directly proven from that analysis. It is shown here that no discernible change in SLD or interfacial roughness occurred after annealing which proves P3HT does not diffuse into the PSS-rich layer.

Second, the red-ox reaction seems to only play a role at annealing temperatures of  $\geq 150$  °C; so it should have minimal effect on this data. Even if the reaction occurred in the sample shown in Figure 5.2, the former point suggests that it would only be at monolayer distances from the interface and no further. Moreover, the products of the red-ox reaction could attract each other (electrostatically) and remain at the interface, potentially blocking any diffusion across the boundary: a scenario akin to interfacial polymerization.

### 5.3.3 PCBM/PEDOT:PSS bilayer

Switching to the electron acceptor component of the bulk heterojunction, a PCBM/PEDOT:PSS bilayer was examined and the results are displayed in Figure 5.3. In contrast to P3HT, PCBM has a higher SLD than PEDOT:PSS since it contains much less hydrogen atoms in its chemical structure. If PCBM were to diffuse into PEDOT:PSS, an increase in PEDOT:PSS SLD should occur after annealing beyond what was observed in the pure film.

The first direct observation from Figure 5.3b is the change in the PCBM top layer with annealing. There is a reduction in SLD by 5% and a 10 Å thinning of the layer as well. It is worthwhile to mention that annealing was performed at a temperature above the glass transition of PCBM ( $T_g \sim 130$  °C)[28] so crystallization should occur and is an inevitable part of the annealed morphology, although it was not directly measured here. There are two distinct differences in the PEDOT:PSS layer before and after annealing with a PCBM overlayer. A 4.8% total increase in the SLD of PEDOT:PSS is observed, which is larger than what was measured in the pure material but similar in magnitude to the reduction in PCBM SLD. Importantly, the PSS-rich layer seen in the two previous samples is absent in both as cast and annealed tests.

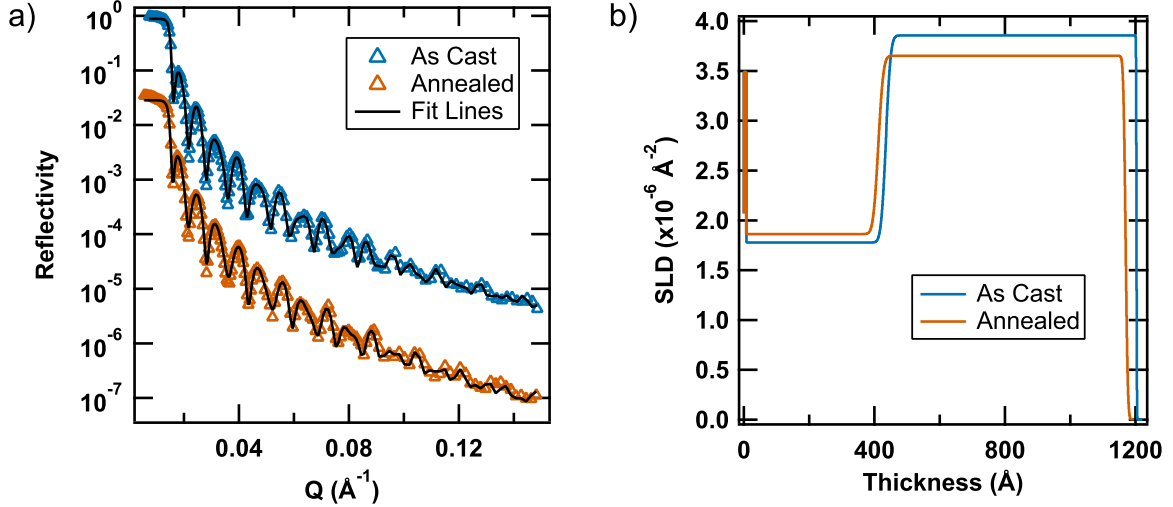


**Figure 5.3:** Reflectivity (a) and SLD (b) profiles of a PEDOT:PSS/PCBM bilayer before and after annealing. Data in (a) was shifted vertically for clarity.

In fact, a lower  $\chi^2$  error was obtained by fitting both datasets to a two slab model as opposed to three slabs used for PEDOT:PSS/P3HT. Based on these observations, two possible scenarios might lead to this result:

1. There was no interlayer mixing and the changes are a result of individual processes taking place in each layer. Also the fitting procedure could not accurately identify the PSS-rich region.
2. PCBM has mixed with PEDOT:PSS, especially the PSS-rich layer, raising its SLD and lowering the SLD and thickness of the PCBM film.

The first point cannot be immediately dismissed since previous reports have modeled PEDOT:PSS as a single layer despite knowledge of PSS segregation.[27, 29, 30] This speaks to the difficulty in identifying the PSS-rich layer, especially when sandwiched between thicker bulk PEDOT:PSS and other polymer layers. Also, the one-to-many mapping of standard reflectivity adds to the challenge of finding the right profile. Furthermore, PCBM is known to contain solvent in its crystal phase[31] so it holds that the amorphous phase traps solvent as well. Annealing will then promote solvent diffusion causing film shrinkage and SLD reduction; if the solvent has a higher SLD than PCBM. Using a liquid density of  $1.1 \text{ g/cm}^3$ , the SLD for chlorobenzene is 1.8

$\times 10^{-6} \text{ \AA}^{-2}$  as given by the NIST scattering calculator.[32] This means that the first scenario is false since evaporation of chlorobenzene from the film stack upon would lead to an increase in PCBM SLD: the opposite of what is observed.

To the second point, PCBM mixing with PEDOT:PSS has been observed before but the distinction between bulk PEDOT:PSS and the PSS-rich layer was not made.[7, 33] Therefore the results of this experiment may specify PCBM’s preference for mixing with PSS. The outcome of the  $\phi_{PCBM}$  calculation from Equation 5.1 in the PSS-rich layer as well as the bulk PEDOT:PSS layer is presented in Table 5.2. The values  $1.8 \times 10^{-6} \text{ \AA}^{-2}$  and  $1.6 \times 10^{-6} \text{ \AA}^{-2}$  were used for bulk PEDOT:PSS and PSS-rich layers respectively based on the fitting result of PEDOT:PSS/P3HT bilayer (see explanation in following section). These agree with SLD calculations from the NIST scattering calculator using a material density of  $1.1 \text{ g/cm}^3$  for both layers.[18] The assumption is made that the PSS-rich layer exists both before and after annealing, regardless of PCBM diffusion and SLD only changes due to PCBM mixing. This is reasonable given the results presented in the previous sections.

**Table 5.2:** Calculated  $\phi_{PCBM}$  contained in PEDOT:PSS layer.

	As Cast	Annealed
Bulk PEDOT:PSS	-1.1%	3.1%
PSS-rich	7.9%	11.7%

The negative result from the as cast bulk PEDOT:PSS phase suggests no PCBM has mixed into that layer and the small change is within experimental error. Interestingly, the PSS-rich layer has been clearly altered due to the diffusion of PCBM even in the as cast state. This would agree with the findings of Guralnick et al.[7] and highlight the preference for PCBM in the PSS-rich phase. In accordance with that study, it is necessary to perform an uncertainty analysis to confirm the extent of this phenomenon.

### 5.3.4 Analysis of Diffusion into PEDOT:PSS

The bar charts in Figures 5.4 and 5.5 compare the SLDs of bulk PEDOT:PSS and PSS-rich layers measured from all three experiments discussed above (note the difference in scale). SLDs for the PCBM/PEDOT:PSS bilayer are identical in both graphs since only one slab was used to fit both layers as explained before. Figure 5.4 illustrates that the bulk PEDOT:PSS layer underwent minor changes during the experiment but the calculated error does indicate that these changes may be real and the difference between as cast and annealed films may just be due to water evaporation as was suggested earlier. In general PCBM does not affect the morphology of the bulk PEDOT:PSS layer.

In contrast to the bulk, the PSS-rich layer is more significantly affected by the presence of PCBM as shown in Figure 5.5. First, the uncertainty in the PSS-rich layer of the pure PEDOT:PSS thin film is quite large. It is even relatively large in the P3HT/PEDOT:PSS bilayer film as compared to bulk PEDOT:PSS. We attribute this to the fact that the PSS-rich layer is not well defined, rather it is a layer with increasing PEDOT content (and therefore SLD) from the surface to bulk PEDOT:PSS.[11, 14, 15] This concentration gradient makes it difficult to define the region as a slab, generating larger errors in the process.

With regard to the pure PEDOT:PSS film, it is believed that the fit accuracy also suffered from the narrow data range collected; making the PSS-rich region even more challenging to decipher. Hence more accurate values of PEDOT:PSS SLD were taken from the P3HT/PEDOT:PSS bilayer and used to produce Table 5.2 above.

Despite these inaccuracies, there is still a distinct difference between the PSS-rich regions with PCBM versus the other films and between as cast and annealed films. This comparison aids in the confirmation of PCBM diffusion into the PSS-rich surface layer of PEDOT:PSS to a maximum of 12% calculated by Equation 5.1 after annealing. Importantly, findings herein also suggest diffusion without thermal annealing, albeit to a lesser extent. What mechanism would cause this to occur?

It is apparent that PCBM has some solubility in PSS, but not PEDOT, since

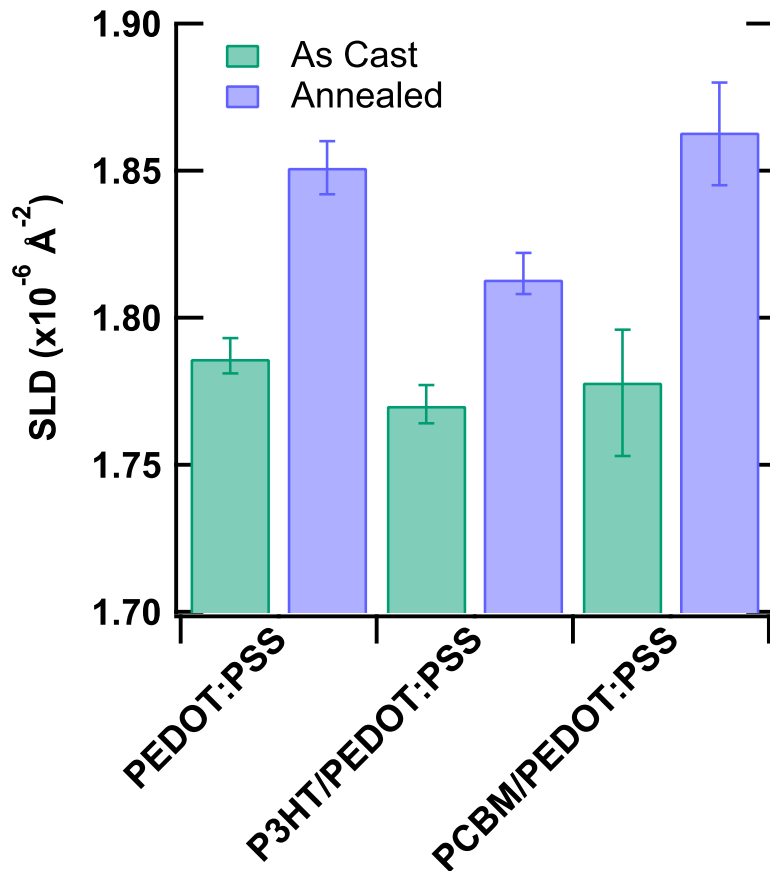


**Figure 5.4:** Chart showing bulk PEDOT:PSS SLD in the pure and bilayer samples. Error bars represent 95% confidence interval calculated during the fitting procedure.

it did not diffuse into the region with the highest PEDOT content (i.e. the bulk PEDOT:PSS layer). In the as cast state however, PCBM is well below its  $T_g$  and reported  $T_g$ s for PSS reach as high as 160 °C.[34] The only way for PCBM to diffuse in that case would be if PSS was swollen by chlorobenzene used to deposit the PCBM film. Consequently, a swelling experiment was done by placing a PEDOT:PSS thin film (coated on a Si wafer) in a bell jar, saturated with chlorobenzene vapor. After 3 hours the film had only swollen  $\sim 5\%$  which is inconclusive since the bell jar still contained water vapor which could have also been responsible for the swelling. Thus

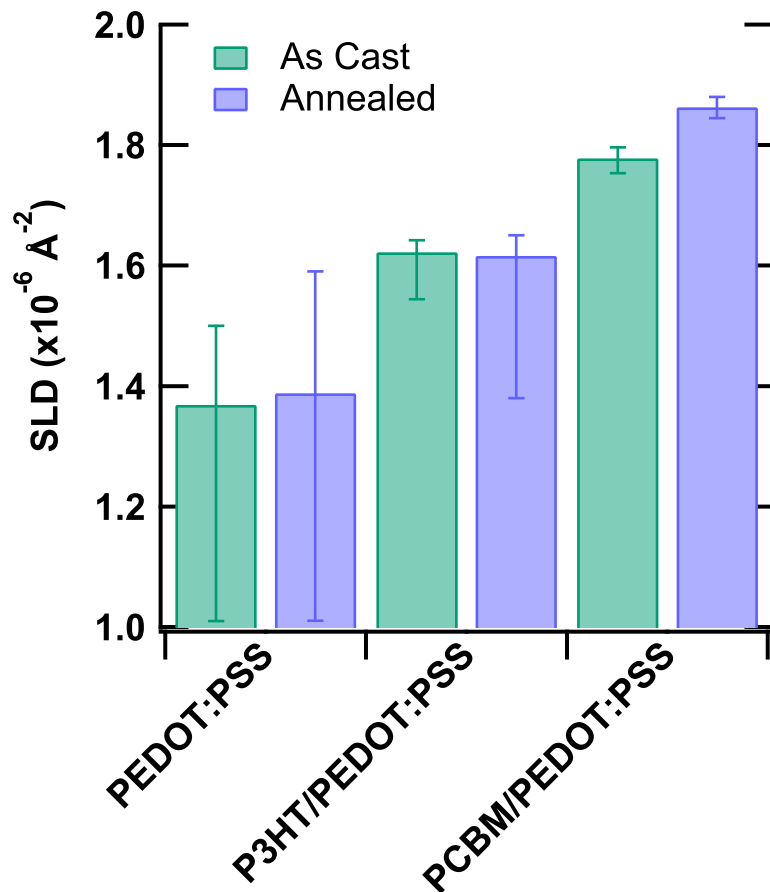


**Figure 5.5:** Chart showing SLD of the PSS-rich surface layer in pure and bilayer samples. Error bars represent 95% confidence interval calculated during the fitting procedure.

the mechanism by which PCBM diffuses into the PSS-rich layer at room temperature remains ambiguous.

#### 5.4 Conclusion

Neutron reflectivity has again proven essential in the study of polymer solar cell research by allowing a systematic study of diffusion into the electron blocking layer material, PEDOT:PSS, by P3HT and PCBM. In terms of the pure PEDOT:PSS, our findings suggest that a two slab model (or possibly a spline fit) should always

be attempted to show the presence, or absence, of a PSS-rich top surface. It was shown that P3HT is in fact immiscible in PEDOT:PSS at annealing temperatures up to 140 °C but the red-ox reaction mentioned in the literature still occurs, most likely at monolayer distances from the interface, undetectable in this study. It has been confirmed however that PCBM mixes with the PSS-rich layer that forms on top of PEDOT:PSS. PCBM is therefore likely miscible in PSS but not in PEDOT. This is an interesting finding since this, like the P3HT/PSS chemical reaction, may have implications related to conventional versus inverted solar device architectures.[16] The cause for PCBM diffusion at room temperature remains unclear and further study is required to understand this. Simple thermal diffusion studies as was performed here can offer profound insight into the processes occurring in polymer BHJs and multilayer stacks during fabrication.

## BIBLIOGRAPHY

- [1] Jonathan W. Kiel, Brian J. Kirby, Charles F. Majkrzak, Brian B. Maranville, and Michael E. Mackay. Nanoparticle concentration profile in polymer-based solar cells. *Soft Matter*, 6(3):641–646, 2010.
- [2] Andrew J Parnell, Alan D F Dunbar, Andrew J Pearson, Paul A Staniec, Andrew J C Dennison, Hiroshi Hamamatsu, Maximilian W A Skoda, David G Lidzey, and Richard A L Jones. Depletion of PCBM at the cathode interface in P3HT/PCBM thin films as quantified via neutron reflectivity measurements. *Adv. Mater.*, 22(22):2444–7, jun 2010.
- [3] J W Kiel, M E Mackay, B J Kirby, B B Maranville, and C F Majkrzak. Phase-sensitive neutron reflectometry measurements applied in the study of photovoltaic films. *J. Chem. Phys.*, 133(7):074902, aug 2010.
- [4] Lilian Chang, Hans W. a. Lademann, Jörg-Bernd Bonekamp, Klaus Meerholz, and Adam J. Moulé. Effect of Trace Solvent on the Morphology of P3HT:PCBM Bulk Heterojunction Solar Cells. *Adv. Funct. Mater.*, 21(10):1779–1787, may 2011.
- [5] B.J. Kirby, P.A. Kienzle, B.B. Maranville, N.F. Berk, J. Krycka, F. Heinrich, and C.F. Majkrzak. Phase-sensitive specular neutron reflectometry for imaging the nanometer scale composition depth profile of thin-film materials. *Curr. Opin. Colloid Interface Sci.*, 17(1):44–53, 2012.
- [6] J. A. Vrugt, C.J.F. ter Braak, C.G.H. Diks, B. A. Robinson, J. M. Hyman, and D. Higdon. Accelerating Markov Chain Monte Carlo Simulation by Differential Evolution with Self-Adaptive Randomized Subspace Sampling. *Int. J. Nonlinear Sci. Numer. Simul.*, 10(3):273–290, jan 2009.
- [7] BW Guralnick, BJ Kirby, C F Majkrzak, and M E Mackay. Morphological characterization of plastic solar cells using polarized neutron reflectivity. *Appl. Phys. Lett.*, 102:083305, 2013.

- [8] K Z Xing, M Fahlman, X W Chen, O Inganas, and W R Salaneck. The electronic structure of poly(3,4-ethylene-dioxythiophene): studied by XPS and UPS. *Synth. Met.*, 89:161–165, 1997.
- [9] G Greczynski, Th Kugler, and W.R Salaneck. Characterization of the PEDOT-PSS system by means of X-ray and ultraviolet photoelectron spectroscopy. *Thin Solid Films*, 354(1-2):129–135, oct 1999.
- [10] G Greczynski, Th Kugler, M Keil, W Osikowicz, M Fahlman, and W.R Salaneck. Photoelectron spectroscopy of thin films of PEDOT-PSS conjugated polymer blend: a mini-review and some new results. *J. Electron Spectros. Relat. Phenomena*, 121(1-3):1–17, dec 2001.
- [11] Jaehyung Hwang, Fabrice Amy, and Antoine Kahn. Spectroscopic study on sputtered PEDOT-PSS: Role of surface PSS layer. *Org. Electron.*, 7(5):387–396, oct 2006.
- [12] S. Timpanaro, M. Kemerink, F.J. Touwslager, M.M. De Kok, and S. Schrader. Morphology and conductivity of PEDOT/PSS films studied by scanning tunneling microscopy. *Chem. Phys. Lett.*, 394(4):339–343, 2004.
- [13] M. Kemerink, S. Timpanaro, M. M. de Kok, E. A. Meulenkaamp, and F. J. Touwslager. Three-Dimensional Inhomogeneities in PEDOT:PSS Films. *J. Phys. Chem. B*, 108(49):18820–18825, dec 2004.
- [14] Anthony M. Higgins, Simon J. Martin, Paul C. Jukes, Mark Geoghegan, Richard A. L. Jones, Sean Langridge, Robert Cubitt, Stephan Kirchmeyer, Anja Wehrum, and Ilaria Grizzi. Interfacial structure in semiconducting polymer devices. *J. Mater. Chem.*, 13(11):2814–2818, 2003.

- [15] P. C. Jukes, A. M. Higgins, M. Geoghegan, R. A. L. Jones, S. Langridge, A. Wehrum, and S. Kirchmeyer. Controlling the Surface Composition of Poly(3,4-ethylene dioxythiophene)–Poly(styrene sulfonate) Blends by Heat Treatment. *Adv. Mater.*, 16(910):807–811, may 2004.
- [16] Scott A. Mauger, Lilian Chang, Christopher W. Rochester, and Adam J. Moulé. Directional dependence of electron blocking in PEDOT:PSS. *Org. Electron.*, 13(11):2747–2756, nov 2012.
- [17] A. M. Nardes, M. Kemerink, R. A. J. Janssen, J. A. M. Bastiaansen, N. M. M. Kiggen, B. M. W. Langeveld, A. J. J. M. van Breemen, and M. M. de Kok. Microscopic Understanding of the Anisotropic Conductivity of PEDOT:PSS Thin Films. *Adv. Mater.*, 19(9):1196–1200, may 2007.
- [18] Annika Lenz, Hans Kariis, Anna Pohl, Petter Persson, and Lars Ojamäe. The electronic structure and reflectivity of PEDOT:PSS from density functional theory. *Chem. Phys.*, 384(1-3):44–51, jun 2011.
- [19] Thomas Stöcker, Anna Köhler, and Ralf Moos. Why does the electrical conductivity in PEDOT:PSS decrease with PSS content? A study combining thermoelectric measurements with impedance spectroscopy. *J. Polym. Sci. Part B Polym. Phys.*, 50(14):976–983, jul 2012.
- [20] Mario Petrosino and Alfredo Rubino. The effect of the PEDOT:PSS surface energy on the interface potential barrier. *Synth. Met.*, 161(23-24):2714–2717, jan 2012.
- [21] S. K. M. Jönsson, J Birgeron, X Crispin, G Greczynski, W Osikowicz, A. W. Denier van der Gon, W. R. Salaneck, and M Fahlman. The effects of solvents on the morphology and sheet resistance in poly(3,4-ethylenedioxythiophene)–polystyrenesulfonic acid (PEDOT-PSS) films. *Synth. Met.*, 139(1):1–10, aug 2003.

- [22] T.P. Nguyen and S.a. de Vos. An investigation into the effect of chemical and thermal treatments on the structural changes of poly(3,4-ethylenedioxythiophene)/polystyrenesulfonate and consequences on its use on indium tin oxide substrates. *Appl. Surf. Sci.*, 221(1-4):330–339, jan 2004.
- [23] Dean M DeLongchamp, Bryan D Vogt, Charles M Brooks, Kenji Kano, Jan Obrzut, Curt A Richter, Oleg A Kirillov, and Eric K Lin. Influence of a water rinse on the structure and properties of poly(3,4-ethylene dioxythiophene):poly(styrene sulfonate) films. *Langmuir*, 21(24):11480–3, nov 2005.
- [24] Ana B. Rodríguez, Monika M. Voigt, Simon J. Martin, Tracie J. Whittle, Robert M. Dalgliesh, Richard L. Thompson, David G. Lidzey, and Mark Geoghegan. Structure of films of poly(3,4-ethylene dioxythiophene)-poly(styrene sulfonate) crosslinked with glycerol. *J. Mater. Chem.*, 21(48):19324, nov 2011.
- [25] Jean-Pierre Veder, Roland De Marco, Graeme Clarke, San Ping Jiang, Kathryn Prince, Ernő Pretsch, and Eric Bakker. Water uptake in the hydrophilic poly(3,4-ethylenedioxythiophene):poly(styrene sulfonate) solid-contact of all-solid-state polymeric ion-selective electrodes. *Analyst*, 136(16):3252, 2011.
- [26] Jean-Pierre Veder, Kunal Patel, Manzar Sohail, San Ping Jiang, Michael James, and Roland De Marco. An Electrochemical Impedance Spectroscopy/Neutron Reflectometry Study of Water Uptake in the Poly(3,4-Ethylenedioxythiophene):Poly(Styrene Sulfonate)/Polymethyl Methacrylate-Polydecyl Methacrylate Copolymer Solid-Contact Ion-Selective Electrode. *Electroanalysis*, 24(1):140–145, jan 2012.
- [27] David M. Huang, Scott A. Mauger, Stephan Friedrich, Simon J. George, Daniela Dumitriu-LaGrange, Sook Yoon, and Adam J. Moulé. The Consequences of Interface Mixing on Organic Photovoltaic Device Characteristics. *Adv. Funct. Mater.*, 21(9):1657–1665, may 2011.

- [28] Jun Zhao, Ann Swinnen, Guy Van Assche, Jean Manca, Dirk Vanderzande, and Bruno Van Mele. Phase diagram of P3HT/PCBM blends and its implication for the stability of morphology. *J. Phys. Chem. B*, 113(6):1587–91, feb 2009.
- [29] James W. Kingsley, Pier Paolo Marchisio, Hunan Yi, Ahmed Iraqi, Christy J. Kinane, Sean Langridge, Richard L. Thompson, Ashley J. Cadby, Andrew J. Pearson, David G. Lidzey, Richard A. L. Jones, and Andrew J. Parnell. Molecular weight dependent vertical composition profiles of PCDTBT:PC71BM blends for organic photovoltaics. *Sci. Rep.*, 4:2295–2300, jun 2014.
- [30] Wenluan Zhang, Hao Shen, Brett W. Guralnick, Brian J. Kirby, Ngoc A. Nguyen, Roddel Remy, Charles F. Majkrzak, and Michael E. Mackay. Correlation between morphology and device performance of pBTTT:PC71BM solar cells. *Sol. Energy Mater. Sol. Cells*, 155:387–396, 2016.
- [31] Minze T. Rispens, Auke Meetsma, Roman Rittberger, Christoph J. Brabec, N. Serdar Sariciftci, and Jan C. Hummelen. Influence of the solvent on the crystal structure of PCBM and the efficiency of MDMO-PPV:PCBM ‘plastic’ solar cells. *Chem. Commun.*, (17):2116–2118, aug 2003.
- [32] NIST Neutron Activation Calculator.
- [33] Haiyun Lu, Bulent Akgun, and Thomas P. Russell. Morphological Characterization of a Low-Bandgap Crystalline Polymer:PCBM Bulk Heterojunction Solar Cells. *Adv. Energy Mater.*, 1(5):870–878, oct 2011.
- [34] Sen Yang, Kang Sun, and William M. Risen. Preparation and thermal characterization of the glass transition temperatures of sulfonated polystyrene-metal ionomers. *J. Polym. Sci. Part B Polym. Phys.*, 28(10):1685–1697, sep 1990.

## Chapter 6

### THESIS CONCLUSION AND FUTURE WORK

#### 6.1 Conclusion of Thesis

The discussion in this thesis was focused on developing differential scanning calorimetry (DSC) techniques for the characterization of the polymer component in polymer bulk heterojunction (BHJ) films for solar cell applications. The benchmark BHJ consisting of electron donating regioregular poly(3-hexylthiophene) (rrP3HT) and electron accepting phenyl-C<sub>61</sub>-butyric acid methyl ester (PCBM) was investigated. To perform quantitative thermal analysis on (rrP3HT) some fundamental thermodynamic properties must be found. Consequently, a series of oligomeric rrP3HT was investigated using DSC. By plotting their melting enthalpies versus their inverse molecular weight, a linear trend was found until the molecular weight reached  $\sim 10$  kg/mol where the chains crystallize in a chain-folded configuration. A correction factor obtained from grazing incidence small angle X-ray scattering was applied to the data to account for chain ends and poorly crystallized material. Extrapolation of the linear region to the y-axis (i.e. to infinite molecular weight) then yielded an enthalpy of fusion ( $\Delta H_m^\infty$ ) of 42.9 J/g which was used throughout this work to evaluate rrP3HT crystallinity. A similar linear extrapolation was done to find the equilibrium melting temperature ( $T_m^\infty = 285$  °C) and the entropy of fusion ( $\Delta S_m^\infty = 12.6$  J/mol·K).

After establishment of these reference points, quantitative analysis of rrP3HT proceeded by first measuring its crystalline and amorphous fractions in both bulk and thin film states. To do this, temperature modulated DSC (TMDSC) in *heat-only* mode was used to boost the sensitivity of the instrument so that the glass transition ( $T_g$ ) of rrP3HT can be accurately examined without jeopardizing the accuracy of the melting

enthalpy for crystallinity calculations. This method was used much throughout this work. Working with regiorandom (100% amorphous) P3HT the  $T_g$  (15 °C) and the step change in heat capacity at  $T_g$  ( $\Delta C_p = 0.32 \text{ J/g}^\circ\text{C}$ ) were evaluated. In contrast to the smooth singular transition of regiorandom P3HT, rrP3HT had a three step  $T_g$  corresponding to side chain dynamics in the crystal phase, a mobile amorphous fraction (MAF) and a rigid amorphous fraction (RAF). Calculations of MAF and RAF were therefore possible and rrP3HT was, for the first time, described in terms of a three phase morphology.

TMDSC was then applied to BHJ thin films prepared by spin coating from 1:1 ratio solution of rrP3HT and PCBM. The thin films exhibit rich thermal behavior with  $T_g$ s of the blend, crystallization exotherms and melting endotherms of the individual components all being visible. BHJ thin films in the as cast state were 100% amorphous, according to the polymer crystallinity analysis, which greatly improved to 30% after annealing at 140 °C for 20 minutes. Using the Couchman equation, it was discovered that rest of the BHJ material was not adequately accounted for in the  $T_g$  of the blend spurring the use of a more intricate analytical method to account for the entire mass of the BHJ film. A tag-team approach whereby data from both TMDSC and small angle neutron scattering (SANS) was used to quantify all phases of the BHJ. The analysis highlighted that the BHJ consists of four phases; crystalline rrP3HT, aggregated PCBM, RAF of rrP3HT and MAF of the blend containing MAF of rrP3HT with dissolved PCBM. This approach is a significant improvement of current BHJ models since it is quantitative and more intricate with attention paid to both polymer and fullerene phases.

The final chapter of the thesis was focused on the diffusion of the BHJ materials into the electron-blocking PEDOT:PSS layer. This layer is typically deposited before the BHJ and so understanding the mixing (or lack thereof) of the two layers is important. As a result neutron reflectivity of bilayers with PEDOT:PSS as the sub layer were examined. Also a pure PEDOT:PSS layer was tested and found to contain a PSS-rich surface. rrP3HT was found to chemically react (as was found in previous research) but

not mix with PEDOT:PSS. PCBM however diffused into PEDOT:PSS, having a large preference for the PSS-rich surface layer where  $\sim 12\%$  PCBM was found in that region after annealing. Interestingly, 8% was found in the PSS-rich layer without annealing suggesting that thermal post-treatment is not the sole reason for interlayer diffusion. More study should therefore focus on the mixing relationship between PCBM and PSS.

## **6.2 Future Work**

### **6.2.1 A New P3HT:PCBM Phase Diagram**

The research in this thesis has demonstrated the effectiveness of TMDSC for the characterization of polymer based BHJs. To further this study, it is imperative that a revised P3HT:PCBM phase diagram be constructed using TMDSC data on thin films. While the P3HT:PCBM phase diagram has already been published[1, 2], it was shown in Chapter 4 that thin film fabrication and post-processing shifts the eutectic point towards lower PCBM concentrations. Thus new information about the relationship of PCBM concentration to the important thermal transitions in the BHJ needs to be acquired since processing effects will directly influence the results. Also, the ability to now calculate the rigid amorphous fraction of P3HT from the methods described herein adds intricacy to the diagram that has been heretofore ignored. The outcome will be a more effective optimization tool and a better predictive model for the real BHJ thin film morphology.

### **6.2.2 Replacing PEDOT:PSS**

Chapter 4 began by the realization that annealing the BHJ film on PEDOT:PSS leaves a PSS residue on the film after removal. This is a major hindrance since an alternative annealing method had to be developed so the BHJ annealed film could be analyzed with accuracy. A solution to this would be to find a suitable replacement for PEDOT:PSS. For the purpose of these experiments, the replacement does not have to be electronically active, although alternative materials to that end do exist.[3, 4]

Finding another sacrificial material will allow for investigations into environmental effects on BHJ thin films[5] using the methods developed here.

The requirements for a PEDOT:PSS substitute are three-fold. First, it must not have any chemical reaction nor be miscible in any of the BHJ materials. This ensures that annealing can be performed in the typical manner (on a hotplate, for example) without any unwanted outcomes, like those of Chapter 5, that will throw off the mass balance in the BHJ or introduce impurities, like residual PSS chains. Second, it must not be soluble in the solvent used to deposit the BHJ layer. This prevents physical mixing of the layers during deposition. It follows that an orthogonal solvent would be used to deposit this new material; similar to PEDOT:PSS. Finally, the replacement material should be of similar surface energy to PEDOT:PSS (i.e. higher than that of both P3HT and PCBM) to avoid differences in the vertical segregation of the BHJ with annealing beyond what has been typically observed.[6, 7]

To this end, poly(N-vinyl pyrrolidone) (PVP,  $M_w \sim 360$  kg/mol) was briefly tested as a likely candidate. Being water soluble, PVP satisfies the solvent orthogonality requirement[8] and the literature shows that PVP also has an appropriately high

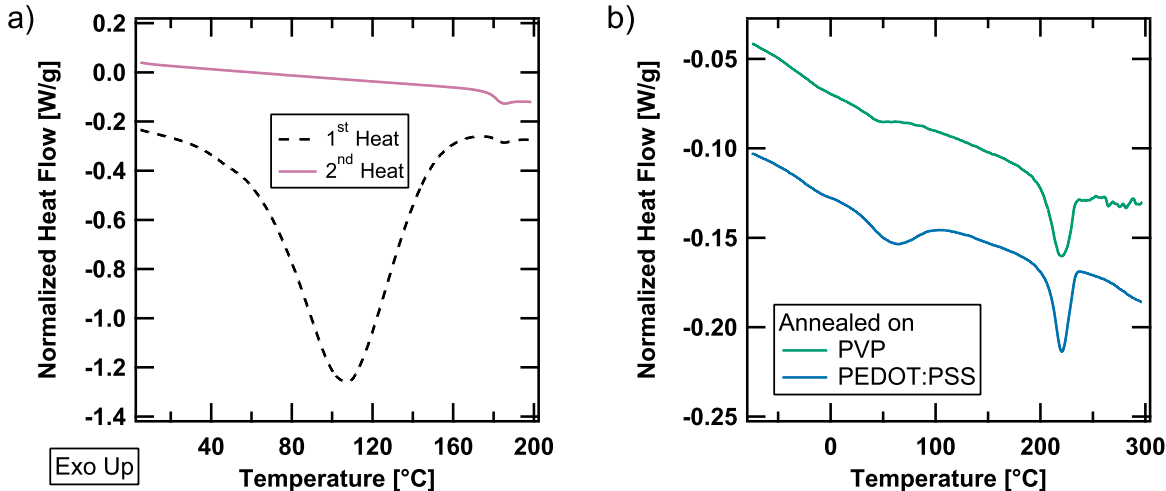


**Figure 6.1:** DSC of pure PVP (a) and TMSDC total heat flow of regioregular P3HT films that were annealed on two different sacrificial layers (b). Graphs were shifted vertically for clarity.

surface energy (53.6 mN/m for PVP[9] vs. 47.5 mN/m for PEDOT:PSS[10]). Its miscibility and chemical reactivity to P3HT and PCBM therefore warrants testing. Initial tests with regioregular P3HT is displayed in Figure 6.1.

It is immediately observed from Figure 6.1a that, like PEDOT:PSS, PVP is hygroscopic and the signal of water evaporation from the material in the first heat can be used as an indicator of the presence of PVP residue (see Chap. 4). The second heat shows a  $T_g$  of 180 °C, which agrees with the reported value for this molecular weight.[8] However, after annealing a pure, regioregular P3HT thin film on a PVP coated substrate, there is no evidence that PVP has reacted or mixed with P3HT. As a comparison, the same experiment was performed on a PEDOT:PSS coated substrate and the water loss peak is obvious (see Figure 6.1b). These promising results favor employing PVP as a more versatile sacrificial layer than PEDOT:PSS for the investigation of P3HT:PCBM BHJ thin films under a range of post-processing and degradation conditions. Further experiments would explore the interaction of PVP with PCBM and BHJ films respectively.

### 6.2.3 PCBM Thermal Properties

While PCBM is amorphous in the optimal morphology of P3HT:PCBM BHJs,[11, see Chap. 4] for other BHJ systems this may not be the case. Other electron donating polymers have different optimal BHJ compositions, many of which require PCBM concentrations as high as 80%.[12–14] It has been shown that the PCBM may contain nano-crystallites even though its diffraction pattern shows an apparent amorphous structure.[15] In addition, PCBM has the ability to crystallize well below its  $T_g$  of 130 °C[15, 16] making the existence of PCBM crystallites (or nano-crystallites) in other BHJ systems a real possibility. Being able to quantify the amount present therefore becomes an important aspect of BHJ characterization. Yet the enthalpy of fusion ( $\Delta H_m^\infty$ ) or any of the other fundamental properties of PCBM remain unknown. Unfortunately the techniques in this work (see Chap. 1) are not suitable for determining this. However, large, solvent free, single crystals of PCBM have been grown[17, 18]

and might be useful in finding these properties using a recently developed technique in our group.[19] Perhaps even the more traditional Hoffman-Weeks approach may be applicable in this case.[20]

#### 6.2.4 High Performance Donor Polymers

P3HT:PCBM is the most commonly investigated BHJ system, but it is not the most efficient. Advances in the chemical synthesis of semiconducting polymers has seen the improvement of polymer BHJ device efficiencies to over 10%.[21, 22] Essentially all of these high performance materials are alternating copolymers of electron-rich and electron-poor monomer units: so-called "push-pull" semiconducting polymers.[23, 24] These present unique challenges to calorimetry since little thermodynamic information exists for this class of polymers. As examples, PBTTT-C14 (a higher mobility relative of P3HT)[25] and PBDTTT-C (a member of the benzodithiophene family of copolymers)[26] were examined using DSC and are shown in Figure 6.2.

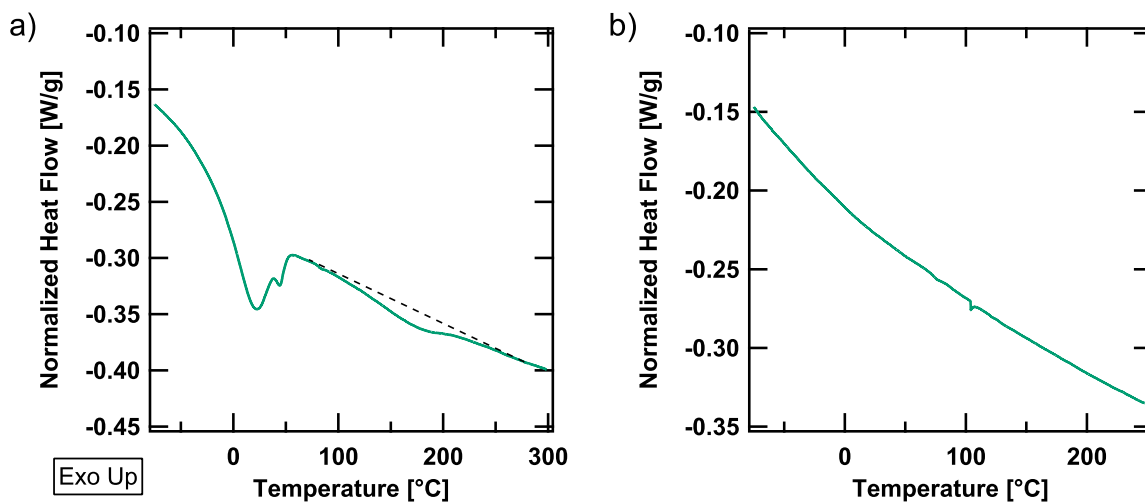


**Figure 6.2:** DSC of bulk PBTTT-C14 (a) and PBDTTT-C (b). Dashed line in (a) is drawn to define the broad backbone melting transition of PBTTT-C14.

For PBTTT-C14, two transitions can be identified that correspond to melting of the C14 side chains and polymer backbone respectively.[25, 27] Crystallinity analysis of this material will therefore need to address both components, either together or

separately. Moreover, studies have shown that this polymer forms a bimolecular crystal with PCBM which exhibits different melting behavior to the pure material.[14, 27, 28] In the extreme case of PBDTTT-C, no transitions can be identified in the thermogram which makes DSC analysis of the pure material – and potentially others of this class – impossible.

Complications inevitably arise when moving away from P3HT to other semiconducting polymers. Nevertheless, the calorimetric methods described in this thesis can still be used as a starting point for quantitative investigations of high performance semiconducting polymers and their blends with PCBM. Obtaining information about PCBM mixing and phase separation by  $T_g$  shifts, bimolecular crystallization, PCBM crystallization and melting phenomenon will be beneficial to the fundamental morphological understanding of this special class of polymers.

## BIBLIOGRAPHY

- [1] Jung Yong Kim and C. Daniel Frisbie. Correlation of Phase Behavior and Charge Transport in Conjugated Polymer/Fullerene Blends. *J. Phys. Chem. C*, 112(45):17726–17736, nov 2008.
- [2] Jun Zhao, Ann Swinnen, Guy Van Assche, Jean Manca, Dirk Vanderzande, and Bruno Van Mele. Phase diagram of P3HT/PCBM blends and its implication for the stability of morphology. *J. Phys. Chem. B*, 113(6):1587–91, feb 2009.
- [3] Mark T Greiner, Michael G Helander, Wing-Man Tang, Zhi-Bin Wang, Jacky Qiu, and Zheng-Hong Lu. Universal energy-level alignment of molecules on metal oxides. *Nat. Mater.*, 11(1):76–81, jan 2012.
- [4] Scott A. Mauger, Jun Li, Özge Tüzün Özmen, Andy Y. Yang, Stephan Friedrich, M. Diego Rail, Louise A. Berben, and Adam J. Moulé. High work-function hole transport layers by self-assembly using a fluorinated additive. *J. Mater. Chem. C*, 2(1):115–123, 2014.
- [5] Matthew O. Reese, Suren A. Gevorgyan, Mikkel Jørgensen, Eva Bundgaard, Sarah R. Kurtz, David S. Ginley, Dana C. Olson, Matthew T. Lloyd, Pasquale Morvillo, Eugene A. Katz, Andreas Elschner, Olivier Haillant, Travis R. Currier, Vishal Shrotriya, Martin Hermenau, Moritz Riede, Kiril R. Kirov, Gregor Trimmel, Thomas Rath, Olle Inganäs, Fengling Zhang, Mattias Andersson, Kristofer Tvingstedt, Monica Lira-Cantu, Darin Laird, Christine McGuinness, Srinivas (Jimmy) Gowrisanker, Michael Pannone, Min Xiao, Jens Hauch, Roland Steim, Dean M. DeLongchamp, Roland Rösch, Harald Hoppe, Nieves Espinosa, Antonio Urbina, Gülsah Yaman-Uzunoglu, Jörg-Bernd Bonekamp, Albert J.J.M. van Breemen, Claudio Girotto, Eszter Voroshazi, and Frederik C. Krebs. Consensus stability testing protocols for organic photovoltaic materials and devices. *Sol. Energy Mater. Sol. Cells*, 95(5):1253–1267, 2011.

- [6] David S. Germack, Calvin K. Chan, Behrang H. Hamadani, Lee J. Richter, Daniel A. Fischer, David J. Gundlach, and Dean M. DeLongchamp. Substrate-dependent interface composition and charge transport in films for organic photovoltaics. *Appl. Phys. Lett.*, 94(23):233303, 2009.
- [7] David S. Germack, Calvin K. Chan, R. Joseph Kline, Daniel A. Fischer, David J. Gundlach, Michael F. Toney, Lee J. Richter, and Dean M. DeLongchamp. Interfacial Segregation in Polymer/Fullerene Blend Films for Photovoltaic Devices. *Macromolecules*, 43(8):3828–3836, apr 2010.
- [8] James E. Mark. *Polymer Data Handbook*. Oxford University Press, 2nd edition, 2009.
- [9] Lovorka Zajic and Graham Buckton. The use of surface energy values to predict optimum binder selection for granulations. *Int. J. Pharm.*, 59(2):155–164, 1990.
- [10] Xiangjun Wang, Thomas Ederth, and Olle Inganäs. In Situ Wilhelmy Balance Surface Energy Determination of Poly(3-hexylthiophene) and Poly(3,4-ethylenedioxythiophene) during Electrochemical Doping-Dedoping. *Langmuir*, 22(22):9287–9294, oct 2006.
- [11] Neil D. Treat, Chris G. Shuttle, Michael F. Toney, Craig J. Hawker, and Michael L. Chabinyc. In situ measurement of power conversion efficiency and molecular ordering during thermal annealing in P3HT:PCBM bulk heterojunction solar cells. *J. Mater. Chem.*, 21(39):15224, sep 2011.
- [12] Sung Heum Park, Anshuman Roy, Serge Beaupre, Shinuk Cho, Nelson Coates, Ji Sun Moon, Daniel Moses, Mario Leclerc, Kwanghee Lee, and Alan J. Heeger. Bulk heterojunction solar cells with internal quantum efficiency approaching 100%. *Nat. Photonics*, 3(5):297–303, may 2009.

- [13] TY Chu, Jianping Lu, and S Beaupre. Bulk heterojunction solar cells using thieno pyrrole-4, 6-dione and dithieno silole copolymer with a power conversion efficiency of 7.3%. *J. Am. Chem. Soc.*, pages 4250–4253, 2011.
- [14] Wenluan Zhang, Hao Shen, Brett W. Guralnick, Brian J. Kirby, Ngoc A. Nguyen, Roddel Remy, Charles F. Majkrzak, and Michael E. Mackay. Correlation between morphology and device performance of pBTTT:PC71BM solar cells. *Sol. Energy Mater. Sol. Cells*, 155:387–396, 2016.
- [15] Xiaoni Yang, Jeroen K J van Duren, Minze T Rispens, Jan C Hummelen, R A J Janssen, Matthias A J Michels, and Joachim Loos. Crystalline organization of a methanofullerene as used for plastic solar-cell applications. *Adv. Mater.*, 16(9-10):802, may 2004.
- [16] Niko Van den Brande, Guy Van Assche, and Bruno Van Mele. Isothermal Crystallization of PC 61 BM in Thin Layers Far below the Glass Transition Temperature. *Cryst. Growth Des.*, page 151014090453004, oct 2015.
- [17] Mosè Casalegno, Stefano Zanardi, Francesco Frigerio, Riccardo Po, Chiara Carbonera, Gianluigi Marra, Tommaso Nicolini, Guido Raos, and Stefano Valdo Meille. Solvent-free phenyl-C61-butyric acid methyl ester (PCBM) from clathrates: insights for organic photovoltaics from crystal structures and molecular dynamics. *Chem. Commun.*, 49(40):4525, 2013.
- [18] Giulia Tregnago, Michael Wykes, Giuseppe M. Paternò, David Beljonne, and Franco Cacialli. Low-Temperature Photoluminescence Spectroscopy of Solvent-Free PCBM Single-Crystals. *J. Phys. Chem. C*, 119(21):150515121453001, may 2015.
- [19] Ngoc A. Nguyen. *Flow Induced/ Refined Solution Crystallization of a Semiconducting Polymer*. PhD thesis, University of Delaware, 2016.

- [20] John D. Hoffman and James J. Weeks. Melting process and the equilibrium melting temperature of polychlorotrifluoroethylene. *J. Res. Natl. Bur. Stand. Sect. A Phys. Chem.*, 66A(1):13–28, 1962.
- [21] Zhicai He, Chengmei Zhong, Shijian Su, Miao Xu, Hongbin Wu, and Yong Cao. Enhanced power-conversion efficiency in polymer solar cells using an inverted device structure. *Nat. Photonics*, 6(September):591–595, 2012.
- [22] Wenchao Zhao, Deping Qian, Shaoqing Zhang, Sunsun Li, Olle Inganäs, Feng Gao, and Jianhui Hou. Fullerene-Free Polymer Solar Cells with over 11% Efficiency and Excellent Thermal Stability. *Adv. Mater.*, apr 2016.
- [23] Junwu Chen and Yong Cao. Development of Novel Conjugated Donor Polymers for High-Efficiency Bulk-Heterojunction Photovoltaic Devices. *Acc. Chem. Res.*, 42(11):1709–1718, nov 2009.
- [24] Chunhui Duan, Fei Huang, and Yong Cao. Recent development of push-pull conjugated polymers for bulk-heterojunction photovoltaics: rational design and fine tailoring of molecular structures. *J. Mater. Chem.*, 22(21):10416, 2012.
- [25] Iain McCulloch, Martin Heeney, Clare Bailey, Kristijonas Genevicius, Iain Macdonald, Maxim Shkunov, David Sparrowe, Steve Tierney, Robert Wagner, Weimin Zhang, Michael L. Chabinyc, R. Joseph Kline, Michael D. McGehee, and Michael F. Toney. Liquid-crystalline semiconducting polymers with high charge-carrier mobility. *Nat. Mater.*, 5(4):328–333, apr 2006.
- [26] Jianhui Hou, Hsiang-Yu Chen, Shaoqing Zhang, Ruby I. Chen, Yang Yang, Yue Wu, and Gang Li. Synthesis of a Low Band Gap Polymer and Its Application in Highly Efficient Polymer Solar Cells. *J. Am. Chem. Soc.*, 131(43):15586–15587, nov 2009.
- [27] Fiona C. Jamieson, Ester Buchaca Domingo, Thomas McCarthy-Ward, Martin Heeney, Natalie Stingelin, and James R. Durrant. Fullerene crystallisation as

a key driver of charge separation in polymer/fullerene bulk heterojunction solar cells. *Chem. Sci.*, 3(2):485, jan 2012.

- [28] A. C. Mayer, Michael F. Toney, Shawn R. Scully, Jonathan Rivnay, Christoph J. Brabec, Marcus Scharber, Marcus Koppe, Martin Heeney, Iain McCulloch, and Michael D. McGehee. Bimolecular Crystals of Fullerenes in Conjugated Polymers and the Implications of Molecular Mixing for Solar Cells. *Adv. Funct. Mater.*, 19(8):1173–1179, apr 2009.

## Appendix A

### TMDSC OF PCBM

Bulk PCBM (Nano-C) was first melted for 2 minutes at 300 °C in the DSC before quenching to a starting temperature of -85 °C to obtain an amorphous sample. TMDSC was then performed under *heat-only* conditions at 3 °C/min with an oscillation period and amplitude of 30 seconds and  $\pm 0.239$  °C respectively. The result is shown in Figure A.1.

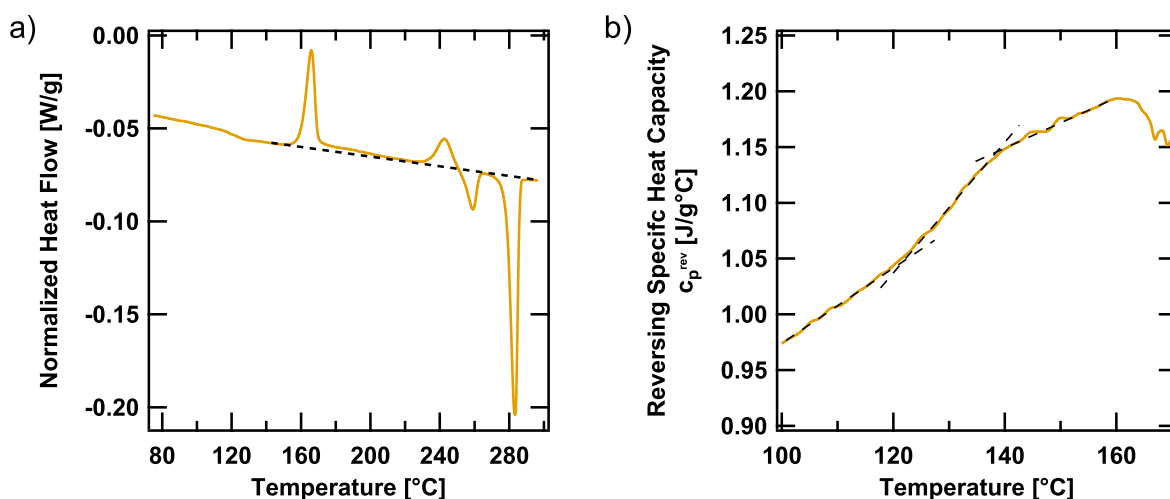


**Figure A.1:** TMDSC of pure PCBM. Shown are the total heat flow (a) and reversing specific heat capacity (b) in the  $T_g$  region.

Two crystallization and melting transitions are visible, preceded by a  $T_g$  which is clear in the reversing heat capacity in Figure A.1b. Measurements from Figure A.1b yielded a PCBM  $T_g$  of 130 °C and  $\Delta C_p$  of 0.11 J/g°C. While it has been speculated that thermally activated oligomerization may affect this measurement, both values reported here agree with the literature.[1, 2]

## BIBLIOGRAPHY

- [1] Deborah Leman, Mary Allison Kelly, Stuart Ness, Sebastian Engmann, Andrew Herzing, Chad Snyder, Hyun Wook Ro, R. Joseph Kline, Dean M. DeLongchamp, and Lee J. Richter. In situ characterization of polymer-fullerene bilayer stability. *Macromolecules*, 48(2):383–392, jan 2015.
  
- [2] Jun Zhao, Ann Swinnen, Guy Van Assche, Jean Manca, Dirk Vanderzande, and Bruno Van Mele. Phase diagram of P3HT/PCBM blends and its implication for the stability of morphology. *J. Phys. Chem. B*, 113(6):1587–91, feb 2009.

**Appendix B**  
**REPRINT PERMISSIONS**

This appendix includes reprint permissions for the previously published content in Chapters 1, 2 and 3 of this thesis.



# RightsLink®

[Home](#)[Account Info](#)[Help](#)

ACS Publications  
Most Trusted. Most Cited. Most Read.

**Title:** Conjugated Polymer Photovoltaic Cells  
**Author:** Kevin M. Coakley, Michael D. McGehee  
**Publication:** Chemistry of Materials  
**Publisher:** American Chemical Society  
**Date:** Nov 1, 2004  
Copyright © 2004, American Chemical Society

Logged in as:  
Roddel Remy  
Account #:  
3001077031

[LOGOUT](#)

## PERMISSION/LICENSE IS GRANTED FOR YOUR ORDER AT NO CHARGE

This type of permission/license, instead of the standard Terms & Conditions, is sent to you because no fee is being charged for your order. Please note the following:

- Permission is granted for your request in both print and electronic formats, and translations.
- If figures and/or tables were requested, they may be adapted or used in part.
- Please print this page for your records and send a copy of it to your publisher/graduate school.
- Appropriate credit for the requested material should be given as follows: "Reprinted (adapted) with permission from (COMPLETE REFERENCE CITATION). Copyright (YEAR) American Chemical Society." Insert appropriate information in place of the capitalized words.
- One-time permission is granted only for the use specified in your request. No additional uses are granted (such as derivative works or other editions). For any other uses, please submit a new request.

If credit is given to another source for the material you requested, permission must be obtained from that source.

[BACK](#)[CLOSE WINDOW](#)

Copyright © 2016 [Copyright Clearance Center, Inc.](#) All Rights Reserved. [Privacy statement](#). [Terms and Conditions](#).  
Comments? We would like to hear from you. E-mail us at [customercare@copyright.com](mailto:customercare@copyright.com)

**JOHN WILEY AND SONS LICENSE  
TERMS AND CONDITIONS**

Oct 25, 2016

---

This Agreement between Roddel Remy ("You") and John Wiley and Sons ("John Wiley and Sons") consists of your license details and the terms and conditions provided by John Wiley and Sons and Copyright Clearance Center.

License Number	3975940052915
License date	Oct 25, 2016
Licensed Content Publisher	John Wiley and Sons
Licensed Content Publication	Journal of Polymer Science Part B: Polymer Physics
Licensed Content Title	Enthalpy of fusion of poly(3-hexylthiophene) by differential scanning calorimetry
Licensed Content Author	Roddel Remy,Emily Daniels Weiss,Ngoc A. Nguyen,Sujun Wei,Luis M. Campos,Tomasz Kowalewski,Michael E. Mackay
Licensed Content Date	Sep 12, 2014
Licensed Content Pages	7
Type of use	Dissertation/Thesis
Requestor type	Author of this Wiley article
Format	Print and electronic
Portion	Full article
Will you be translating?	No
Title of your thesis / dissertation	Thermal Characterization of Bulk Heterojunction Polymer-based Solar Cells
Expected completion date	Dec 2016
Expected size (number of pages)	100
Requestor Location	Roddel Remy University of Delaware 201 Dupont Hall  NEWARK, DE 19716 United States Attn: Roddel Remy
Publisher Tax ID	EU826007151
Billing Type	Invoice
Billing Address	Roddel Remy University of Delaware 201 Dupont Hall  NEWARK, DE 19716 United States Attn: Roddel Remy
Total	0.00 USD
Terms and Conditions	

**TERMS AND CONDITIONS**

This copyrighted material is owned by or exclusively licensed to John Wiley & Sons, Inc. or one of its group companies (each a "Wiley Company") or handled on behalf of a society with which a Wiley Company has exclusive publishing rights in relation to a particular work (collectively "WILEY"). By clicking "accept" in connection with completing this licensing transaction, you agree that the following terms and conditions apply to this transaction (along with the billing and payment terms and conditions established by the Copyright Clearance Center Inc., ("CCC's Billing and Payment terms and conditions"), at the time that you opened your RightsLink account (these are available at any time at <http://myaccount.copyright.com>).

## Terms and Conditions

- The materials you have requested permission to reproduce or reuse (the "Wiley Materials") are protected by copyright.
- You are hereby granted a personal, non-exclusive, non-sub licensable (on a stand-alone basis), non-transferable, worldwide, limited license to reproduce the Wiley Materials for the purpose specified in the licensing process. This license, **and any CONTENT (PDF or image file) purchased as part of your order**, is for a one-time use only and limited to any maximum distribution number specified in the license. The first instance of republication or reuse granted by this license must be completed within two years of the date of the grant of this license (although copies prepared before the end date may be distributed thereafter). The Wiley Materials shall not be used in any other manner or for any other purpose, beyond what is granted in the license. Permission is granted subject to an appropriate acknowledgement given to the author, title of the material/book/journal and the publisher. You shall also duplicate the copyright notice that appears in the Wiley publication in your use of the Wiley Material. Permission is also granted on the understanding that nowhere in the text is a previously published source acknowledged for all or part of this Wiley Material. Any third party content is expressly excluded from this permission.
- With respect to the Wiley Materials, all rights are reserved. Except as expressly granted by the terms of the license, no part of the Wiley Materials may be copied, modified, adapted (except for minor reformatting required by the new Publication), translated, reproduced, transferred or distributed, in any form or by any means, and no derivative works may be made based on the Wiley Materials without the prior permission of the respective copyright owner. **For STM Signatory Publishers clearing permission under the terms of the [STM Permissions Guidelines](#) only, the terms of the license are extended to include subsequent editions and for editions in other languages, provided such editions are for the work as a whole in situ and does not involve the separate exploitation of the permitted figures or extracts,** You may not alter, remove or suppress in any manner any copyright, trademark or other notices displayed by the Wiley Materials. You may not license, rent, sell, loan, lease, pledge, offer as security, transfer or assign the Wiley Materials on a stand-alone basis, or any of the rights granted to you hereunder to any other person.
- The Wiley Materials and all of the intellectual property rights therein shall at all times remain the exclusive property of John Wiley & Sons Inc, the Wiley Companies, or their respective licensors, and your interest therein is only that of having possession of and the right to reproduce the Wiley Materials pursuant to Section 2 herein during the continuance of this Agreement. You agree that you own no right, title or interest in or to the Wiley Materials or any of the intellectual property rights therein. You shall have no rights hereunder other than the license as provided for above in Section 2. No right, license or interest to any trademark, trade name, service mark or other branding

("Marks") of WILEY or its licensors is granted hereunder, and you agree that you shall not assert any such right, license or interest with respect thereto

- NEITHER WILEY NOR ITS LICENSORS MAKES ANY WARRANTY OR REPRESENTATION OF ANY KIND TO YOU OR ANY THIRD PARTY, EXPRESS, IMPLIED OR STATUTORY, WITH RESPECT TO THE MATERIALS OR THE ACCURACY OF ANY INFORMATION CONTAINED IN THE MATERIALS, INCLUDING, WITHOUT LIMITATION, ANY IMPLIED WARRANTY OF MERCHANTABILITY, ACCURACY, SATISFACTORY QUALITY, FITNESS FOR A PARTICULAR PURPOSE, USABILITY, INTEGRATION OR NON-INFRINGEMENT AND ALL SUCH WARRANTIES ARE HEREBY EXCLUDED BY WILEY AND ITS LICENSORS AND WAIVED BY YOU.
- WILEY shall have the right to terminate this Agreement immediately upon breach of this Agreement by you.
- You shall indemnify, defend and hold harmless WILEY, its Licensors and their respective directors, officers, agents and employees, from and against any actual or threatened claims, demands, causes of action or proceedings arising from any breach of this Agreement by you.
- IN NO EVENT SHALL WILEY OR ITS LICENSORS BE LIABLE TO YOU OR ANY OTHER PARTY OR ANY OTHER PERSON OR ENTITY FOR ANY SPECIAL, CONSEQUENTIAL, INCIDENTAL, INDIRECT, EXEMPLARY OR PUNITIVE DAMAGES, HOWEVER CAUSED, ARISING OUT OF OR IN CONNECTION WITH THE DOWNLOADING, PROVISIONING, VIEWING OR USE OF THE MATERIALS REGARDLESS OF THE FORM OF ACTION, WHETHER FOR BREACH OF CONTRACT, BREACH OF WARRANTY, TORT, NEGLIGENCE, INFRINGEMENT OR OTHERWISE (INCLUDING, WITHOUT LIMITATION, DAMAGES BASED ON LOSS OF PROFITS, DATA, FILES, USE, BUSINESS OPPORTUNITY OR CLAIMS OF THIRD PARTIES), AND WHETHER OR NOT THE PARTY HAS BEEN ADVISED OF THE POSSIBILITY OF SUCH DAMAGES. THIS LIMITATION SHALL APPLY NOTWITHSTANDING ANY FAILURE OF ESSENTIAL PURPOSE OF ANY LIMITED REMEDY PROVIDED HEREIN.
- Should any provision of this Agreement be held by a court of competent jurisdiction to be illegal, invalid, or unenforceable, that provision shall be deemed amended to achieve as nearly as possible the same economic effect as the original provision, and the legality, validity and enforceability of the remaining provisions of this Agreement shall not be affected or impaired thereby.
- The failure of either party to enforce any term or condition of this Agreement shall not constitute a waiver of either party's right to enforce each and every term and condition of this Agreement. No breach under this agreement shall be deemed waived or excused by either party unless such waiver or consent is in writing signed by the party granting such waiver or consent. The waiver by or consent of a party to a breach of any provision of this Agreement shall not operate or be construed as a waiver of or consent to any other or subsequent breach by such other party.
- This Agreement may not be assigned (including by operation of law or otherwise) by you without WILEY's prior written consent.

- Any fee required for this permission shall be non-refundable after thirty (30) days from receipt by the CCC.
- These terms and conditions together with CCC's Billing and Payment terms and conditions (which are incorporated herein) form the entire agreement between you and WILEY concerning this licensing transaction and (in the absence of fraud) supersedes all prior agreements and representations of the parties, oral or written. This Agreement may not be amended except in writing signed by both parties. This Agreement shall be binding upon and inure to the benefit of the parties' successors, legal representatives, and authorized assigns.
- In the event of any conflict between your obligations established by these terms and conditions and those established by CCC's Billing and Payment terms and conditions, these terms and conditions shall prevail.
- WILEY expressly reserves all rights not specifically granted in the combination of (i) the license details provided by you and accepted in the course of this licensing transaction, (ii) these terms and conditions and (iii) CCC's Billing and Payment terms and conditions.
- This Agreement will be void if the Type of Use, Format, Circulation, or Requestor Type was misrepresented during the licensing process.
- This Agreement shall be governed by and construed in accordance with the laws of the State of New York, USA, without regards to such state's conflict of law rules. Any legal action, suit or proceeding arising out of or relating to these Terms and Conditions or the breach thereof shall be instituted in a court of competent jurisdiction in New York County in the State of New York in the United States of America and each party hereby consents and submits to the personal jurisdiction of such court, waives any objection to venue in such court and consents to service of process by registered or certified mail, return receipt requested, at the last known address of such party.

### **WILEY OPEN ACCESS TERMS AND CONDITIONS**

Wiley Publishes Open Access Articles in fully Open Access Journals and in Subscription journals offering Online Open. Although most of the fully Open Access journals publish open access articles under the terms of the Creative Commons Attribution (CC BY) License only, the subscription journals and a few of the Open Access Journals offer a choice of Creative Commons Licenses. The license type is clearly identified on the article.

#### **The Creative Commons Attribution License**

The [Creative Commons Attribution License \(CC-BY\)](#) allows users to copy, distribute and transmit an article, adapt the article and make commercial use of the article. The CC-BY license permits commercial and non-

#### **Creative Commons Attribution Non-Commercial License**

The [Creative Commons Attribution Non-Commercial \(CC-BY-NC\) License](#) permits use, distribution and reproduction in any medium, provided the original work is properly cited and is not used for commercial purposes.(see below)

#### **Creative Commons Attribution-Non-Commercial-NoDerivs License**

The [Creative Commons Attribution Non-Commercial-NoDerivs License](#) (CC-BY-NC-ND) permits use, distribution and reproduction in any medium, provided the original work is properly cited, is not used for commercial purposes and no modifications or adaptations are made. (see below)

#### **Use by commercial "for-profit" organizations**

Use of Wiley Open Access articles for commercial, promotional, or marketing purposes requires further explicit permission from Wiley and will be subject to a fee.

Further details can be found on Wiley Online Library

<http://olabout.wiley.com/WileyCDA/Section/id-410895.html>

**Other Terms and Conditions:**

**v1.10 Last updated September 2015**

**Questions? [customercare@copyright.com](mailto:customercare@copyright.com) or +1-855-239-3415 (toll free in the US) or +1-978-646-2777.**

---



# RightsLink®

[Home](#)[Account Info](#)[Help](#)

**Title:** Three-Phase Morphology of Semicrystalline Polymer Semiconductors: A Quantitative Analysis

**Author:** Roddel Remy, Sujun Wei, Luis M. Campos, et al

**Publication:** ACS Macro Letters

**Publisher:** American Chemical Society

**Date:** Sep 1, 2015

Copyright © 2015, American Chemical Society

Logged in as:

Roddel Remy

[LOGOUT](#)

## PERMISSION/LICENSE IS GRANTED FOR YOUR ORDER AT NO CHARGE

This type of permission/license, instead of the standard Terms & Conditions, is sent to you because no fee is being charged for your order. Please note the following:

- Permission is granted for your request in both print and electronic formats, and translations.
- If figures and/or tables were requested, they may be adapted or used in part.
- Please print this page for your records and send a copy of it to your publisher/graduate school.
- Appropriate credit for the requested material should be given as follows: "Reprinted (adapted) with permission from (COMPLETE REFERENCE CITATION). Copyright (YEAR) American Chemical Society." Insert appropriate information in place of the capitalized words.
- One-time permission is granted only for the use specified in your request. No additional uses are granted (such as derivative works or other editions). For any other uses, please submit a new request.

[BACK](#)

[CLOSE WINDOW](#)

Copyright © 2016 [Copyright Clearance Center, Inc.](#) All Rights Reserved. [Privacy statement.](#) [Terms and Conditions.](#) Comments? We would like to hear from you. E-mail us at [customer care@copyright.com](mailto:customer care@copyright.com)